The Pennsylvania State University

The Graduate School

IMPROVEMENTS ON POWER CALIBRATION AND CORE MONITORING AT THE PENN STATE BREAZEALE REACTOR

A Dissertation in

Nuclear Engineering

by

Gokhan Corak

Submitted in Partial Fulfillment

of the Requirements

for the Degree of

Doctor of Philosophy

August 2022

The dissertation of Gokhan Corak was reviewed and approved by the following:

William J. Walters
Associate Professor of Nuclear Engineering
Dissertation Co-Advisor
Co-Chair of Committee

Kenan Ünlü
Professor of Nuclear Engineering
Director of Radiation Science and Engineering Center
Dissertation Co-Advisor
Co-Chair of Committee

Marek Flaska
Professor of Nuclear Engineering

Douglas E. Wolfe
Professor of Materials Science and Engineering
Metals, Ceramics, and Coatings Processing Department Head for the Applied Research Laboratory

Jeffrey Geuther
Associate Research Professor
Associate Director for Operations RSEC

Arthur Motta
Graduate Program Chair of Nuclear Engineering
Professor of Nuclear Engineering

Abstract

Accurate measurements of the power level in a nuclear reactor are important for several reasons. First, the maximum allowable power is limited by regulations for safety reasons, and the reactor should always be maintained below that limit. Second, the power (and thus total neutrons produced by the reactor) is needed to accurately model experiments. Finally, the burnup (energy released per unit mass) of the fuel should be accurately quantified for fuel management purposes.

Different detector types measure the reactor power level in Penn State Breazeale Reactor (PSBR), which includes both neutron and gamma-ray measurements which includes fission chambers, gamma ion chamber, and compensated ion chamber and outputs of these detectors are calibrated using PSBR Checks and Calibration Procedures (CCP), specifically thermal power calibration (CCP-2). The power calibration is performed with the reactor operating at the D_2O tank, which should cause a flux tilt away from the detectors, and thus the lowest possible signal. This ensures that the displayed power is never underestimated than the power at other experimental locations. Energy deposition for the above-mentioned detectors is assumed linear during the calibration procedure but detector power levels may show different power outputs in some cases.

The first goal of this thesis is to investigate the behavior of the above-mentioned detectors in different temperatures and power levels while incorporating control rod movements, as well as the location of the reactor core near any experimental fixtures (e.g., at the Fast Neutron Irradiator and D_2O tank). The effect on the neutron flux shape due to the control rod position is investigated, along with how neutron flux shape affects the behavior of the detectors. Control rod movement significantly affects the neutron flux distribution inside the reactor core, especially in asymmetrical insertion and withdrawal of the control rods. Since these detectors are located at fixed positions outside of the reactor core, Self-Powered Neutron Detectors (SPND) and a miniature fission chamber are investigated computationally to estimate neutron flux in different positions around and within the reactor core due to their small size. The small size is an advantage, allowing them to be

placed closer to the reactor core. Later, an experiment conducted with a Westinghouse WL-7186 miniature fission chamber by placing it inside the central thimble at low power and asymmetrical control rod movement was investigated and results showed that asymmetric control rod movement has a significant effect on detectors depending on their location. MCNP 6.2 and Serpent 2 were used in the computational analysis of the behavior of the neutron and gamma transportation as well as the response of the above-mentioned detectors.

Detector responses were created for each detector and each core locality incorporating the MCNP FMESH method on various reactor power. The D_2O Tank 1000 kW was the case assumed base case for these calculations and a correction is applied for each detector. For non-D_2O core locations, the power is overestimated by up to 5.9 %. At lower power, the non-linearity in the detector response due to control rod movement results in up to 7.5 % error. Based on these results, a cubic fitting for the power was made for each core location to correct the observed power. Later, cubic curve fitting was applied to the detector responses to estimate true power in any reactor power for D_2O tank, R1 open pool, FNI, and FFT experimental locations. This will allow for more accurate modeling of experiments and better knowledge about fuel utilization.

Finally, detector responses were applied to the logbook laptop at PSBR to estimate corrected reactor powers for each case and fuel burnup. In current applications, fuel burnup is calculated by the reactor console. Logbook laptop burnup correction showed that for the core loading 59, a 3.7% difference in burnup was calculated using corrected power. In the future, the power correction method should be applied to the reactor console burnup calculation.

Table of Contents

List of Figures

List of Tables

List of Abbreviations

PSBR	Penn State Breazeale Reactor
RSEC	Radiation Science and Engineering Center
NRC	Nuclear Regulatory Commission
TRIGA	Training, Research, Isotopes, General Atomics
MW, kW, W	Megawatts, Kilowatts and Watt
FC	Fission Chamber
RSS FC	Reactor Safety System Fission Chamber
SFC	Spare Fission Chamber
CIC	Compensated Ion Chamber
GIC	Gamma Ion Chamber
SPND	Self-powered neutron detector
D_2O Tank	Heavy water moderator assembly
R1	Reactor operates at open pool
FNI	Fast neutron irradiator tube
FFT	Fast flux tube
DRF	Detector Response Function
MCNP	Monte Carlo N-Particle code
FM	Fission Matrix Method
SOP	Standard Operating Procedure
CCP	Checks and Calibration Procedure
ARO	All control rods out position
ARI	All control rods inserted position
ADVANTG	AutomateD VAriaNce reduction Generator
CADIS	Consistent Adjoint Driven Importance Sampling
FOM	Figure of Merit
SDEF	Source definition
SSW-SSR	Surface Source Write and Read

Acknowledgements

I am grateful to many people for supporting me to pursue this degree. First, I would like to thank my Co-Advisors Dr. William Walters and Dr. Kenan Ünlü for their continuous support, for their patience, and motivation. Without them, this work would not exist.

I would also like to thank my committee, Dr. Marek Flaska, Dr. Douglas Wolfe, and Dr. Jeffrey Geuther for engaging with me and improving this work in this process with their comments and recommendations.

I am grateful for the financial support provided by the Radiation Science and Engineering Center and the Department of Energy, Nuclear Energy University Programs that jointly awarded grant with Westinghouse Corporation during my education, (NEUP Project 16-10773). Any opinions, findings, conclusions, or recommendations expressed in this publication are those of the author and do not necessarily reflect the views of the funding agency.

I would like thank to Radiation Science and Engineering center staff for their support for the experimental design and reactor operation for the measurements.

To my friends in nuclear engineering, especially, Alibek, Maksat, Susanna, Can, Onur, Yucel, Bugra, and Nuri thank you for the discussions, and your support throughout the process of my research and writing this thesis. I am fortunate to have friends like you.

I owe thanks to my family for helping me starting from Day 1 on the earth, and for their unending love and support. I wish to thank my wife, Özlem, who provide endless love and support in my life and my career. Finally, I would like to thank my little son, Aras Ege, who brings joy to our little family, and I hope one day you become a nuclear engineer.

Chapter 1

Introduction

A vital parameter in reactor control is the accurate measurement of the reactor power at any moment and obtaining accurate power measurement information is important for several reasons. The first and most important is that accurate measurements are necessary to operate the nuclear reactor safely. Secondly, accurate reactor power measurements lead to better research outcomes from experiments that use the reactor. Accurate reactor power measurements also lead to the effective use of the reactor. Power measurement uncertainties play a key role in determining the maximum allowable power limit for the power reactors. The Nuclear Regulatory Commission (NRC) licenses a reactor by limiting the maximum heat output, or power level for the reactor core [1]. Precise measurements reduce the uncertainties in the reactor power levels. which leads to the safe operation of the reactor at higher power levels. Power uprates play a vital role in power reactors. From 1977 to 2018, power reactors were attributed to 23764 MWt, 7921 MWe total in the United States [2]. Research reactors do not have a need to produce electricity, so power uprates are not the main concern for them. However, less uncertainty in power level measurements is desired since less uncertainty gives a better understanding of power levels and safe reactor operation. Improved power measurements can also lead to less uncertainty in burnup calculations, improving the tracking of fission products and transuranic isotope production.

Nuclear reactor power measurements are taken with neutron and gamma detectors, and the most common type are ionization chambers. The reactor power is proportional to the amounts of released gamma rays and neutrons from the reactor core due to fission. These detectors measure local flux near the outside of the reactor core, which means that the total number of neutrons in the reactor core cannot be measured directly, but the total number of neutrons due to fission can be estimated using calibration techniques and simulations. The PSBR has three different types of detectors in the pool: two Fission Chambers (FC), two Gamma Ion Chambers (GIC), and one Compensated Ion Chamber (CIC). Power monitoring in the PSBR is done by these ex-core neutronic and gamma instruments which are similar to other research reactors. The calibration of the detectors is carried out by the thermal power calibration procedure which is done at 800 kW. After calibration of the detectors, the power output from each detector is assumed to be a linear function of the detector response which is related to the incident particle that causes an event inside the detector region. This assumption is an excellent assumption if the power distribution does not change between the reactor power levels and operating conditions. However, many routine reactor operations change the shape of the power distribution, which could affect the detector response even for the same total power output. These operations may include:

- Asymmetric insertion of control rods shifts power towards or away from the detectors
- Symmetric insertion of control rods shifts power towards the outer edge of the reactor (this is especially true of the PSBR which is a larger core than most TRIGA reactors), as well as axially towards the bottom section of the reactor core
- Operation of the reactor next to the D_2O tank shifts power towards the tank and away from the detectors

The asymmetric control rod movement causes power shift in TRIGA reactors which has been noted by other researchers such as those at the Josef Stefan Institute (JSI), who performed an investigation into optimal detector positioning to reduce this effect, the use of multiple detectors, and the calculation of a correction factor for the power based on rod position [3]. The PSBR mostly uses symmetric control rods during standard operation, and the level of insertion depends on the desired power level. Previously, the reactor operated with asymmetric insertion more often. A symmetric insertion shifts power toward the outer edge of the reactor, towards the detectors. This is especially true in the PSBR, which has more fuel elements than most TRIGAs (the current core has more than 100 fuel elements, compared to <60 at JSI in the core). Operation at the D_2O tank results in a lower detector response at a given power level, so the current power calibration procedure is performed at the D_2O tank. This results in conservative (lower than reality) power level readings under other operating conditions for safety reasons but will also lead to over-prediction of fuel burnup.

All of these factors together make it very challenging to predict the true power level of the reactor given a single detector response since any method would need to take into account all of the control rod positions, the location in the pool, and potentially other factors such as fuel temperature. To achieve this, this thesis proposes to couple calculated detector response functions (DRFs), which are calculated by the Monte Carlo N-particle transport code (MCNP) individual fuel element response method, with the FMESH method developed using MCNP as well as a recently developed fission-matrix-based methodology that has been developed for the analysis of the PSBR with temperature and control rod feedback [4]. Similar coupling methods have proved successful in analyses of other systems [4],[5].

To achieve accurate power measurements; an MCNP model will be made for all detector types currently available at PSBR and self-powered neutron detectors. The effect of fuel temperature, control rod positions, and the reactor core locality on detector responses will be also be discussed. Experiment results will be coupled with the Fission Matrix Method and FMESH method to estimate detector responses. Finally, a correction method will be presented that incorporates all the above-mentioned parameters to accurately estimate true reactor power in any condition.

The main focus of this thesis is to get a better understanding of the true reactor power measurements. Knowing the true reactor power will improve reactor experiments and fuel management calculations.

1.1 Motivation

The PSBR has different types of detectors that are in use for power measurement. As mentioned before, the reactor power is estimated to be directly proportional to the response of these detectors. The power distribution will change which will cause changes in the source distribution. Besides, the probability of the neutrons reaching the detector from the source location will change; all of these parameters affect the accurate measurement of the power.

It is desirable to know the power measurements more accurately for fuel management and experimental reasons. MCNP would give a better understanding of the neutron flux and statistical fluctuation depending on the position of the detectors, control rod movements, and fuel temperature. Experiments and simulations can be compared to see how reactor power is changing with the above-mentioned parameters. Accurate measurements may be done for a variety of power levels by incorporating in-core detections such as self-powered neutron detectors and miniature fission chamber detectors where they can be placed in any position in or out-core due to their small size. All of these factors may improve power measurements at the PSBR.

1.2 Objectives

The goal of this thesis is to investigate the behavior of the ex-core detectors due to a variety of reactor operating conditions, with the aim of better estimating the true reactor power. The main objectives are:

- Develop an MCNP model for ex-core detectors, self-powered neutron detectors, and a WL-7186 miniature fission chamber.
- Investigate the neutron flux shape change with the control rod positions, and how this affects the behavior of the detectors.

- Investigate the effect of reactor operation parameters on the detector response including fuel temperature, control rod positions, and core locality (near D_2O, FNI, FFT, and open pool).
- Investigate asymmetric control rod position effect on neutron flux and the detector behaviors.
- Investigate the importance of individual fuel rods on the detector response.
- Perform an experiment with an in-core detector and ex-core detectors to validate the computational model.
- Develop a method to quickly estimate detector response under varying conditions by coupling FMESH and Fission Matrix Method calculations with detector response functions.
- Develop a correction for the power calibration based on operating conditions and a metric for power tilt based on operation detectors to improve power measurements and fuel burnup.

The rest of the thesis is divided as follows. Chapter 2 gives a brief description of the Penn State Breazeale Reactor. Then, this chapter gives a background about the PSBR power detection system that includes the detector types. After that, a brief explanation is given about how the thermal power calibration is made, and why the calibration is important to the reactor power measurements, and how much power difference there is between the actual versus the observed power. Finally, a literature review was done to show the importance of this thesis in this field.

The current detector types in the reactor core and their working principles are explained in Chapter 3. This chapter also contains the Monte Carlo modeling and MCNP code, MCNP modeling of the reactor core, detector design, and ADVANTG automated weight window generator for PSBR. Finally, a description of the visualizing tools and scripts that were developed for this thesis will be explained to understand and visualize complex data outputs.

Chapter 4 explains the different modes that are available in MCNP. This chapter focuses on presenting preliminary results for several methods using MCNP and Serpent 2. A comparison of these methods is included in this chapter and these methods will be used throughout the thesis. Individual fuel element detector response is also explained in this chapter since is used by the FMESH and Fission Matrix Method.

The effect of operational parameters on the detector response function for a given power level is examined in Chapter 5. These operational parameters are symmetric/asymmetric control rod movement and the presence of the reactor core to the experiment fixtures such as the D_2O tank, FNI, and FFT. The temperature effect for the fuel elements is also investigated in this chapter.

Chapter 6 introduces the experiment done at PSBR using ex-core detectors and an additional miniature fission chamber, which was placed into the central thimble of the reactor. This chapter describes the preparation done for the experiment, calculations that are necessary for the Standard Operating Procedure at PSBR (SOP-5) calculations, and results of the high power ex-core detector results, low power ex-core detector, and WL-7186 miniature fission chamber results for asymmetrical insertion and withdrawal. In addition, a comparison is done with experimental and simulation results to show the differences between them.

The calculation of detector responses for each ex-core detector are discussed in Chapter 7. Results are presented for the calculation of detector response using the MCNP/DRF that uses both FMESH fission source calculations and individual fuel element responses on the detectors. This chapter also shows how the correction is done for power measurement using the aid of simulations and experiments done at the reactor.

Chapter 8 describes how the results of this thesis could be used in reactor operation, reactor power measurement, and fuel burnup estimation. The developed detector responses can be used to estimate true reactor power for different cases. To do that, logbook computer data created in Excel will be multiplied with power corrections depending on the type of the operation. By using this method, better fuel utilization and burnup calculations can be made. In the future, detector responses can be implemented directly into the control console to estimate fuel burnup and corrected power.

Finally, Chapter 9 summarizes the work done in this thesis and gives a conclusion and some insight into future work.

Chapter 2
The Penn State Breazeale Reactor (PSBR)

The Penn State Breazeale Reactor (PSBR) is the oldest American university reactor that is still operating, and the reactor reached criticality on August 15, 1955. The PSBR was initially designed as a Materials Testing Reactor (MTR) which used plate-type fuel and was licensed for a power level of 100 kWth. The PSBR was later upgraded to 200 kWth in 1960. In 1965, Penn State received a license that allowed for the conversion of the reactor from highly enriched MTR fuel to a TRIGA (Training, Research, Isotopes, General Atomics) design. This design requires low-enriched uranium fuel and provides steady-state power of 1 MW, with the capability to pulse the reactor up to 2000 MW [6]. The PSBR's movable core does not contain a fixed reflector and is located in a 24 ft.-deep pool with ~71,000 gallons of demineralized water. Figure 2-1 shows a picture of The Penn State TRIGA Reactor core. A variety of dry tubes and fixtures are available in or near the core for irradiating samples. A pneumatic transfer system is also available for the irradiation of samples.

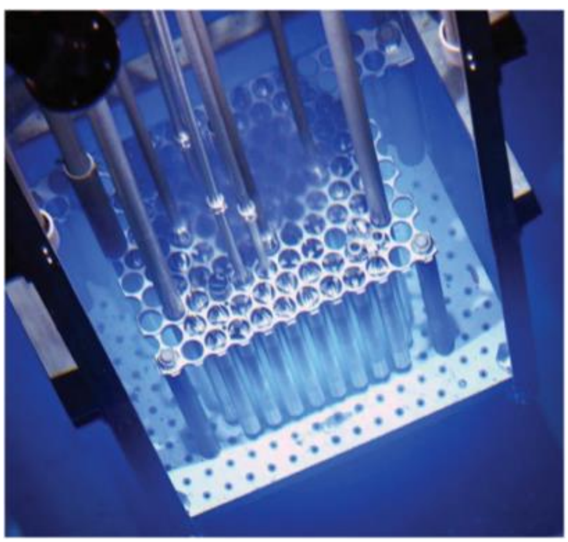

Figure 2-1: A picture of Penn State TRIGA Reactor Core

The PSBR has four standard control rods, three of which, the shim, safety, and regulating control rods, can be placed in automatic control. The fourth control rod, the transient control rod, is always in manual mode and is used to pulse the reactor. An Experimental Control Rod and Drive (ECRD) may be positioned over the core and used for control experiments. The standard control rods have a removal distance of 15-inches which is the same length as the standard TRIGA fuel. The safety, shim, and regulating rods have two different regions. They have a 15-inch boron carbide neutron absorber section which is located below 15 inches of TRIGA fuel. Withdrawal of the control rods from the core will insert the fuel follower region of the control rods into the core, which increases the positive reactivity. [7].

2.1 PSBR Power Detection System

Considering redundancy is vital from a reactor safety perspective. To take into account redundancy, The Penn State Breazeale Reactor (PSBR) has three different types of detectors, five of which are in the reactor pool. There are two Fission Chambers (FC), one connected to the Reactor Safety System (RSS), and one spare. The RSS Fission Chamber is connected to the Wide Range Channel. Likewise, there are two Gamma Ion Chamber (GIC), one of which is connected to the Power Range Channel and the other one is spare. This gives a redundant high-power SCRAM signal to the RSS. Finally, the Compensated Ion Chamber (CIC) is in use as a spare detector. These channels are the main indicator of the reactor power and are responsible for the reactor safety, such as high power SCRAM and high-temperature SCRAM. The power range reactor trip comes from the GIC and the wide range drawer reactor trip comes from the main fission chamber. Wide range and Power range monitors can be seen in Figure 2-2 PSBR control console.

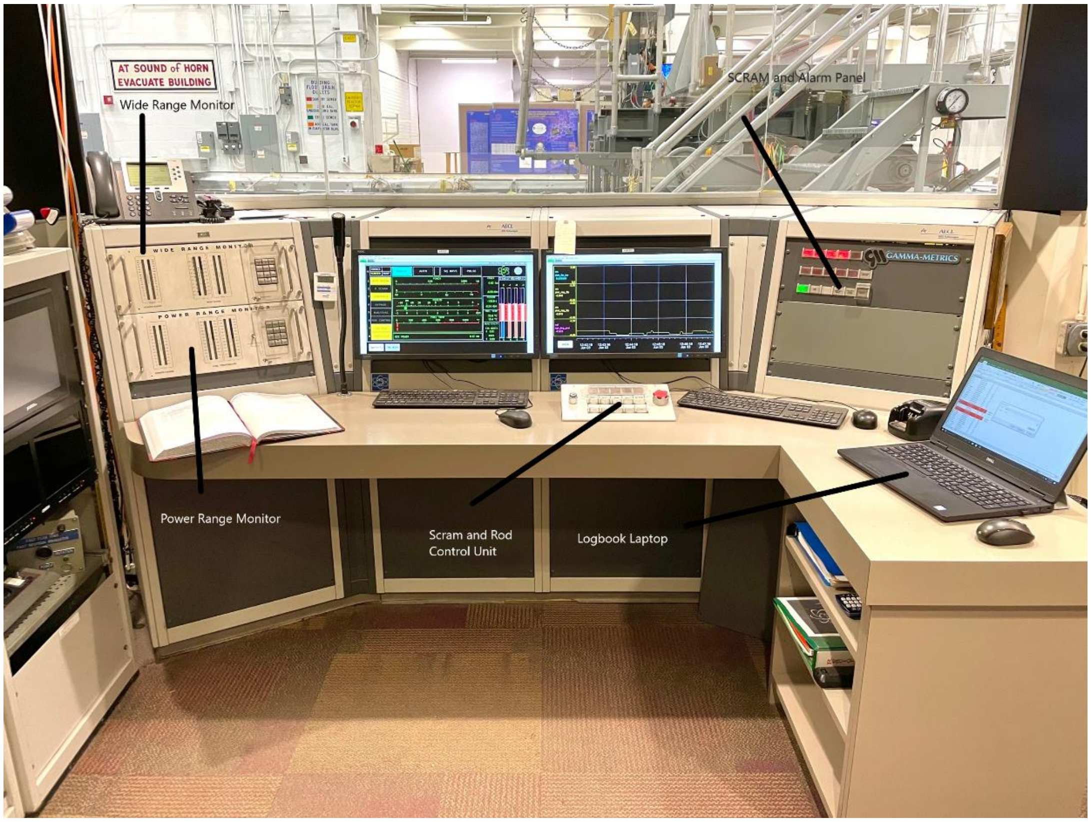

Figure 2-2. PSBR control console and equipment [8]

Power monitoring in the PSBR is done by these neutronic and gamma-ray instruments which is similar to most other research reactors. The calibration of these detectors is carried out by the thermal procedures. The PSBR has a power calibration procedure that relies on thermal calculations. The detectors are biennially calibrated according to the Checks and Calibrations Procedure (CCP) not to exceed thirty months. Additionally, the thermal power calibration has to be re-done after the change in the new reactor core loads.

The Penn State Breazeale Reactor Control and monitoring system`s main indicator of power is the Wide Range Fission Chamber. The GIC provides a second power range input to the reactor safety system. The Spare fission chamber, GIC, and CIC are also installed as backup indicators for reactor power and will be discussed throughout this chapter. Detector positions relative to the reactor core are shown in Figure 2-3.

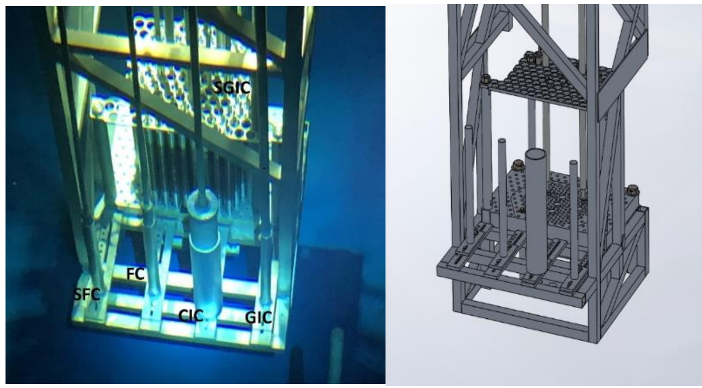

Figure 2-3: Penn State Breazeale Reactor in-pool detectors: fission chambers, compensated ion chamber, and gamma ion chambers

Figure 2-4 shows the drawing of the detectors' locations at PSBR core assembly and location in the reactor pool. Since the detectors are positioned outside of the core, a change in the reactivity introduced by the control rods will affect indicated power.

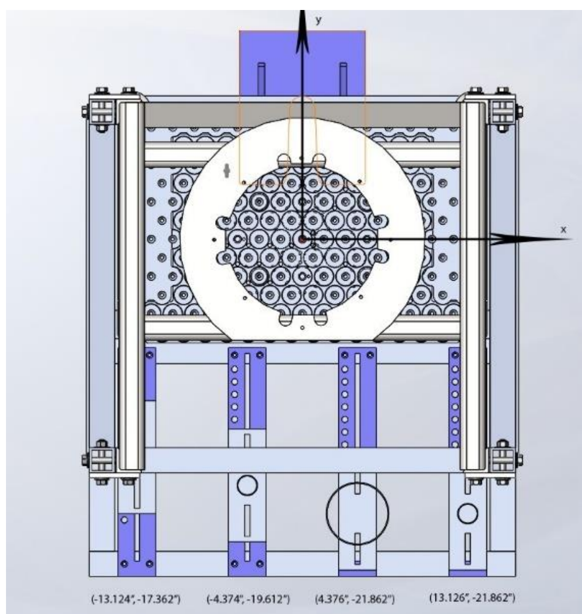

Figure 2-4: Detector position relative to the center of the reactor core

The PSBR has special instrumental fuel elements, one of which is placed in the highest neutron flux location. These instrumental fuel elements contain thermocouples to measure fuel temperature. Thermocouples are implanted within the fuel and provide a temperature input to the RSS. Figure 2-5 represents the TRIGA fuel and the instrumental fuel element [9].

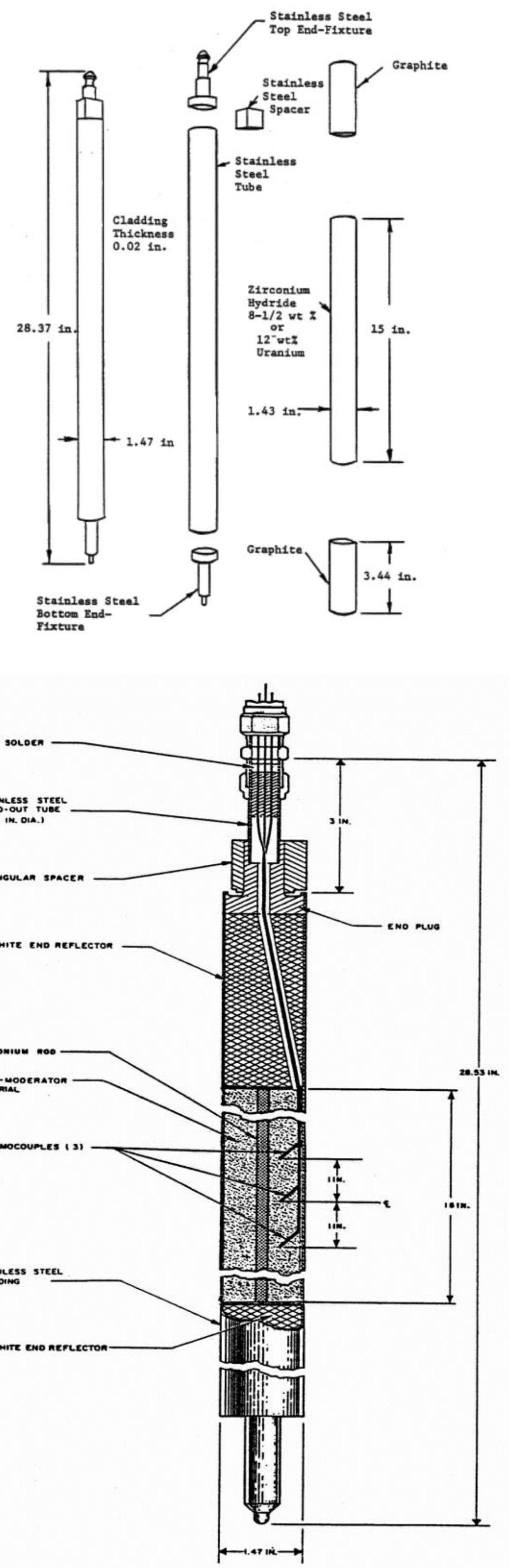

Figure 2-5: Penn State Breazeale Reactor fuel elements and the instrumental fuel element [10]

The radiation detectors that are in use at the PSBR have different working principles from each other due to the different behavior of the incident radiation.

An incident thermal neutron will cause the uranium-235 atom to fission, with the average of two fission fragments produced having high kinetic energy. These fission fragments will cause ionization of the argon gas within the fission chamber. The fission fragments resulting from the interaction of neutrons with the coating cause a significantly larger amount of ionization within the fission chamber than the gamma radiation incident on the detector. This results in the neutron-generated charge pulses being significantly larger than the gamma ray pulses [11]. Due to this reason, fission chambers are very sensitive to neutron flux and this allows the fission chambers to operate in higher gamma fields. Fission Chambers can work in three operation modes: pulse, current, and the Campbelling mode which is also known as Mean Square Voltage (MSV) mode. The usages of these modes depend on the neutron flux level at the detector, and the suitable operation mode can be chosen for the Fission Chamber to give an accurate power level indication. In pulse mode, the voltage produced by the RC circuit is measured. Pulse mode is used in a research reactor mainly during the start-up. The main reason that pulse mode is used in a startup is that it can provide spectral information that is used to distinguish between neutrons and gamma radiation. The current mode is the most common operation mode in detection systems. A current measuring circuit is placed across the terminals of the detector and the average current is measured by the system. Finally, MSV or Campbelling mode is mainly used in a nuclear reactor to measure neutrons in a high gamma background. The MSV circuit blocks the steady-state component of the current and squares the amplitude of the varying component. The resulting signal is proportional to the square of the charge created by each incident particle of radiation, which gives a difference between types of radiation. PSBR FC operates in pulse mode under 300W and MSV mode for high power applications.

The gamma ion chamber is connected to the Power Range monitor and operates in current mode only. The GIC generates a current output that is proportional to the reactor power. The compensated ion chamber has an electrically compensated ionization chamber to measure thermal neutron flux. The primary use of this detector is in a mixed neutron and gamma ray radiation field where the gamma flux is the dominant portion of the total radiation.

According to Heidrich [12], the amount of neutrons that reach the detector depend on the neutron flux and reactor pool temperature. When the pool temperature increases, the absorption cross-section decreases, and more neutrons reach the detectors; this results in an indicated power that is higher than the actual power for the fission chambers and the compensated ion chamber. On the other hand, gamma ion chambers are affected only by the changes in the density of the water as it relates to the shielding of gamma-rays, which is minuscule since density changes are very small in the PSBR.

All of the above-mentioned detectors have been designed in MCNP with a simplified version since structural parts do not contribute much to the tally results. These simplified detector models will be described in Chapter 3.

2.2 Thermal Power Calibration Method for TRIGA Reactors

The PSBR is required to measure its thermal power output biennially while not exceeding 30 months. Reactor power measurements play an important role in safety and power needs to be accurately determined. The reactors licensed by the Nuclear Regulatory Commission (NRC) must operate at a power level that is less than their licensed power.

The thermal power level in a power reactor is usually determined by the heat balance method with the secondary steam plant. Since the research reactors do not contain steam processing parts, they need to come up with a different method to determine the thermal power level at the reactor.

The PSBR reactor thermal power calibration is carried out by the heat exchanger balance method. In this method, the steady-state energy balance of the primary cooling loop is required. The inlet temperature, outlet temperature, and the water flow in the primary cooling loop are measured. Thermal power can be calculated using these parameters and the estimated heat losses from the pool. Estimation of the pool heat loss is challenging and may cause uncertainties in the reactor thermal power calibration procedure. According to Heidrich [12], the relative uncertainty of the external effects in the thermal power calibration is approximately 2.6% for a 400 kW, 1.3% for an 800 kW, and reduce to 1.0% for full power (1 MW) power calibration. This signifies that the current method seems precise but still has 10.4 kW uncertainty at 800 kW. This method also includes conduction through the pool walls, evaporation from the pool water's surface, and conduction through the aluminum gate that separates the north and south sides of the reactor pool, which is not a true loss term [12].

The calibration of the ex-core detectors is done at 800 kW after the thermal calibration is finalized. These means detector power responses will carry on the uncertainties due to the thermal power calibration uncertainties. In addition, detector powers are assumed linear with a change of power. Since the detectors are located at the south end of the reactor core, any change in neutron flux distribution on the other side of the core will not be taken into account which will cause significant changes in power measurements. This neutron flux distribution can be changed by many effects such as control rod insertion, core location change, etc. Even if the reactor core is assumed symmetrical, the reactor core is not purely symmetric due to the control rod types, location of the fuels, and having dry tubes/water channels inside the reactor core.

The uncertainty on the reactor power level and the method that utilizes the thermal calibration method may be improved using MCNP. With the aid of the experiment and simulations, reactor power change around the core will be investigated. This may improve the accuracy of the thermal power calibration and the detector calibration.

2.3 How different are detector outputs and actual power?

As mentioned in the previous section, the thermal power calibration method has 1.3% uncertainty for an 800 kW thermal power calibration. This uncertainty will affect the detector calibration, thus the accurate power measurement. In addition to that, the reactor core can be moved around the pool near the different fixtures. The neutron flux distribution will vary between these locations and operational conditions such as control rod insertion and removal. With the D_2O tank coupled to the reactor core, the neutron flux profile shifts to the detector region. Due to this reason, the calibration procedure is done near the D_2O tank to ensure the power reading is at the maximum. According to Bascom [10], with the instrumentation calibrated at the previous D_2O tank, the actual thermal power in the open pool (R1) position was 960 kW when the reactor console measured 1 MW by the CCP-2 Thermal Power Calibration. This discrepancy between the different locations should be investigated. The thermal power calibration method only focuses on a single power level at a single location. It does not take into account other effects such as core location proximity to the other fixtures around the pool, symmetric or asymmetric insertion of the control rods, and others.

2.4 Literature Review

Up until this point, a literature review has been done on a variety of topics for this thesis which includes MCNP, MCNP detector designs, detector geometry, tallies that are used in MCNP, ADVANTG weight window generator, working principles of the detectors that are in use in PSBR, the self-powered neutron detectors, and their design and use in MCNP, miniature fission chambers, and Fission Matrix Method.

Accurate power measurement plays an important role in the safe operation of nuclear reactors and are done by in-pool neutron and gamma detectors at the research reactors. The calibration of these detectors is done when there is a change in the reactor core and/or structural materials and is usually done at a single location with important power levels. Other factors, such as; control rod positions, proximity to the neutron moderator material, and reflector will affect the power measurement results. Many recent studies focused on the accurate measurement of power in reactors. The paper [13] by Snoj, L., Barbot, L. investigates the effect of the control rods on the accuracy of the power measurement. According to the authors, asymmetric control rod insertion can significantly affect power measurements due to flux redistribution, indicating that at the same nuclear power, the readings on a single channel can vary by up to 30 % depending on the control rod configuration. With the flux redistribution correction, the authors showed that the relative difference between the theoretical estimate of the factor and the Monte Carlo computed factor can be as large as 8 %. This phenomenon can be observed at PSBR as well since the control rods can be manually controlled and cause a change in flux distribution. According to Heidrich [12], more or fewer neutrons reach the detector depending on neutron flux and pool temperature. As pool temperature increases, the absorption cross-section decreases, and more neutrons reach the detectors, resulting in an indicated power that is higher than the actual power for the fission chambers and the compensated ion chamber. On the other hand, gamma ion chambers are affected only by the changes in the density of the water as it relates to the shielding of gamma-rays, which is very small since density changes are very small in the PSBR. The PSBR thermal calibration method has 1-3% uncertainty at 800 kW which is up to 24 kW. The calibration of the detectors is done at this power level and detector responses are assumed linear with a change of power. The uncertainty on the reactor power level and the method that utilizes the thermal calibration method may be improved using MCNP methods and a new detector response function that will be developed in this thesis.

Another paper by Zagar, T., Ravnik, M., and Pcrsic A. [14] focuses on the analysis of the TRIGA reactor thermal power calibration method. The authors claim that calorimetric power calibration can be significantly wrong if it is performed under uncontrolled conditions. If the calibration is done with high power, where the error can be high as 30%. They implemented experimental calibration factors to correct reactor power measurements. This method can also be implemented by using the MCNP model developed at the PSBR and improving the power measurements which will be discussed in Chapter 7 and Chapter 8.

The calorimetric power calibration is done at constant power where the primary cooling system is switched off and the rate of temperature increase of the water is recorded. The reactor power can be calculated as a function of the temperature increase. Another method is the heat balance method consists of the steady-state energy balance of the primary cooling loop of the reactor. The PSBR reactor thermal power calibration is carried out by the heat exchanger balance method. In this method, the steady-state energy balance of the primary cooling loop is required. The inlet temperature, outlet temperature, and the water flow in the primary cooling loop are measured. Thermal power can easily be calculated using these parameters and the estimated heat losses from the pool. Estimation of the pool heat loss is challenging and may cause uncertainties in the reactor thermal power calibration procedure. Reactor power can be calculated using the heat balance equation shown in

Equation 2-1[12]:

$$q_{Rx} = \dot{m}C_p(T_{in} - T_{out})|HX + q_{Loses} - q_{Pumps} + q_{heat-up}$$

where

$$q_{Loses} = q_{Conduction} + q_{Convection} + q_{Radiation} + q_{Evaporation} \qquad \text{Equation 2-1}$$

and

$$q_{Pumps} = q_{HXS\_Pump} + q_{RS\_Pump} + q_{N-16\ Pump}$$

The heat balance equation parameters are shown in Table 2-1.

Table 2-1. Heat balance parameters that are used in Equation 2-1

q_{Rx}	Thermal energy generated by the reactor operating at 800 kW indicated power
$\dot{m}C_p(T_{in} - T_{out})\|HX$	Heat transferred through the primary loop of the heat exchanger system
$q_{Conduction}$	Conduction through pool walls
$q_{Convection}$	Convection in pool
$q_{Radiation}$	Radiative heat transfer
$q_{Evaporation}$	Evaporation of the pool water from the surfaces
q_{HXS_Pump}	Heat exchanger primary pump
q_{RS_Pump}	Recirculation system pump
$q_{N-16\ Pump}$	N-16 diffuser pump

The thermal losses due to the pool surface and walls need to be calculated. This is very challenging since balancing the system in a steady-state is not always possible and there will be uncertainties in the heat balance method due to heat losses.

Mesquita, A. Z et al. [15], [16] describe the difference between the power calibration method done by two thermal power calibration methods. All the above-mentioned papers can be summarized as power measurement in nuclear reactors done by thermal calibration methods, and detectors are calibrated by the results of thermal calibration processes. These thermal calibrations are designed to be accurate enough, but they are not for every power level since calibrations are only done at certain power levels and can be affected by many factors.

Reactor simulations are a very important aid when it comes to analyzing a tremendous amount of data. Ding, Y. et al.[17] introduces an MCNP code to simulate and calculate the energy response of an ionization chamber. Their findings reflect that the ionization chamber can measure photon radiation energy up to 10 MeV. Kim J. C. et al. [18] compared three different types of ionization chambers that are sensitive to gamma-rays. Their results showed a linear relation between incident particles and simulated electrical output from the detector design. The PSBR detectors can be modeled in MCNP and electrical output measurements can be done in the future.

Simplified detector modeling is a common way to introduce a variety of neutron and gamma detectors into MCNP simulations. These simple models with specific tally cards can calculate detector response due to an incident particle's energy deposition inside the detector region. Theses by Taylor, N.R [19] and Gift, M. [20] looked at a simple MCNP detector design and compared it with experiments. Both theses used a very similar design of ion chambers with a simple cylindrical tube and important interior materials. Gift M. concludes that there is an exposure rate discrepancy between MCNP simulation results and the experiments. Similar to these theses, papers by Coburn, J. et al. [21], Bell, Z. W. et al. [22], and Wallace, J. D [23] focus on ion chamber modeling in MCNP. Coburn, J. et al. implemented a new calibration technique using fission chambers. According to Wallace, J. D., the MCNP package provides an easier development of reliable models to predict detector behavior for different detection systems [23].

Self-powered neutron detectors are widely used for in-core flux measurements at nuclear reactors. They rely on the (n,β^-) reaction and do not need external power to operate the detector. This feature makes them an important aid in monitoring reactor power in accident scenarios. Due to their reaction type, self-powered neutron detectors have a delayed aspect which makes them incompatible for simultaneous reactor power measurement and control. On the other hand, digital compensation methods can be designed for SPNDs to overcome the delayed behavior of the emitter. Turso, J.A, Corak, G. et al. [24] proved that SPNDs can be used in real-time applications with digital compensation methods. The paper by Kópházi, J. et al. [25] focuses on the calculation of the delayed part of the SPND using MCNP. The calculation of delayed aspects regarding the SPND requires detailed electron physics in MCNP which makes it computationally expensive. In steady-state conditions, reactor power can be associated with the (n,β^-) reaction. Rabir, M.H.B, et al. [26] focused on the measurement and simulation of SPND in Malaysian's PUSPATI TRIGA Reactor using MCNP. According to the authors, MCNP overestimates the SPND signal by 20% compared to measurements. Vermeeren, L [27] proved that neutron and gamma sensitivity of SPNDs by the Monte Carlo model matched with experiments. Kim, M.S. published a paper that places 40 Rh SPNDs in the reactor and studies the contribution of the external gamma rays. The paper concludes that this method may lead to accurate power calibrations using self-powered neutron detectors.

MCNP simulations may help the future detector calibration process at PSBR. The power inaccuracy between different locations may be compensated by applying new detector responses calculated by the MCNP code. Investigating each fuel element, the control rods, and the fuel temperature parameters near the D_2O tank, FNI, FFT, and R1 open pool locations will give information about each parameter and eventually lead to more accurate power measurements. By these means, fuel management calculations may be improved and the PSBR would operate more efficiently. This thesis will aim to develop a MCNP model for the reactor core, structural materials, and neutron and gamma detectors. Self-powered neutron detectors and a miniature fission chamber will be implemented into the MCNP model. Different reactor operation parameters and control rods movement will be investigated to analyze detector response and improve power measurements. The above-mentioned papers and theses in the literature review indicated that MCNP is suitable for the detector design and may be used for better estimation of the reactor power for the PSBR.

Chapter 3

PSBR MCNP Core Model and Detector Design-Characterization

This section will describe the Monte Carlo Methods and MCNP. In addition, PSBR MCNP core model development that was updated over multiple years, and detector modeling in the PSBR MCNP code will be explained. The modification needed to be done to the original PSBR MCNP core model to increase the accuracy of the model and reduce computational time. The detectors for the power detection system were installed into the PSBR approximately two decades ago. The documentation of the detectors does not give a complete explanation of the materials and the geometry. Due to this reason, several assumptions have been made and that will be described throughout this chapter.

3.1 Monte Carlo Methods and MCNP

The transport and interaction of radiation in a reactor can be described with two methods: stochastic or deterministic. Stochastic means randomly determined, having a random probability distribution or pattern that may be analyzed statistically but may not be predicted precisely. In a deterministic model, the future events can be calculated exactly, without the involvement of randomness.

In reactor physics, stochastic methods simulate individual particles such as neutrons. Each event that neutron faces have a probability distribution. Reaction rates depend on neutron flux which means, these reaction rates will have uncertainty due to incident neutron probabilities of interaction. However, deterministic methods rely on equations and numerically solve them. In the deterministic method, neutron transport equations need to be solved for neutron flux with different energies. Then reaction rates can be calculated using neutron flux and cross-sections.

Monte Carlo methods are used to model the probability of the different reactor physics parameters and can provide the closest representation of reality since they can use continuous angle and energy variables, and simulate exact geometries [28]. They can be computationally expensive since each particle and its reactions with materials need to be simulated. To reduce the uncertainty of the results, these simulations need to be repeated multiple times with more initial particles. Deterministic methods would be faster compared the Monte Carlo methods since they solve discretized equations rather than simulating each particle. However, the discretization of energy, angle, and space needs to be done perfectly. Having a few groups will lead to significant inaccuracy of the results, however, having too many discretization groups will lead to a complex system with multiple parameters and will cause time and other problems.

Monte Carlo N-Particle Transport (MCNP) is a Monte Carlo radiation transport code designed to track many types of particles over a wide range of energies and was developed by Los Alamos National Laboratory. This code can be used in many fields such as radiation shielding, nuclear criticality calculations, radiation detector design, dose calculations, fission and fusion reactor design, etc. [29].

The code contains several sections to describe cells, surfaces, materials, and various physics that require calculating the desired result. Depending on material and temperature, MCNP calls the cross-section library to calculate desired reaction rate and other calculations. In addition, MCNP contains several useful tally options. These tallies are surface flux, cell or volume flux, point or ring detectors, particle and fission heating, pulse height tally, mesh tallies, and radiography tallies.

MCNP stochastic code requires computational power to simulate complex reactor models. It requires multiple-core, fast and reliable computers to solve various problems. The important thing is that the MCNP can replace expensive and time-consuming experiments. Multiple simulations can be done at MCNP and finalized geometry and material description can be acquired without having any experiments. MCNP is a very popular tool among nuclear engineers.

3.2 MCNP Modeling of PSBR

Several modeling tools have been used over the years for fuel management and experimental design of the PSBR [30]–[34]. The current fuel management code is called TRIGSIMS which is based on using the Monte Carlo code MCNP for particle transport, coupled with the ORIGEN-S code for isotopic depletion. MCNP uses evaluated data for a variety of particles to track them over extensive energy ranges. MCNP contains different tally types that aid in determining desired reaction rates of the isotopes. Flux shape and power distribution within the core can be determined by using specific tally options. The PSBR MCNP model has been developed by graduate students, staff members, and professors many years ago, and new features and core loadings are changing invariably [30]–[34]. This code is mainly in use for burnup calculations, fuel utilization, and new core loadings with cooperating with TRIGSIMS and ORIGEN-S codes [35]. Fuel elements in the PSBR MCNP model are divided into five axial zones to define fuel depletion change on the z-axis. Figure 3-1 illustrates The PSBR full MCNP model incorporating a reactor core, new D_2O moderator assembly, new beam ports (on the top), full pool model, Fast Neutron Irradiator (FNI), and Fast Flux Tube (FFT) which is located at the bottom right [10].

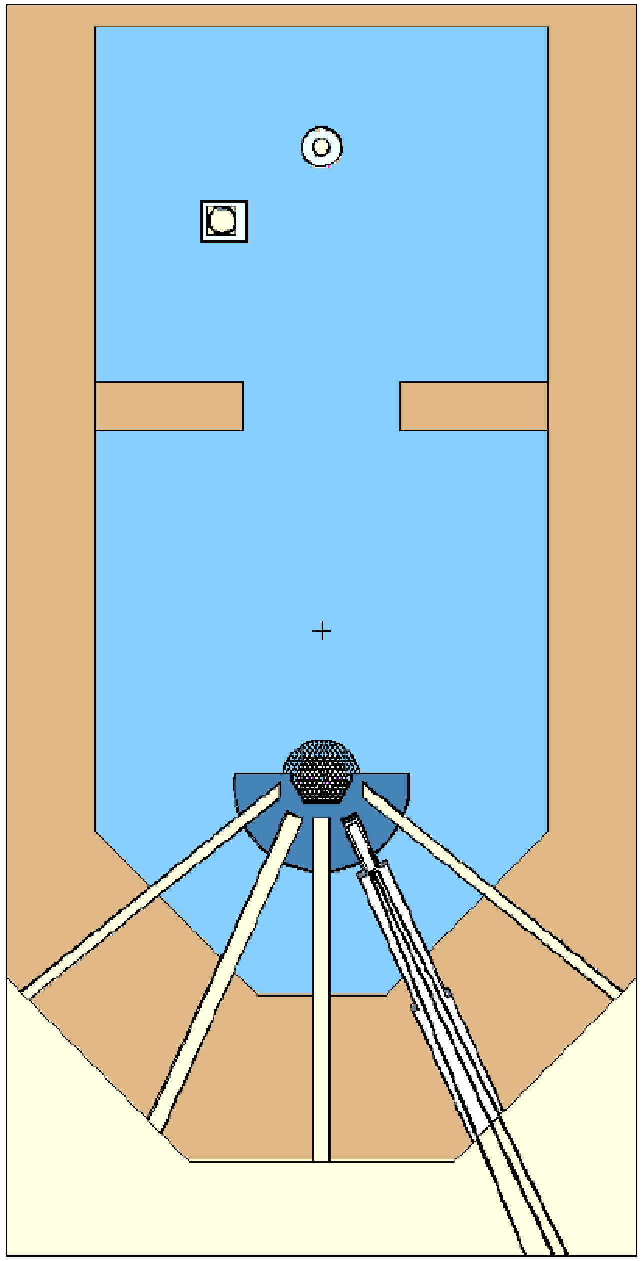

Figure 3-1: Penn State Breazeale Reactor full MCNP model including reactor core, D_2O tank, beam ports, FNI, and FFT [10]

Figure 3-2 represents the core loading 58A map of PSBR [10]. The PSBR utilizes two types of TRIGA fuel. The yellow-marked fuel elements which are 8.5-weight percent uranium, and blue-marked fuel elements are 12-weight percent uranium, both of which are enriched to

19.8%. Green circles represent the control rods whereas pink colored circles represent two dry irradiation tubes.

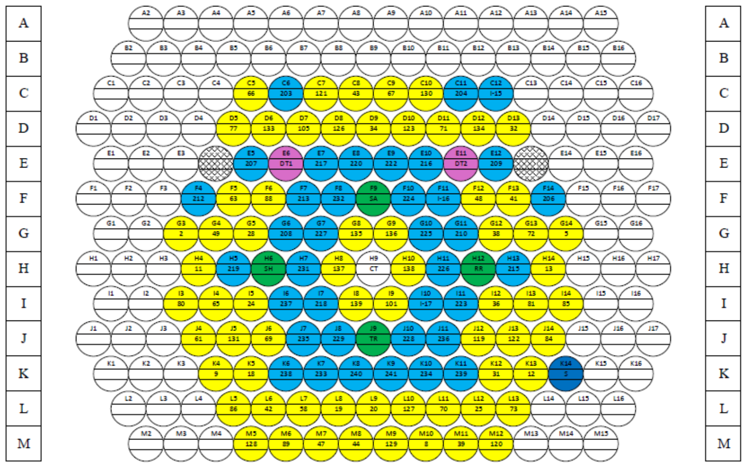

Figure 3-2: Penn State Breazeale Reactor core loading map for version 58A [10]

Figure 3-3 shows the core layout with the new D_2O tank and the beam ports installed during the 2018 renovation [10].

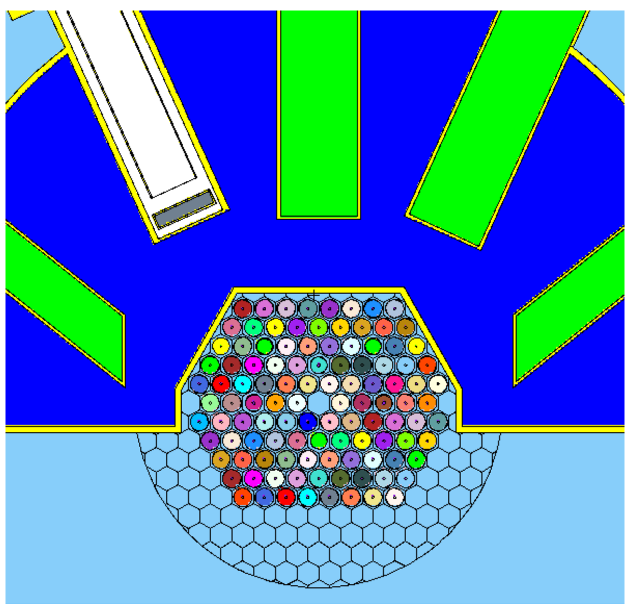

Figure 3-3: A closer look at the reactor core, new D2O tank, and the new beam ports [10]

Future core loadings are done by an automated system developed by Bascom [10]. After every new core loading, several Standard Operational Procedures (SOPs) needed to be conducted including thermal power calibration and detector calibration. The main MCNP model is updated for research needs in this thesis and will be described in Section 3.7.

3.3 Fission Chamber Design in MCNP

The Fission Chamber is a type of ionization chamber that is coated with a small amount of fissile material on the wall of the detector, typically Uranium-235. When an incident neutron is absorbed in the fissile material, it may cause a fission reaction. The fissile nucleus will split into two fission fragments and they will travel in opposite directions due to the conservation of momentum. Therefore, one fission fragment will escape from the detector and the other one will travel into the filled gas region of the detector. This fission fragment will deposit its energy into the fill gas partially or fully. The deposition of energy in the filled gas region will ionize the atoms. Eventually, electrons created in the ionization process will be collected at the inner electrode by applying an external high voltage to the fission chamber. The output generated by the detector will be proportional to the rate of fission events that happened in the detector. That means the output of the detector will be proportional to the neutron flux level at the detector location.

The PSBR has two unguarded fission chambers from Westinghouse-Thermofisher with the serial number WL-23110. Initially, the fission chambers were designed in MCNP as simple cylindrical tubes. The simplified cylindrical tube model of the detectors in MCNP is very common in literature [21], [19]. The electronic parts and some structure-cable materials were not included in the MCNP model. The neutron-sensitive material is a thin layer of U_3O_8 enriched to over 90 w% ^{235}U, placed between aluminum sleeves. The total ^{235}U mass is 0.443 g. Figure 3-4 represents the shape of the fission chamber and the specifications provided by the manufacturer. Figure 3-5 shows the FC design created in MCNP using the specifications in Figure 3-4.

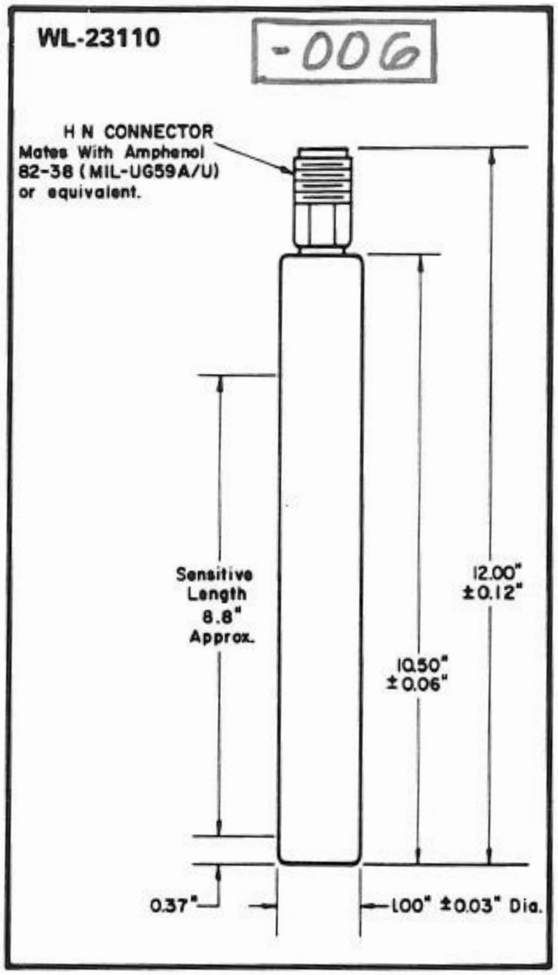

Mechanical	Units	WL-23110
O.D., nominal	Inches	1.00
Length, nominal	Inches	12.00
Sensitive Length, nominal ..	Inches	8.87
Net Weight..............	Pounds	0.4
Shipping Weight..........	Pounds	3.0
Materials		
Outer Case	–	Aluminum
Electrodes	–	Aluminum
Insulation................	–	Al_2O_3
Sensitive Material:		
Amount of U^{235} in U_3O_8	%	>90
Thickness	mg/cm^2	2.0
Total Quantity of U^{235} ..	Gram	0.443
Gas Fill	–	Ar-N
Gas Pressure	cm-Hg	76
Impedance		-006
Resistance, minimum		
(At Max. Temp.)	Ohms	10^9
Capacitance	pF	45
Maximum Ratings		
Voltage Between Electrodes	Volts	800
Temperature	°F	575
External Pressure (note 1) ..	PSI	180
Thermal Neutron Flux:	nv	10^{11}
Gamma Flux	R/Hr	10^6
Typical Operation (at approx. 25° C)		
Operating Voltage	Volts	300
Operating Voltage Plateau	Volts	200-800
Thermal Neutron Flux:		
Lower Limit	nv	6
Upper Limit	nv	6×10^5
Sensitivity (note 2)	CPS/nv	0.18
Output Pulse Characteristics:		
Amplitude (unloaded)....	Volts	2×10^{-4}
Inherent Rise Time (Average)	Seconds	2×10^{-7}

Figure 3-4: Fission chamber dimensions and specifications provided by the manufacturer

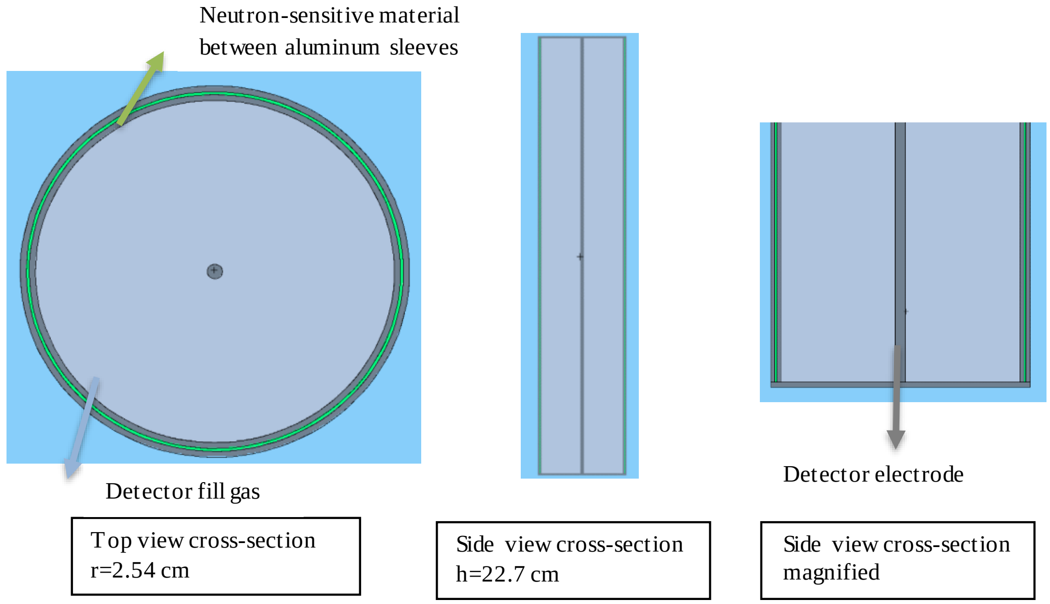

Figure 3-5: Simplified fission chamber design in MCNP, top view, side view cross-section, and side view cross-section closer look

One of the assumption made in this thesis was the simplified detector geometry design in the MCNP. The most important part of the detector is the target material that interacts with neutrons and gamma-rays. Reactor power will be proportional to the fission events that occur in the target region which is investigated with the F4 tally option in the MCNP. Due to this reason, other complex parts of the detector did not get designed in the MCNP code. Even if it is desired to design them into MCNP, there is no geometry specification for that in the documentation.

Consequently, the simplified detector designs will give an accurate estimation of the reactor power since the modeling of the important target region is accurately designed with a description given by the manufacturer.

3.4 Gamma Ion Chamber (GIC) Design in MCNP

The PSBR has two RS-C4-0806-112 type gamma ion chamber detectors in the pool. The first detector provides secondary power input for RSS which is placed in the right bottom corner of the reactor core. The second gamma ion chamber is placed above the reactor core and provides secondary power input. The chamber walls are composed of Al-1100 and the parts are insulated using ceramic insulators. The fill gas is at 76 cm-Hg Nitrogen to ensure gamma rays interact with the gas.

In a similar fashion to the fission chamber design, the simplified model of the gamma ion chamber has been implemented into MCNP as a cylindrical tube. The electrode, outside tube, and nitrogen-filled gas were modeled using the MCNP. Figure 3-6 shows the cross-section of the top and side views of the gamma ion chamber design in MCNP.

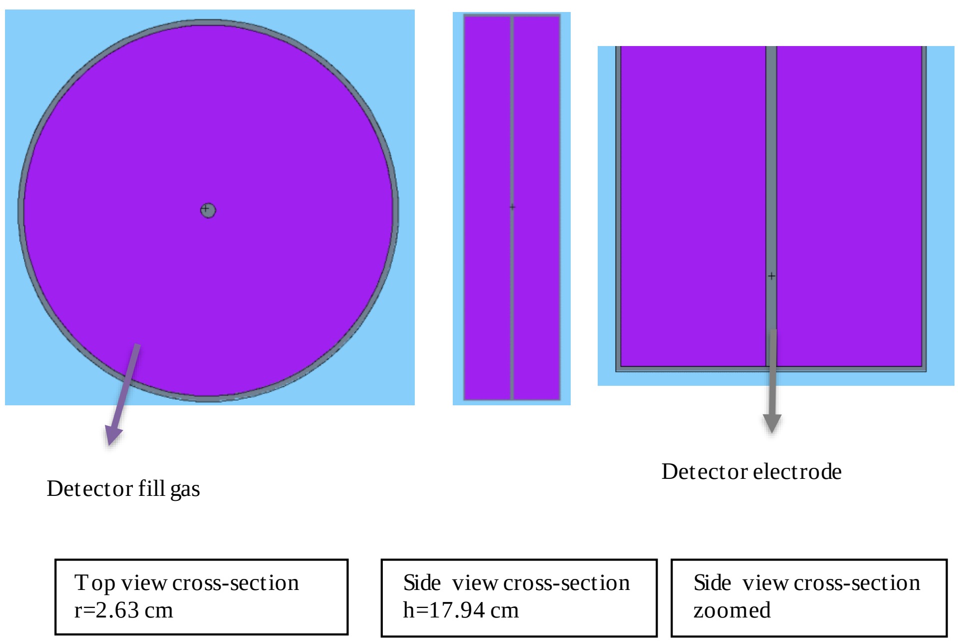

Figure 3-6: Simplified gamma ion chamber design in MCNP, top view, side view cross-section and side view cross-section closer look

3.5 Compensated Ion Chamber (CIC) Design in MCNP

The PSBR has a compensated ion chamber which is an electrically compensated ionization chamber to measure thermal neutron flux outside of the reactor core for intermediate and power ranges. The primary use of this detector is in a mixed neutron and gamma flux where gamma flux is the dominant portion of the total radiation.

A RS-C1-2514-115 type Reuter Stokes CIC is placed into the PSBR. Compensation is provided by a chamber section that is sensitive to gamma-rays only. A negative voltage is applied to the compensating electrode and a positive voltage is applied to the high voltage electrode. Output currents are subtracted electrically and neutron current alone is measured. The CIC has concentric cylinders with a B-10 coating for providing a neutron-sensitive area. Al-1100 has been used for its construction due to its low neutron absorption properties.

Figure 3-7 shows the CIC design in MCNP. The blue material shows the boron coating around the grey Al-1100 material and the electrode is in the middle section. The energy deposition difference between the two cylinders will give a neutron contribution to the CIC detector.

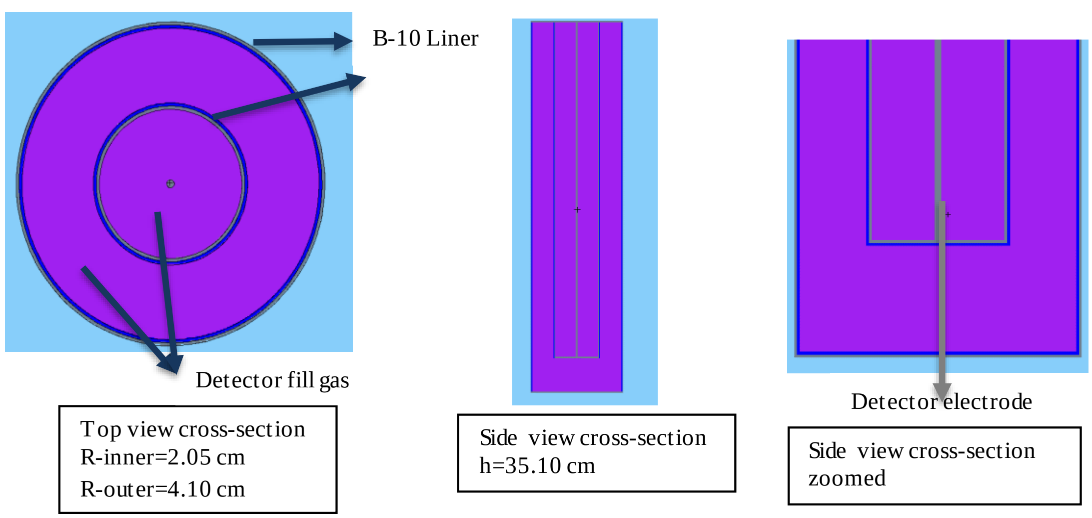

Figure 3-7: Simplified compensated ion chamber design in MCNP, top view, side view cross-section and side view cross-section closer look

3.6 Self-Powered Neutron Detector Design (SPND) in MCNP

A self-powered neutron detector is a device that can measure the neutron flux. This detector utilizes beta emission from the emitter material, which absorbs the incident neutron and does gamma decay. After the gamma decay, delayed beta reaction occurs and this reaction can be measured as a current using an ammeter. This current does not need amplification which makes self-powered neutron detectors a great candidate for reactor power monitoring in emergency scenarios.

SPNDs can be placed near the fuel elements in channels because of their small size. On the other hand, these detectors cannot provide real-time estimates of reactor power due to their internal delay from the beta emission mechanism. They are suitable for reactor monitoring but not suitable for reactor control purposes. Their main advantage over ion-chamber type detectors is that they do not need an external power source to continue operations since beta emission relies only on neutron flux. They also have a high resistance to temperature and pressure. Rhodium, vanadium, and silver-type self-powered neutron detectors are very common. In this thesis, a rhodium emitter was investigated. Figure 3-8 shows the Rhodium-103 decay scheme [36].

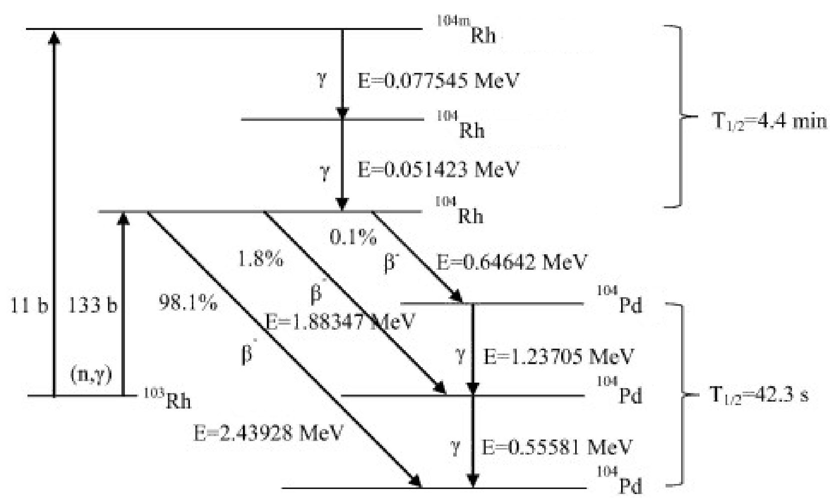

Figure 3-8. Rhodium-103 decay scheme with interaction types and cross-sections [36]

The rate of change in the number of nuclei of isotope X can be described in Equation 3-1:

$$\frac{dX(t)}{dt} = Production\ of\ the\ Isotope\ X - Loss\ of\ the\ Isotope\ X \qquad \text{Equation 3-1}$$

The loss from the decay of the rhodium will be a production of the next stable nuclei in the chain. Rhodium-103 has a high absorption cross-section and shorter half-life which makes it a great candidate for SPND applications. These properties are well suited for identifying flux maps in the PWR systems. However, the relatively high absorption cross-section of rhodium implies that the rhodium SPND will burn out with time, so the emitters should be replaced [7].

Equation 3-2 provides the rate equations developed for the isotopes that result in a rhodium SPND current signal. The important contributors are rhodium-104 and rhodium 104m.

$$\frac{dN_{104m}(t)}{dt} = \sigma_{104m} N_{103} \phi(t) - \lambda_{104m} N_{104m}(t)$$

$$\frac{dN_{104}(t)}{dt} = \sigma_{104} N_{103} \phi(t) + \lambda_{104m} N_{104m}(t) - \lambda_{104} N_{104}(t) \qquad \text{Equation 3-2}$$

$$i(t) = k_{pv}(\sigma_{104}+\sigma_{104m}) N_{103} \phi(t) + k_{gv} \lambda_{104} N_{104}(t)$$

Table 3-1 explains the parameters that are used in Equation 3-2.

Table 3-1: Self-powered neutron detector parameters and constants [7]

N_{103}, N_{104} and N_{104m}	Atomic densities of rhodium-103, rhodium-104, and rhodium-104m
σ_{104} and σ_{104m}	Microscopic neutron absorption cross-section of rhodium-104 and rhodium-104m
λ_{104} and λ_{104m}	Decay constant of rhodium-104 and rhodium-104m
$i(t)$	Current from Self-powered neutron detector
k_{pv} and k_{gv}	Probabilities of rhodium-103 neutron capture and rhodium-104 decay leading to a current-carrying electron
$\phi(t)$	Input flux from the reactor

Figure 3-9 shows the SPND design in MCNP. The inner cylinder represents the rhodium-103 emitter material and the other parts are the structural materials.

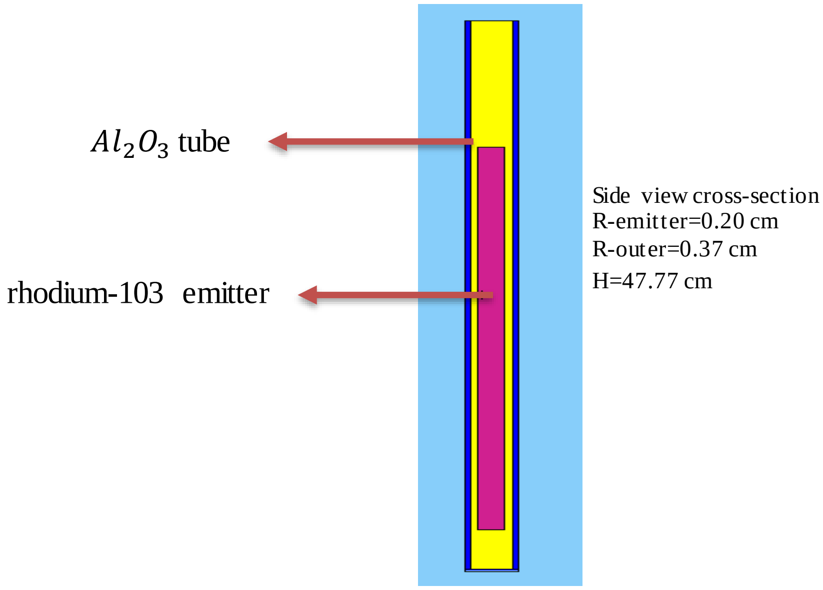

Figure 3-9: Self-powered neutron detector design in MCNP, middle section represents beta emitter material

Twelve self-powered neutron detectors are placed around the reactor core using the PSBR MCNP model to compare neutron flux around the core computationally. These detectors will give results depending on the neutron flux at their location by using the F4 tally option in the MCNP. One self-powered neutron detector is located in the central thimble where the neutron flux is the highest. The last two self-powered neutron detectors are located at dry tube locations. Dry irradiation tubes are air-filled tubes that allow for the placement of experimental tools or samples in real experimental conditions. In the MCNP model, the SPND design changed to be as long as the fuel elements. Five axial cells are defined to investigate neutron flux change with the z-axis, which is important since control rod movements may contribute to higher flux in some cells depending on the axial position.

3.7 PSBR Core Model and Detector Design in MCNP

After finalizing the detector models in MCNP, the detectors are placed in their location. Figure 2-3 and Figure 2-4 show the original drawing and image for neutron and gamma-ray detectors in the PSBR. Figure 3-10 is created inside MCNP and shows all PSBR power detection systems and also SPNDs placed inside dry tubes, a central thimble, and 12 SPNDs around the core.

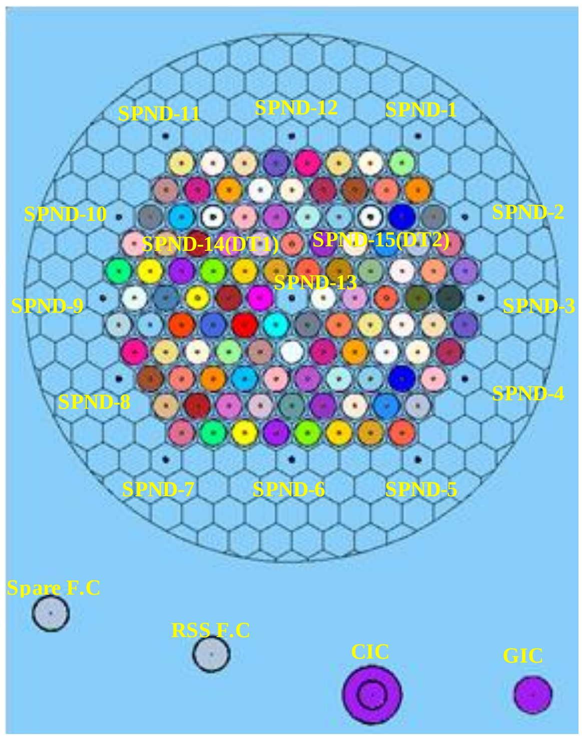

Figure 3-10: MCNP PSBR core model, Fission Chambers, Compensated Ion Chamber, Gamma Ion Chamber, and Self-Powered Neutron Detectors placed in and around the core

In addition to that, preliminary runs showed the important results using the self-powered neutron detectors which will be described in Chapter 4. However, placing 15 different self-powered neutron detectors inside the reactor core is not realistic. It is good the show what would be the possible outcomes of having SPNDs in the reactor core by the simulation methods. Chapter 4 will describe the results of having SPNDs inside the core and how flux shape differs inside and around the reactor core. For the future of the research, these detectors will be removed and only ex-core detectors will be used. After Chapter 6, a new detector, a miniature fission chamber will be introduced to the research and experiments will be done using this detector and the ex-core detectors.

The PSBR MCNP model is modified according to the needs of the research that will be done. The latest updated code has many structural geometries in it which cause an increased run time for the code. To reduce computational time in the simulations, the main code is divided up into four small codes depending on reactor operation positions. These locations are the open pool (R1 Location), D_2O tank, FFT, and FNI. Figure 3-11 through Figure 3-14 shows a simplified MCNP model that will be used in this thesis.

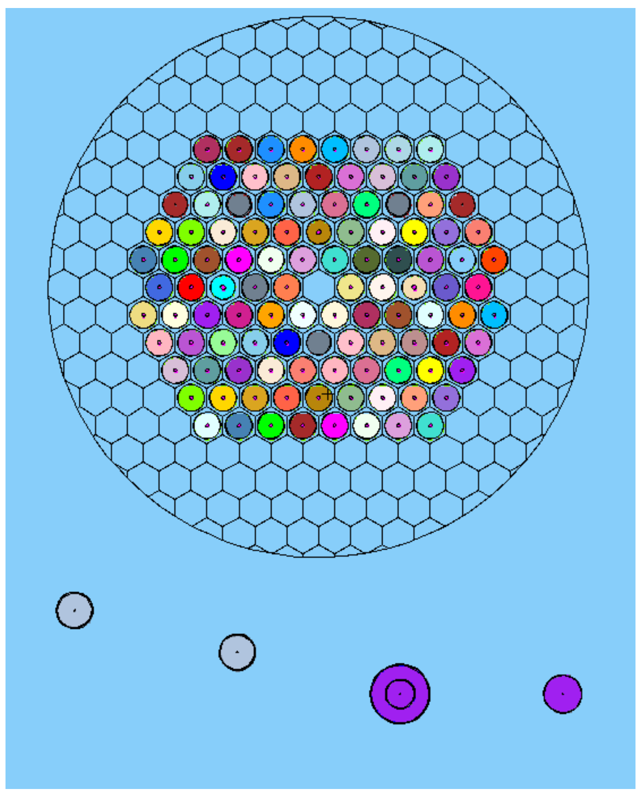

Figure 3-11: Reactor core and detectors where reactor placed at open pool (R1) location

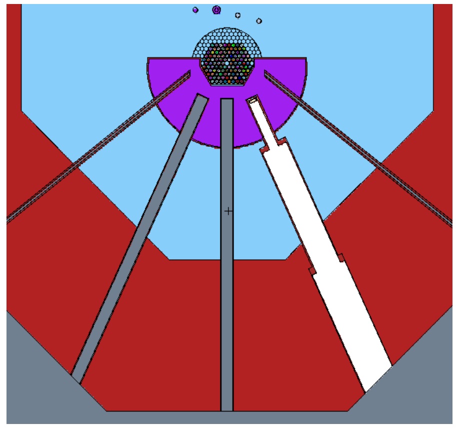

Figure 3-12: Reactor core and detectors where reactor placed at D_2O tank location

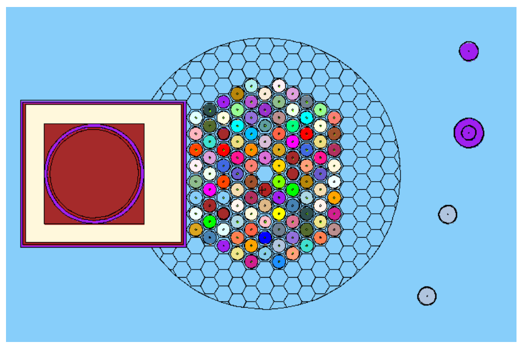

Figure 3-13: Reactor core and detectors where reactor placed at FNI location

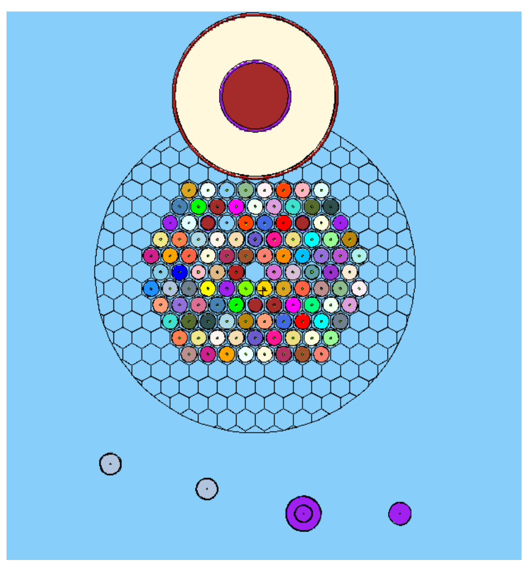

Figure 3-14: Reactor core and detectors where reactor placed at FFT location

Preliminary runs were completed using the R1 open pool location for all detector types in Chapter 4 to show proof of concept. The goal here is the test the behaviors of the detectors using different methods and control rod position changes. After that, a detailed investigation will be done for all locations and with all detectors.

3.8 ADVANTG Automated Weight Window Generation for MCNP Model

The PSBR power detection system detectors are located on the south side of the reactor core. There is a significant gap between the fuel elements and the detectors that are filled with pool water. The neutrons can travel on the order of centimeters in the water which makes calculations challenging due to having a high uncertainty in the results without having a variance reduction technique. At full power, the thermal neutron flux at the central thimble is around $3 \times 10^{13}\ neutrons/cm^2$, and the thermal flux at the detector region is about 6-7 orders of magnitude less.

As the detectors are located on the south side of the reactor core, the neutrons traveling in the opposite direction or not important areas in the water contribute more time to the calculations and the uncertainties. To reduce uncertainties associated with tally results, variance reduction techniques should be implemented into the model. One way to do that is by implementing the AutomateD VAriaNce reduction Generator (ADVANTG) software. ADVATNG software automates the generation of variance reduction parameters for continuous energy Monte Carlo simulations using MCNP5 [37]. ADVANTG generates space and energy-dependent mesh-based weight window bound and biased source distributions from three-dimensional discrete ordinates calculations that are performed by the Denovo package [38]. ADVANTG is used in many applications to reduce both the user effort and the computational time required to obtain accurate and precise tally estimates.

ADVANTG has a Consistent Adjoint Driven Importance Sampling (CADIS) method and the Forward-Weighted CADIS (FW-CADIS) method to generate variance reduction parameters. The CADIS method was developed for accelerating individual tallies and the FW-CADIS method can be applied to multiple tallies and mesh tallies [37]. The FW-CADIS method has been shown to produce relatively uniform statistical uncertainties across multiple cell tallies and mesh tallies [39]. FW-CADIS method was designed to span the range from a few localized tallies to space and energy-dependent mesh tallies that cover the entire domain. This is accomplished by weighting contributions of all tallies described in the input deck and creating an adjoint source. The weight can be calculated by taking the inverse of each individual response:

$$q^{+} = \frac{1}{R_1}\sigma_{d,1} + \frac{1}{R_2}\sigma_{d,2} + \cdots + \frac{1}{R_N}\sigma_{d,N} \qquad \text{Equation 3-3}$$

The total response is a sum of equal-weight terms:

$$R = \langle q^{+}, \phi \rangle = 1 + 1 + \cdots + 1 \qquad \text{Equation 3-4}$$

Weight targets are then computed in proportion to the inverse of the adjoint scalar flux:

$$w(P) = \frac{R}{\phi^{+}(P)} \qquad \text{Equation 3-5}$$

Denovo is used to calculate the adjoint flux distribution at the tally points. MCNP input files are read by the ADVANTG, and the user defines important regions such as detector tallies into the input file. Then, this method focuses on these regions of the problem. The cells of each mesh have a particle weight lower limit cutoff. When a particle enters the cell with less than that lower limit, it goes through a roulette process. Depending on the ratio of particle and cell weight cutoffs, the particle will either be terminated or its weight will be increased while it continues to be tracked. When a particle's weight is higher than the weight cutoff of the cell, the particle will have divided into multiple particles. These particles will be individually tracked by the system. However, the total weight will be kept equal to the original weight, thus there will be no bias in tallies calculated using these particles. By this method, in the important regions, more particles will be tracked, and statistical uncertainties will be reduced.

ADVANTG 3.2 code was used to create weight window parameters into MCNP using the FW-CADIS method and weight window constants; important regions can be seen in Figure 3-15 and Figure 3-16. An example of the ADVANTG input file is shown in Appendix.

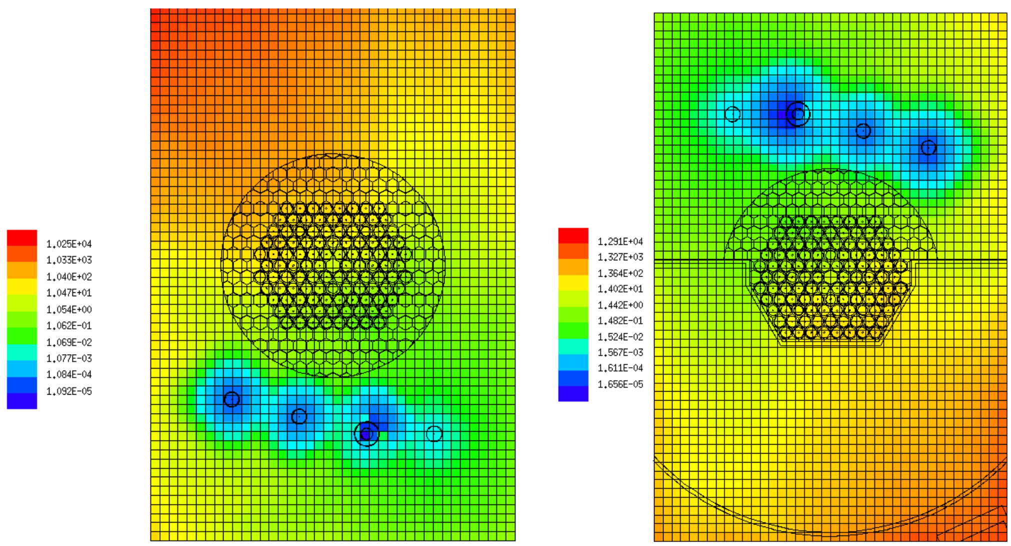

Figure 3-15: ADVANTG weight window map for R1 and D_2O tank locations

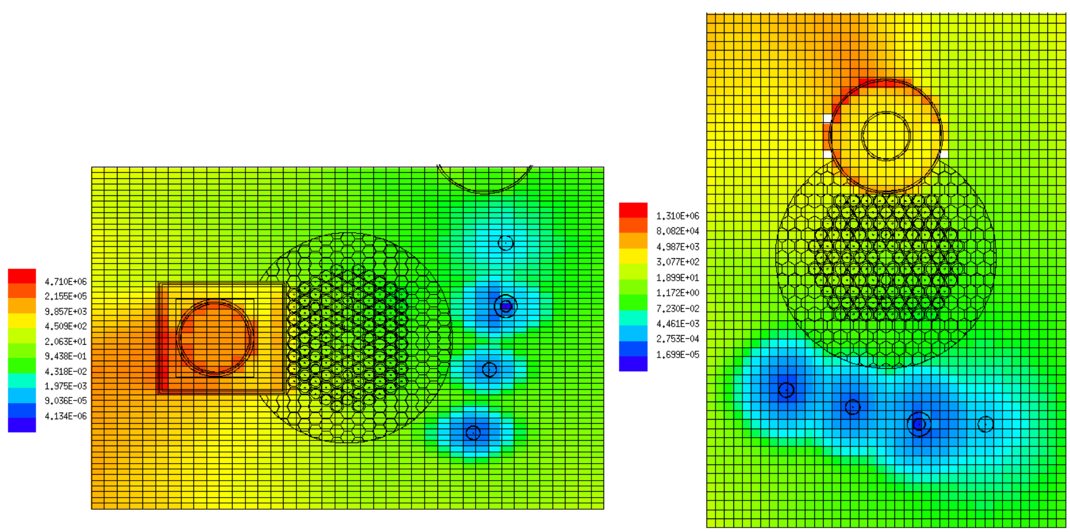

Figure 3-16: ADVANTG weight window map for FNI and FFT locations

Chapter 4 investigates the case of having weight window and no weight window cases and how they affect the tally results. Uncertainties associated with tally results reduced significantly. In addition, the Figure of Merit (FOM) was used as a metric to compare how fast the simulation was completed with these uncertainties. The MCNP Manual defines FOM as in Equation 3-6:

$$FOM = \frac{1}{\sigma^2 \times T} \qquad \text{Equation 3-6}$$

where σ = relative error and T = computer time in minutes [29]. FOM is a good indication when comparing multiple simulations run on the same computer hardware. The FOM also increased, which is an indication of how fast the simulation results with low uncertainties. All results from the ADVANTG will be explained in the next chapter.

3.9 Visualization Tools for MCNP Results

This research contains multiple investigations and a huge data set produced by the MCNP. Just looking at the data set and trying to compare it with other data sets is not possible without the aid of plotting. During the research, several scripts for organizing the data and plotting them were required. MCNP has built-in plotting software that plots tally results. Unfortunately, this plotting software is hard to use and is not user-friendly. Figure 3-17 shows an example of a flux distribution at center of the core using MCNP built-in plotting software.

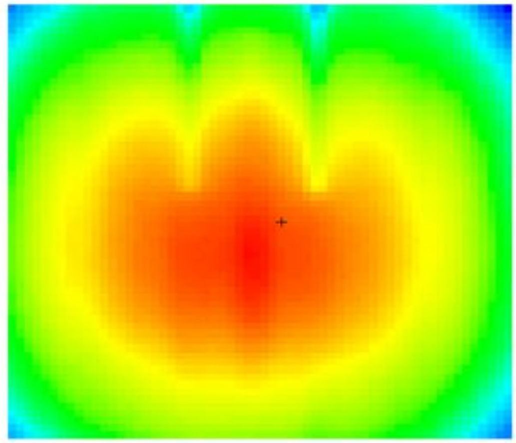

Figure 3-17: An example flux distribution at center of the core using MCNP built-in plotting software.

As seen in Figure 3-17, there is not enough color detail, and it does not allow for color scheme changes. It only allows the user to observe very basic tally results. A new method using MATLAB is introduced to the scripting to see better flux shape in 3D and will be explained in the next section.

3.9.1 3D Mesh Tally Visualization

To better visualize the 3D mesh tally results, a MATLAB® script has been written to plot the neutron flux in 3D. This MATLAB® script reads the mesh tally output of the MCNP code. After that, the script requests input from the user about the desired neutron energy, and cross-section information about the view (top view, side view) by defining XY, YZ, and XZ planes, and creating 3D visualization of the neutron flux map.

Three different neutron energies were implemented into the MATLAB® script: fast, thermal, and total neutron flux which are the options that users can pick and plot depending on the cross-sectional view.

The 3D mesh plot visualizes the highest and lowest neutron flux levels depending on the location and the tally result of the MCNP with color mapping. The blue color represents the low neutron flux and the red color represents high neutron flux levels.

Figure 3-18 through Figure 3-20 shows the thermal neutron flux per source particle (MCNP tally result) at z=0, y=0, and x=0, respectively. The MATLAB® script may help users to better understand and visualize the neutron flux profile at PSBR with different input parameters.

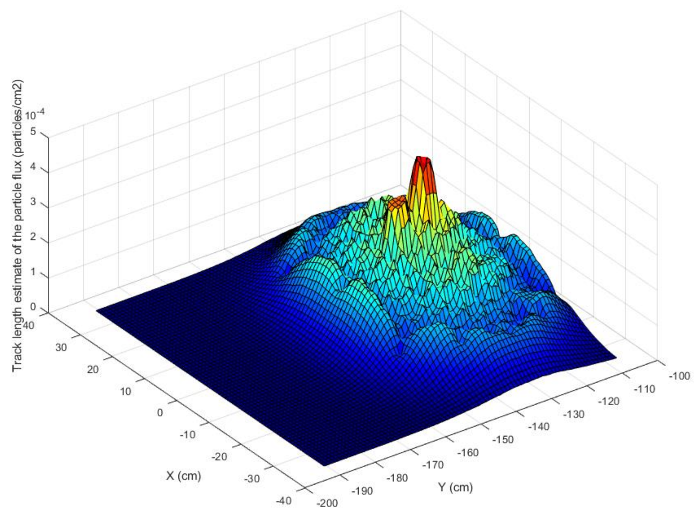

Figure 3-18: 3D MATLAB®flux plotter for thermal flux at z=0

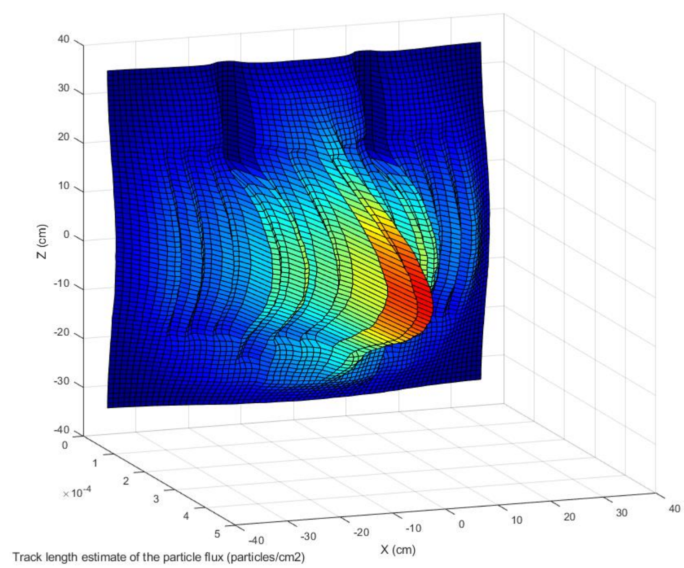

Figure 3-19: 3D MATLAB®flux plotter for thermal flux at y=0

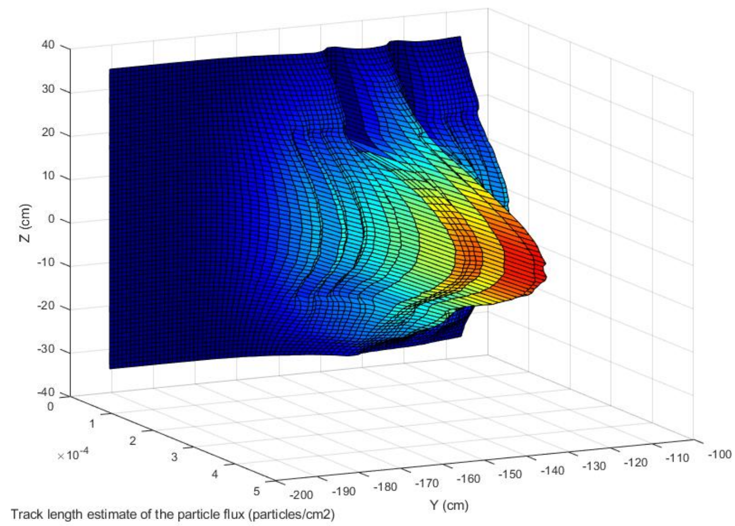

Figure 3-20: 3D MATLAB®flux plotter for thermal flux at x=0

From Figure 3-18 to Figure 3-20, the thermal neutron flux profile changes with control rods, and the fuel elements can be seen. In addition, this code has the ability to compare two different inputs of thermal neutron flux. The code can compare two different input files such as two different control rod position effects on neutron flux and can plot the difference in neutron flux.

3.9.2 Individual Detector Tally Visualization

The current model has fifteen self-powered neutron detectors with five axial regions and, four in-pool detectors. Which make eighty different tally result for the MCNP result. Processing and visualizing all of these tallies is challenging. Therefore, a MATLAB® script was written to organize all of these data sets and then compare them. This code reads the individual MCNP tally results and plots detector responses depending on the source fuel element and the control rod distance from the base of the fuel. This visualization script is used for future sections to plot detector responses.

A simple individual fuel element tally contribution to the spare fission chamber visualization plot is shown in Figure 3-21.

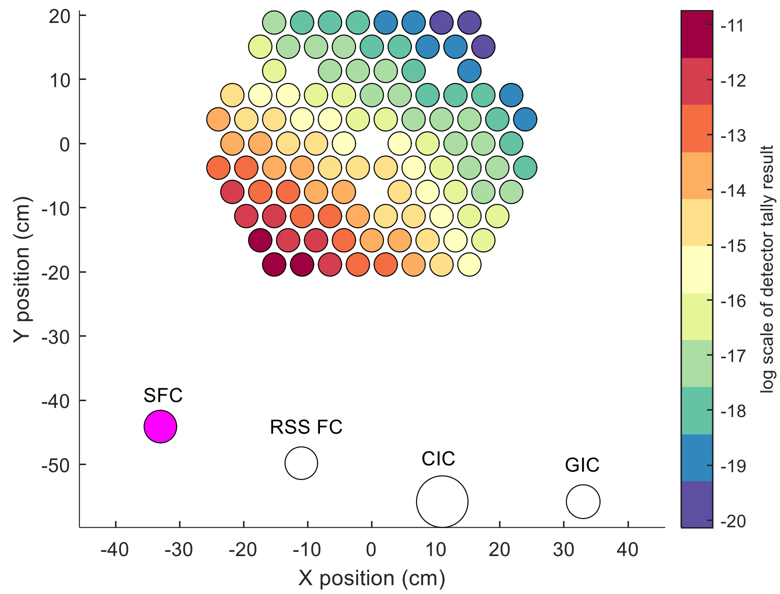

Figure 3-21: An example plot for individual tally response to spare fission chamber at R1 location in logarithmic scale

This plotting and several scripting tools created in MATLAB and Bash environment are used throughout the project to process and plot the results of desired investigations.

Chapter 4

MCNP Model Modes and Detector Response Models

This chapter will describe how MCNP is used throughout this thesis. Since MCNP has a variety of different methods, cards, and tallies to solve a problem, detailed research has been done to pick the best approach for the entire set of calculations.

4.1 MCNP Modes, Options and Tally Cards

MCNP has different modes that activate or deactivate various physics options for neutron and photon transport. Users can define the desired mode depending on the problem. There are two main modes in MCNP to run the input file; KCODE and NPS (fixed-source). The KCODE card specifies the MCNP6 criticality source that is used for determining the effective criticality parameter, k_{eff} , which is also known as the neutron multiplication constant and eigenvalue of the reactor [29]. The KCODE calculations aim to compute the eigen distribution of the fission source. NPS fixed source history cutoff can be used with detector response applications with source definition cards (SDEF). The SDEF card is used for the definition of the source particles' energy spectrum, angle, and location. The NPS is the way to finalize the MCNP runs by giving the final particle number. MCNP will stop when it reaches the NPS value of the total particle number. Tally results should be normalized depending on the reactor power level which is related to the number of fissions in the reactor since fission neutrons are the source.

In MCNP, the user can select which particles will be investigated and transported for the problem. Users can define particles inside the mode card, and the code only transports particles defined in the mode card. Since this research focuses on neutrons and photons, the mode card is created for the neutron and photons. By default, mode *n, p* does not account for photo-neutrons but does account for neutron-induced photons [29]. Mode *n, p* problems generate bremsstrahlung photons with a thick-target bremsstrahlung approximation [29]. If secondary electron transport had been used instead of this approximation, the computer time would be much longer. In the thick-target bremsstrahlung approximation, electrons are generated, then immediately, Bremsstrahlung photons are generated without transporting electrons [40]. In this way, expensive electron transport will be eliminated. With the default physics card, no fluorescence from photoelectric interactions is produced, no binding effects are used for photon scattering, and no coherent scattering is included. Various photon physics may be turned on or off. This physics can greatly affect the runtime since MCNP tries to track every particle in the system, especially electron transports [41]. For this research, photon physics is used as default since prompt gamma-rays are important to estimate reactor power at a steady state.

Tally cards are created for each detector region. These detector tallies give results depending on the input: particle type, energy, interaction type in the cell, etc. For fission chambers, the F4 neutron track length estimated tally is used with a tally multiplier card (FM). This tally multiplier card multiplies the neutron flux with the fission cross-section and gives the fission reaction rate per particle inside the detector region. In the gamma ion chamber, the F6 energy deposition tally is used. This tally records energy deposition inside the detector cell by the photons. The compensated ion chamber looks at the neutron-alpha reaction in the B-10 coating using an F4 tally and the FM multiplier card. Finally, the F4 tally with the FM card is created for self-powered neutron detectors. These tallies are specified by looking at the ^{103}Rh (n,γ) reaction, which can happen inside the emitter material of the self-powered neutron detectors. The detector response can be assumed to be proportional to the tally results. In literature, there are many applications of MCNP detector modeling by using simple geometry with important parts and using F4 and F6 tallies to compare experimental results [21],[19]. Since MCNP is a radiation transport code, it cannot simulate electronic noise or the efficiency of the detection system. But these parameters can be determined experimentally and be compared to the results of MCNP. This will allow for improvements to the detector response functions.

By default, with the neutron physics model, delayed gammas from fission products are ignored. This means that almost half of the gamma rays produced in the reactor are ignored. To investigate the difference between having those ignored gamma-rays, preliminary KCODE runs are done with 10,000 particles and 500 cycles for each case. To include delayed gamma-rays, the Activation Control Card (ACT) should be used in MCNP. This card tracks interactions that may cause delayed gamma-ray emission. On the other hand, this card can only be used with one task, which makes computation times very high. The results can be seen in Table 4-1

Table 4-1: MCNP particle mode comparison with and without ACT card using 500 cycles, tally results represents reaction rate per source particle

Detector Type	Mode: n,p without ACT card		Mode: n,p,e without ACT card		Mode: n,p with ACT card	
	Tally Result	Uncertainty	Tally Result	Uncertainty	Tally Result	Uncertainty
RSS Fission Chamber	2.50E-05	0.0811	1.94E-05	0.0885	2.12E-05	0.0925
Spare Fission Chamber	1.11E-05	0.1182	1.26E-05	0.1023	9.83E-06	0.1199
Compensated I.C Outer	2.10E-05	0.1045	2.07E-05	0.1178	2.66E-05	0.1024
Compensated I.C Inner	8.20E-07	0.4116	9.64E-07	0.3099	2.94E-06	0.2857
Gamma Ion Chamber	1.74E-07	0.0349	3.14E-07	0.1440	2.72E-07	0.0232
Total Computer Time	1143.58 min		1575.14 min		1103.54 min	
Wall Clock Time	56 min		67 min		18h 40 min	
Number of cores	40		40		1	

*10000 particles with 500 cycles

Table 4-1 shows the results for different MCNP modes. The calculation times are extremely high for electron transport and delayed particles (ACT) because, this calculation is not allowed in multithread, which means it can be only run in a single core. Due to this reason, the ACT card was removed from the input, and the electron transport model is excluded for future runs to make them shorter. Electron transport is also not included in future research since causes more computation time and high tally uncertainties. The assumption made here is that the GIC tally is directly proportional to prompt gamma rays. Since each case will have the same type of geometry design and variables that change with fission will be the same, GIC results would be proportional to each other.

4.2 Neutron Flux Investigation with Control Rod Movement

For the preliminary runs, the control rod movement effect at the periphery of the core is investigated. Control rod insertion would disturb and tilt the neutron flux distribution inside and outside of the core. Since ex-core detectors are located at the south-side of the reactor core, they will be affected by the control rod movement. To see this effect, an imaginary cylinder with 6 axial zones is created near the detector region which can be seen in Figure 4-1 for the Core loading 58A.

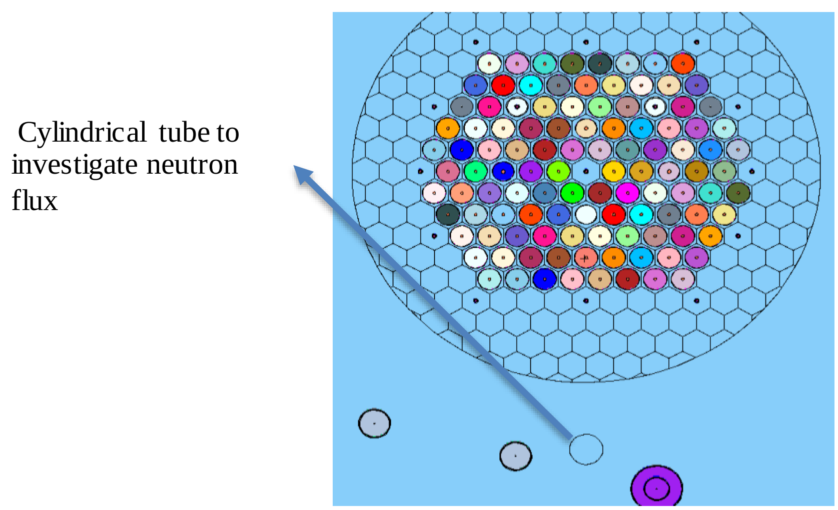

Figure 4-1: A Cylindrical tube placed outside of the core region to investigate axial neutron flux levels

The F4 flux tally KCODE simulation is done for this hypothetical water-filled cell. Figure 4-2 shows results from the flux levels inside the cylinder located outside of the core. Control rod positions were changed to match important operation power levels taken by core loading 58. Axial disturbing of the flux shape is shifting with decreasing power through the detector region.

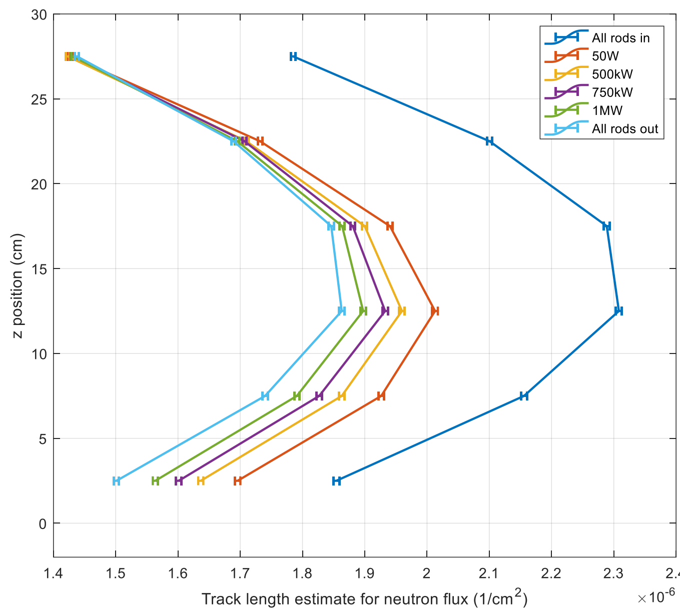

Figure 4-2: Track length estimate of neutron flux change per source particle with the position for different control rod power levels

Since the control rods are inserted from the top, the axial flux distribution will shift toward peaking in the lower core. This effect will be investigated in Chapter 5 with more particles and with more details.

To investigate the neutron flux distribution in the core, the mesh tally method is used in MCNP. A 3D mesh has been created and it can be seen in Figure 4-3.

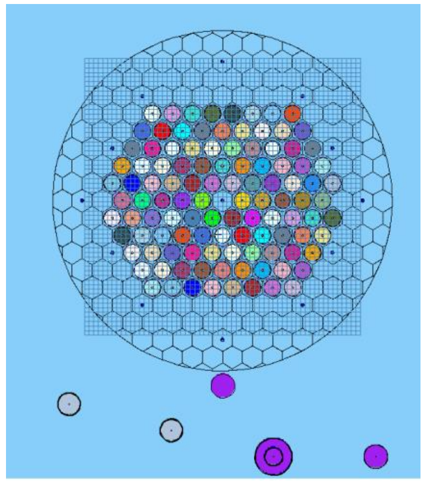

Figure 4-3: 3D mesh tally created by MCNP code that creates a flux map for the reactor core

This mesh covers the entire fuel region and the neutron flux can be seen inside the mesh in Figure 4-4.

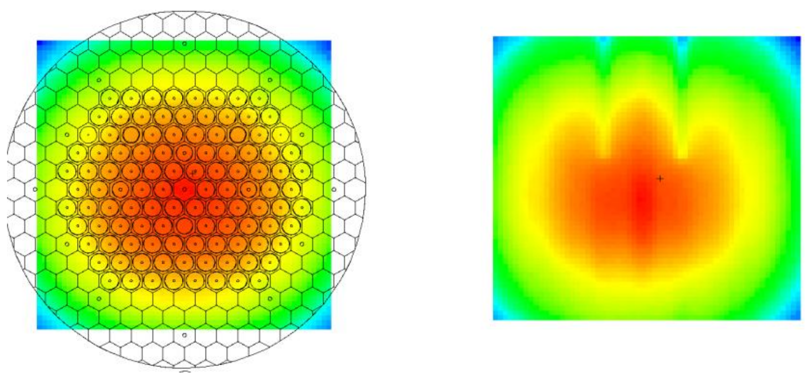

Figure 4-4: Flux heat map created by the MCNP plotting software. Red is the region of highest neutron flux and blue is the lowest

Comparisons are done for the different control rods, and they proved that when control rods are inserted, flux is suppressed to the outside of the core region, which gives higher results for detector tallies per source particle. Since the primary goal of this thesis is to investigate detector behavior change with the neutron flux, this mesh tally is expanded until it covers to detector region. Previous figures show the neutron flux in a heat map, but upcoming calculations will be displayed using alternative visualization using MATLAB®.

4.3 Investigation of ADVANTG Weight Window Generator

Preliminary results showed high uncertainties due to short computation times with KCODE calculations, and it's difficult to see if there is a significant effect from the control rod position for the non-ADVANTG runs. The errors are relatively high since neutrons cannot travel great distances in water and detectors are located outside of the core. This problem can be overcome by increasing the number of particles and cycles. On the other hand, this caused more computational time for the runs. The ADVANTG weight-window generator model was introduced into MCNP to reduce uncertainties for the detector results. For preliminary results, the control rod position change effect was investigated for the detectors with and without the ADVANTG weight windows by placing control rods at the all rods out and all rods in positions. The effect of control rod position change will be thoroughly investigated in Chapter 5.

In the beginning, all of the calculations were done at an open pool location to compare different methods. First, KCODE calculations were done for the open pool location. These KCODE calculations were chosen to have a high number of particles to reduce uncertainty. The main focus of these KCODE calculations is implementing the weight window file generated by the ADVANTG. With the same amount of particles, the code runs similar input files with and without ADVANTG weight window file to compare the importance of the variance reduction. Later, the effect of the control rod position on a fission source was investigated. This is accomplished by creating a translation card for each control rod. These translation cards require user inputs to change the control rod position axially. For preliminary runs, two cases were investigated: all-rods-out (ARO) where all control rods were withdrawn from the reactor core by 38.1 cm, and all-rods-in (ARI) where all control rods were inserted into the reactor core.

Table 4-2 and Table 4-3 show the comparison of the KCODE calculations by weight window and control rod position for different detectors. Tally results represent reaction rates per source particle. Relative change between weight-window and no weight-window results are shown with the ratio of the FOM for both calculations.

Table 4-2: Comparison of the KCODE weight window and control rod position calculations for core loading 59 where all control rods are withdrawn

	KCODE WW ARO		**KCODE No WW ARO**		**Relative Change of Tally Results**	**Figure of Merit Ratio**
	Tally Result	Relative Unc.	Tally Result	Relative Unc.		
RSS FC	3.64E-07	0.0028	3.59E-07	0.0423	1.39	194.06
Spare FC	2.02E-07	0.0034	1.94E-07	0.0495	4.12	180.08
CIC	2.37E-05	0.0032	2.27E-05	0.0369	4.40	113.13
GIC	1.82E-07	0.0052	1.80E-07	0.0115	1.11	4.15

Table 4-3. Comparison of the KCODE weight window and control rod position calculations for core loading 59 where all control rods are inserted

	KCODE WW ARI		**KCODE No WW ARI**		**Relative Change of Tally Results**	**Figure of Merit Ratio**
	Tally Result	Relative Unc.	Tally Result	Relative Unc.		
RSS FC	4.39E-07	0.0025	4.47E-07	0.0343	1.79	173.00
Spare FC	2.45E-07	0.0032	2.40E-07	0.0431	2.08	166.75
CIC	2.88E-05	0.0029	2.80E-05	0.0331	2.86	119.61
GIC	2.02E-07	0.0047	2.00E-07	0.0107	1.00	4.75

Comparing the calculations using weight window and no weight window options, uncertainties are increased between 10-30 times. Relative changes are under 5% for having and not having the weight window method. The weight window mostly focuses on the detector region, thus without the weight window, particles got lost without reaching the detector region. This proves the importance of using weight windows to reduce uncertainties. There is also no major difference between the detector results, and thus KCODE weight window will be used for the calculations.

According to the results, FOM improved around 194 times in all rods out case for the RSS fission chamber. The improvement can be observed in all of the detectors. The lowest improvement seen in the gamma ion chamber due to change in uncertainty is not great as other detectors for using weight window.

Compared to the control rod position change effect on the detector responses, the ARI case has higher tally results compared to the ARO case per source particle. These numbers need to be normalized for each power level. When the control rods are at the all-rods-in position, higher detector tallies occur per source particle. This can be explained by a flux profile shift towards to the detector region from the reactor by inserting the control rods, which is described in Section 4.2

4.4 Effect of Individual Fuel Rods on Detector Responses

There are over 100 different fuel elements currently loaded in the PSBR. Each fuel element contains low enriched uranium; 8.5 wt% U and 12 wt% U [10]. Fuel burnup levels are different for each fuel element due to many fuel loadings and shuffling since the PSBR was first loaded with TRIGA fuel in 1965. This will affect neutron flux and contribution to the detectors with different distances from each fuel element. Reactor power measurements can be affected by the source distribution. Fuel elements closer to the detector region may contribute more to the detector response whereas those further away may contribute less. The goal is to investigate the individual fuel element contribution to the detector region by creating an SDEF card. This may give a better understanding of power measurements and improve burnup calculations for future core loadings. This can also be used to estimate the detector responses due to a given source distribution, for example, as calculated by newly developed fast-running fission-matrix models for the PSBR.

The individual effect of rod spatial location will be investigated in this section. To investigate individual fuel element contribution to the detector region, a source definition (SDEF) card was created for each fuel element. The location of each fuel element is different which affects the contributions to the detector responses due to the distance between the fuel element and the detector. The fission turnoff card (NONU) is also used in fixed source calculations. With this card, fission will not be included in calculations and only source importance will be investigated. Fixed-source calculations allow the user to define when the calculation will end by defining the number of particles that will be transported.

In the first part of the research, the goal is to investigate those fuel elements with different control rod positions. There are six different control rod positions defined in the research which correspond to the important power levels. Having more than 100 fuel elements requires more than 1000 different runs to be done incorporating all the control rod positions and fuel elements. Every run gives several output files which makes it harder to process such data. To ease this run process, a script was written in BASH which creates input files depending on the source locations and automatically runs for all cases and puts output files into the separate folders. This BASH script is improved for future simulations and needs to prepare the input files and process outputs files for data extraction.

Initial runs were done with 100,000 particles with a fixed source calculation for each fuel element with six different control rod positions. Tally uncertainties associated with those runs are fairly high since 100,000 particles are not enough for reactor calculations. However, the tallies with high uncertainty will also be those with the lowest contribution to the detectors. The goal is to compare these runs with ADVANTG model calculations to prove how effective the weight windows model is in MCNP.

Some of the individual simulations were completed for each fuel element and compared in Table 4-4 for the RSS fission chamber. The purpose is to compare some important fuel elements with and without ADVANTG code and to see how individual fuel elements contribute to detector results. The fuel elements picked for this section can be seen in Figure 4-5.

Table 4-4: MCNP individual fuel element tally results in reaction rate per source particle from comparison with ADVANTG and without ADVANTG for RSS fission chamber

Fuel Element	Control Rod Position(cm)	ADVANTG Option	Tally Result	Uncertainty	Computer Time	Figure of Merit (FOM)	FOM Ratio
47	32.5	**With**	**1.89E-04**	**0.0048**	**376.26**	**113.200**	**123.17**
		Without	1.76E-04	0.0703	220.19	0.919	
	0.0	**With**	**1.89E-04**	**0.0048**	**374.54**	**113.600**	**123.61**
		Without	1.76E-04	0.0703	220.13	0.919	
208	32.5	**With**	**1.87E-06**	**0.0414**	**219.07**	**2.661**	**221.75**
		Without	5.27E-07	0.5981	241.03	0.012	
	0.0	**With**	**1.94E-06**	**0.0414**	**200.52**	**2.915**	**265.00**
		Without	5.01E-07	0.6255	222.11	0.011	
239	32.5	**With**	**1.26E-05**	**0.0155**	**288.33**	**14.490**	**301.87**
		Without	9.18E-06	0.3059	221.53	0.048	
	0.0	**With**	**1.25E-05**	**0.0155**	**288.74**	**14.410**	**300.21**
		Without	9.18E-06	0.3059	221.34	0.048	

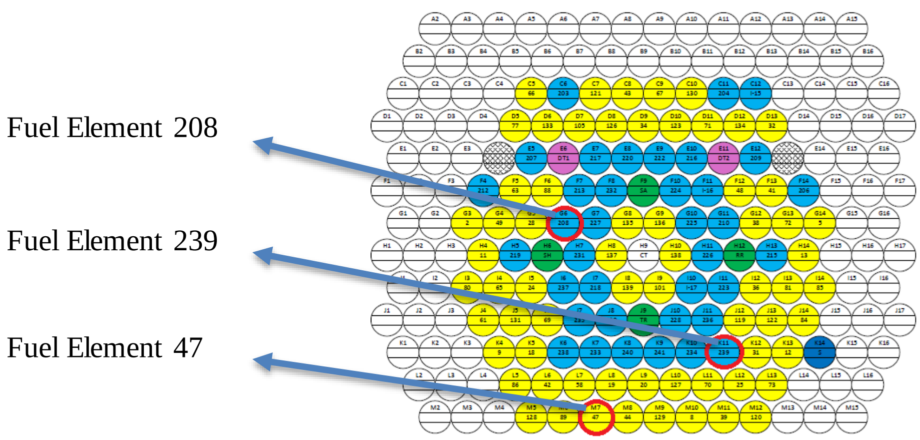

Figure 4-5: Fuel elements picked for the comparison

The results prove how important the fuel element proximity is to the detectors. This can be explained by the fast and thermal neutron range, whereas the distance increases, there is less of a probability that the neutrons will reach that location. Results also showed that the ADVANTG code reduces uncertainties for all fuels and will be used for future simulations. The Figure of Merit (FOM) also indicated that the ADVANTG runs have a higher figure of merit compared to the without ADVANTG runs, which computationally run faster with low uncertainty.

4.5 Methods to Calculate Detector Responses

This section describes how the detector response results are calculated with various methods. Fission source distribution can be acquired with different methods such as SSW calculation, KCODE calculation, and also Fission Matrix Method using Serpent. In addition to that, this chapter will describe detector response function development with the FMESH method and individual detector response functions.

4.5.1 Fission Source Distribution using KCODE

Fission Source Distribution can be created by different methods. MCNP KCODE mode is used in this section to create the fission source distribution. In this mode, KCODE looks at criticality calculations with an initial guess. Each detector has a different tally option that multiplies the reaction rate with the neutron flux per source particle calculated by the KCODE method. This tally result includes the neutron flux due to the fission source, the volume of the cell, cross-section data used for the interaction, and the average neutron released per fission.

The KCODE method tally results were later compared with the other fission source distributions such as SSW-SSR, FMESH, and Fission Matrix Method in sections 4.6.2 and 4.6.3.

4.5.2 Surface Source Write and Read Method (SSW-SSR)

MCNP has a card that initially runs KCODE calculations to create a surface source using the SSW card. This card is used to write a surface source file for use in a subsequent MCNP6 calculation to save time in future calculations. Volume source calculations are done by defining cell numbers in SSW and SSR files which can be done with fission source methods. The initial

SSW run should have enough particles to reduce uncertainty in future simulations. The only drawback of this method is that SSW runs can only be done with a single core, which means it does not allow simulation in multiple core systems, hence causing longer computational times. After the SSW run is completed, MCNP creates a source file named WSSA. The users need to rename the WSSA file as RSSA to use in future SSR calculations.

The SSR card uses the surface source file that was created by SSW calculation. The number of particles of the SSR calculation will be related to the number written to the WSSA file during the SSW calculations which means normalization between the calculations is conserved. Users can specify a different value on the NPS card in the SSR input file compared to the SSW input file. In this case, if the NPS value is smaller than the initial calculation, some tracks will be rejected. If the values are larger than the initial calculation, some tracks will be duplicated. For example, if the SSW calculation used an npp value of 100 and the SSR calculation used an npp of 200, then every track is duplicated, each with a different random number seed and each with half the original weight. Note that a larger value of npp on the SSR calculation will indeed lower the tally errors until the weight variance contained on the RSSA file dominates. Therefore, a user should maximize the number of tracks on the RSSA file. Because the npp value can readjust particle weights as described above, some variance reduction parameters (e.g., weight-window bounds) may need to be renormalized for SSR applications [29].

A SSW input file was created for the R1 open pool simulations. This file contains an SSW card that contains each fuel element cell number. After the SSW KCODE calculation is done, the SSR file created with the same cells and the SDEF card is removed from the SSR input file since it only requires the RSSA file created by the SSW simulations. Results are investigated and compared in Section 4.6

4.5.3 Combining Individual Fuel Element Response with Fission Source

The main goal of this thesis is to develop a method to understand behavior of the detector in different operation conditions. To do that, individual fuel element response to each detector and fission source distribution need to be investigated. Individual fuel element response can be acquired using fixed source calculation for each fuel element, as is described in Section 4.4.

Investigation of the individual fuel element response is crucial since closer fuel elements would have higher contribution to the detector response compared to the fuel elements further away to the detector region which is proved in Section 4.4. PSBR has more than 100 fuel elements, which contain 5 axial fuel regions created by the MCNP code. Therefore, more than 500 individual runs need to be completed to investigate all contributions to each detector taking into account the axial difference in each fuel element. A script is written in BASH to prepare all of the necessary input files. This script reads each fuel element location from the input file and writes it into a new input file by replacing the SDEF card. Then the script executes the MCNP code. After individual runs are completed, this script extracts the tally output for all detectors for each run and puts it into the .txt file. Finally, all data is processed by the MATLAB code to create a detector response function using the FMESH method.

For each fuel region *i* in the reactor, a fixed-source calculation is performed to determine the detector response $R_{i,j}$ in each detector *j*. The detector response function can be found in Equation 4-1.

$$DRF_{i,j} = \frac{R_{i,j}}{S_i} \qquad \text{Equation 4-1}$$

Source distribution S_i , can be obtained by MCNP FMESH or faster methods such as the Fission Matrix Method [4]. Then, the response in each detector, R_j can be determined by summing up the responses due to each fuel region and shown as Equation 4-2.

$$R_j = \sum_i DRF_{i,j} S_i \qquad \text{Equation 4-2}$$

These results have been used successfully by other researchers [5], [42] to couple with fission-matrix source distributions. This allows the detector responses to be calculated easily without having to perform a full transport solution in MCNP, which is computationally very time-consuming. The detector response functions for each fuel element have uncertainties due to their distance to the detectors. The further fuel elements have less contribution to the detector response and have high uncertainty. This is similar to the fission source. The uncertainty in the detector response is calculated by the multiplication uncertainty, which is the contribution of the source and detector response function's uncertainty. The total uncertainty in the detector response can be seen in Equation 4-3.

$$\Delta R_j = \left(\sum_i DRF_{i,j} S_i\right) \times \sqrt{\Delta DRF_{i,j}{}^2 + \Delta S_i{}^2}$$

$$\Delta R^2 = \sum_i \Delta R_j{}^2 \qquad \text{Equation 4-3}$$

MCNP calculates the Detector Response Function uncertainty for each fuel element. Similarly, the FMESH method and Fission Matrix Method uncertainties for each source are calculated by MCNP and Serpent. Finally, the total uncertainty for the FMESH and Fission Matrix method is calculated by Equation 4-3.

The fission source distribution uncertainties can get as low as possible with FMESH and Fission Matrix Method by running high particle numbers. The uncertainties associated with the fission source are less than 0.5%. The main contributor of uncertainty in the detector responses comes from detector response functions. These functions are designed for all fuel elements with axial regions and simulations which are done using the SDEF method for all fuel elements. The fuel elements closer to the detectors have high tally results with low uncertainty. In addition to this, fuel elements further away from the detectors have small tally results with high uncertainty. Due to this reason, the main uncertainty comes from the detector response function. For a simple example, the following results are shown for the RSS fission chamber FMESH result for the reactor power at 1000 kW and the reactor located at the open pool in Table 4-5.

Table 4-5. Uncertainties due to source distribution and individual fuel element detector response function

	Uncertainty (%)
σS_i	0.0503
σD_i	0.2129

The uncertainty due to detector response functions is greater than the source distribution uncertainty which is shown in Table 4-5. The main contribution of the uncertainty to the FMESH results will come from detector response functions and will be seen in Chapter 5.

4.5.3.1 Fission Matrix Method

The goal of this chapter is to show the detector response functions with different methods. To achieve this, KCODE, NPS, and SSW-SSR were developed for PSBR core loading 59 using MCNP.

In previous work by Rau, a fission-matrix method was developed to quickly (much less than 1 second) calculate the reactivity and power distribution of a system, including temperature and control feedback effects. This method can be can also be combined with the detector response function of each fuel element in order to quickly estimate detector responses under various conditions, as discussed in section 4.6.2.

A fission matrix is composed of the number of fission neutrons available in volume 2 that will be created from a fission neutron created in volume 1 [28]. The fission matrix's eigenvalue and eigenvector are the multiplication factor and the fission source, respectively. Rau

[28] proved that tallied fission matrix data can be reused to estimate a fission matrix for a different system. This is important since users do not require performing an additional criticality simulation. With the method developed by Rau, a set of fission matrices can be pre-calculated for a range of temperatures and control rod positions, and then later be interpolated and solved for any state, i.e., temperature distribution and control rod position. Rau implemented this method into a python code, which is used here in this work.

The calculation of fission matrix databases for the Fission Matrix Method was carried on in Serpent 2 Monte Carlo model. Rau used the “set fmtx” option in Serpent for tallying fission matrices since it works in conjunction with a criticality simulation. The thesis by Rau focuses on early core loadings with fresh fuel, but also core loading 58, which consists of used fuel elements that were also simulated to prove Fission Matrix Method would work for the nonuniform fuel loadings. Early core loadings such as core loading 4 feature an earlier design of the D_2O tank in a box shape and can be seen in Figure 4-6.

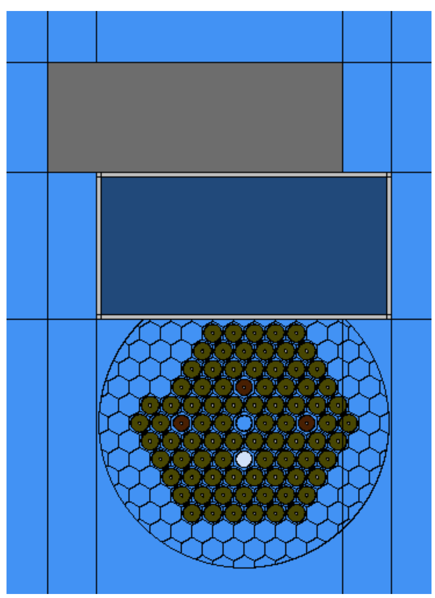

Figure 4-6. Core loading 4 and D_2O Tank, dark blue is moderator and gray box is graphite reflector

The analysis by Rau was done for Core loading 58 for R1 open pool location only, and a detailed geometrical update was required to run future core loadings. A python code was created by Rau to convert TRIGSIMS model outputs for updated core loadings.

In this work, the previous python code was used to create Core loading 59 input files for the Serpent, which is the current core loading. The code reads the TRIGSIMS model and creates three files that contain information about the cell, material, and pin definitions. After conversion, the user can run Serpent with updated geometrical and material information. Figure 4-7 and Figure 4-8 show the core loading 59 translated into the Serpent model.

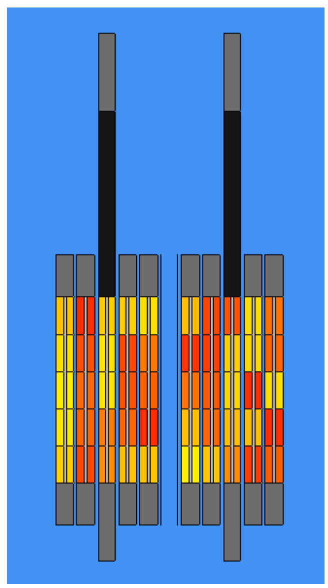

Figure 4-7. R1 open pool Serpent model from the front view

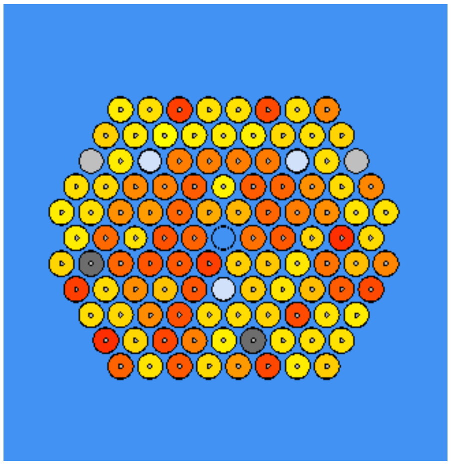

Figure 4-8. R1 open pool Serpent model from the top view

Using this updated Core 59 model, a new fission-matrix database was created using a set of uniform temperatures and control rod positions. For this work, uniform fuel temperatures of 300, 400, 500, and 600 K were used, as well as uniform control rod positions at 0%, 20%, 40%, 60%, 80%, and 100% insertion.

In addition to that, the newly built D_2O tank model from 2019 was implemented into the main Serpent model, based on the existing MCNP model of the tank. Figure 4-9 and Figure 4-10 show the reactor core coupled with the D_2O tank from the front view and top view.

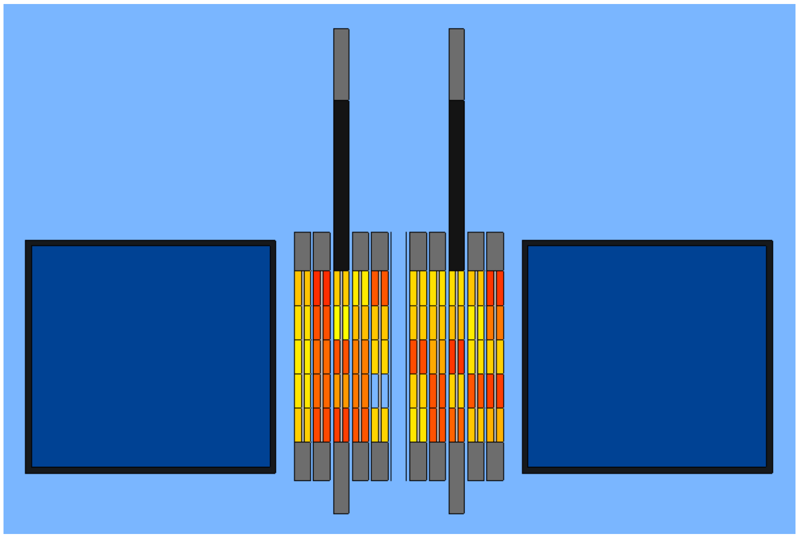

Figure 4-9. Serpent D2O Tank and Core Model from the front view

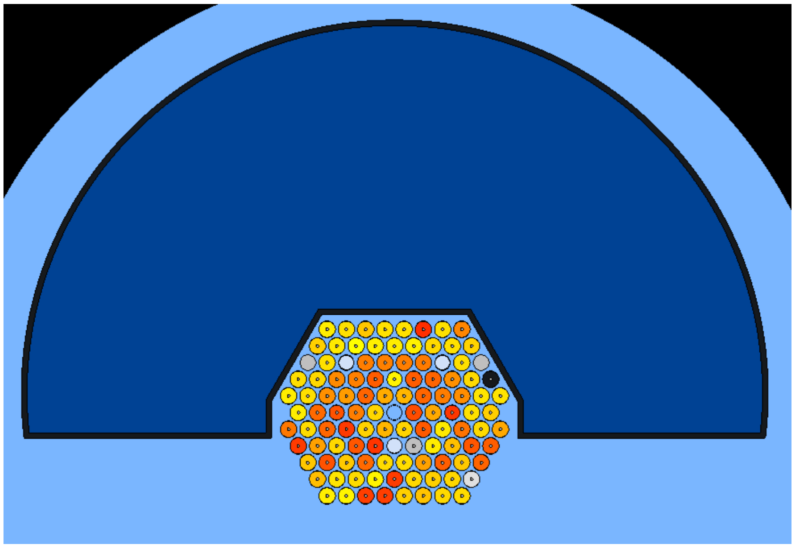

Figure 4-10. Serpent D_2O Tank and Core Model from the top view

After the model was completed, preliminary runs were performed to create data for the fission matrix method. Rau developed a method to include the previous D_2O tank using a correction factor, and this method was used here, but the data was updated using the new D_2O tank model. In order to calculate this correction factor, calculations were performed with and without the D_2O tank, and the Fission Matrix was stored for use in Rau's code. The comparison will be explained in section 4.6.2.

4.5.3.2 FMESH Method

MCNP FMESH tallies can be configured with different orientations, such as cylindrical, XYZ, etc. A mesh can be superimposed on the reactor core location and results are written to a separate output file with the default name meshtal. The mesh tally calculates the track length estimate of the particle flux averaged over a mesh cell similar to the F4 flux tally. In this thesis, box shape meshes are superimposed over the reactor core. Each fuel element is surrounded by 4 mesh bins which are summed by MATLAB code. Due to the asymmetry of the FMESH indexes, the MATLAB script is updated to get correct results by calculating the distance from the center of the fuel element to the center of the closest four FMESH bins. Figure 4-11 shows an example of superimposed mesh over the reactor core.

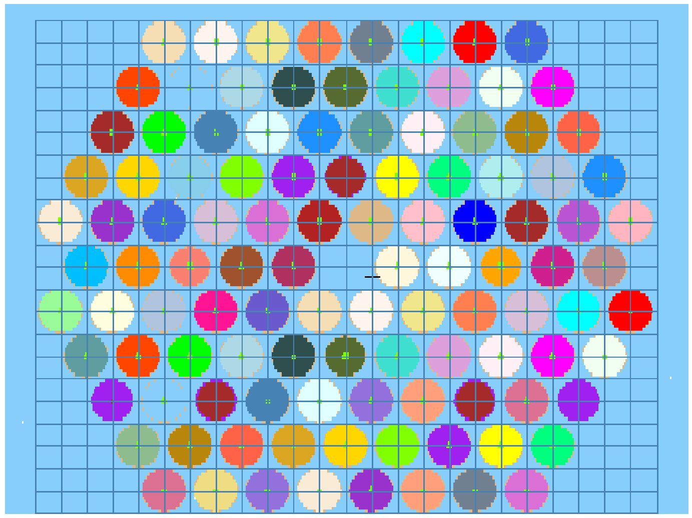

Figure 4-11. Superimposed FMESH tally over the reactor core fuel region

An FMESH tally is created over the reactor core which gives the source distribution over the mesh created. The results are normalized per source particle and need to be re-normalized by multiplying with an appropriate factor that takes into account reactor power. All of these methods will be compared in the next section.

4.6 Comparison of Different Methods

Different methods are utilized to understand detector behaviors in preliminary calculations. It is necessary because relying on only one method will not prove the accuracy and the reliability of the model.

4.6.1 Investigation of Single Fuel Element Response Using Different Methods

The goal of this section is to show the effect of different methods on detector response due to a single fuel element. During the DRF calculation, it was assumed that the source was uniformly distributed within a single fuel region. In reality, this will be not uniform, and this section seeks to quantify the error introduced as a result of the uniform source approximation.

Two fuel element candidates were chosen in this section. The first one is fuel element 872 which is located in the middle section of the reactor core between the transient rod and regulating rod. The second one is fuel element 1122 which is located on the south edge of the reactor core especially close to the RSS fission chamber. Figure 4-12 shows the location of the fuel element 1122 and fuel element 872 with reference to the reactor core and detectors.

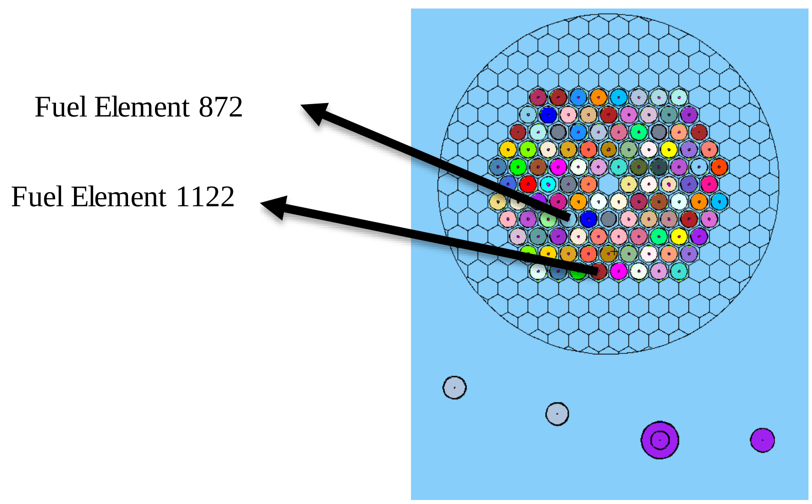

Figure 4-12: Two candidate fuel element that picked for analysis where fuel element 872 closer to the center of the core and fuel element 1122 is closer to the detector region

A comparison is done between these two fuel elements using a fixed source calculation where the source definition is defined as inside the fuel element region. This method is called the uniform source calculation method. Next, it is important to understand what is going on inside these fuel elements. It is expected that the region inside the fuel element that is facing the detector region should contribute more than the region that faces the opposite side. To investigate this, the fuel element's source distribution is divided into two regions. It is done by splitting the input file in two and defining the y- dimension as two halves of the circle. This method is called the split source method and a simple geometrical description can be seen in Figure 4-13. The north region is where the fuel element faces to detector region and the southern region is the region that faces the opposite side.

Figure 4-13: A simple geometrical description of the split source method

These two methods rely on the fixed source calculation and the source definition that is defined inside the fuel region. These two methods will be also compared with the SSW-SSR method with the same approach.

In the SSW-SSR method, the same fuel elements are defined in the SSW card with a KCODE calculation. The weight window file was removed for the runs of SSW because weight-window bounds generated in a SSW calculation are not useful in the SSR calculation [29]. The SSW method can be only run in a single core. This means that for the uncertainties less than 1%, it requires code to run for 5-6 days for the PSBR model using a single processor. After the SSW calculation is done, MCNP creates a source file named WSSA which has to be renamed to RSSA before using it for SSR calculations. In SSR calculation, the fuel element cell number defined in the SSR card and source description card is removed since it will read the source file from the SSW results. SSR calculations are done in minutes since it can use multithreading with 40 processors. Since the number of particle histories are different for a SSW and SSR, proper normalization needs to be done to make comparisons between the SSR, uniform, and split source methods. To do that, results are divided to k_{eff} values and normalized FMESH values. Table 4-6 and Table 4-7 show the results for comparison of these three different methods for fuel element 872 and fuel element 1122, respectively.

Table 4-6: Comparison of the Split Source, Uniform Source and SSW-SSR method tally results on fuel element 872 per source particle

	Split Source South/North		**Split Average**	**Uniform Source**	**SSR Normalized**
RSS FC	2.13E-07	1.54E-07	1.84E-07	1.80E-07	1.82E-07
Spare FC	3.77E-08	3.16E-08	3.46E-08	3.24E-08	3.37E-08
CIC	3.14E-05	2.24E-05	2.69E-05	2.75E-05	2.60E-05

*Uncertainties are less than 6% for Uniform and SSR, less than 1 % for Split Source

Table 4-7: Comparison of the Split Source, Uniform Source and SSW-SSR method tally results on fuel element 1122 per source particle

	Split Source South/North		**Split Average**	**Uniform Source**	**SSR Normalized**
RSS FC	4.85E-06	3.37E-06	4.11E-06	4.10E-06	4.19E-06
Spare FC	9.49E-07	7.32E-07	8.41E-07	8.38E-07	8.89E-07
CIC	2.24E-04	1.60E-04	1.92E-04	1.92E-04	1.91E-04

*Uncertainties are less than 3% for Uniform and SSR, less than 1 % for Split Source

The F4 tally results represent the number of neutrons per cm^2 per source particle. This number is about an order of magnitude higher for the fuel element 1122 since it is closer to the detectors and because there is a higher chance to reach the detector active region compared to the fuel element 872.

The investigation is also done for the split source method. For both fuel elements, the south section of the fuel has a higher tally result compared to the north section. This can be explained similarly, since the north region is closer to the detector region, there is a higher chance the neutrons interact with the detector target material.

Finally, comparing the three methods, the results are matched within the uncertainty levels. The highest discrepancy between the three methods occurs in the spare fission chamber, which is the furthest detector compared to the fuel elements that are investigated. This can be explained by the same logic as the previous paragraphs, i.e., distance is higher, leading to less chance to do interaction in the detector and higher uncertainties.

4.6.2 Comparison of the KCODE calculation versus FMESH and Fission Matrix Method

Individual fuel element calculations are taken from Section 4.4. These calculations contain all detector tally data using a SDEF card of the fuel regions and NPS. All data is processed by the script created by BASH and MATLAB. Figure 4-14 shows the sample individual tally response to the RSS fission chamber for the open pool location in both logarithmic and linear scales.

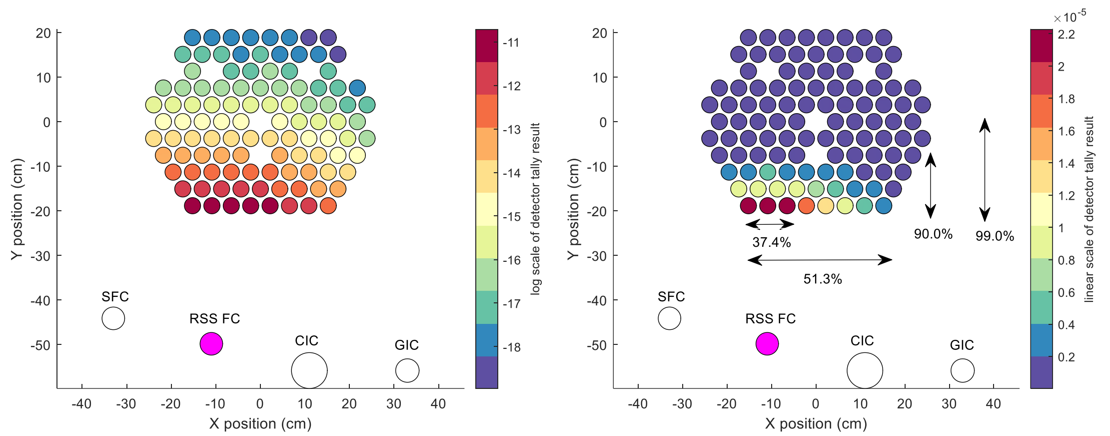

Figure 4-14. R1 Open pool individual tally contribution to the RSS fission chamber, log and linear scale

The highest contribution to the RSS FC comes from the first-row fuel elements. The contribution decreases when the fuel elements become distant. The individual tally results from each fuel element need to be multiplied by the source distribution of the reactor core. Two methods can produce source distributions for this thesis. Initially, the source distribution is taken from the FMESH superimposed tally from the KCODE calculation. Then, it was taken from the Fission Matrix Method developed by Serpent 2. In theory, results from the multiplication of the detector response function and fission source should match with the KCODE calculation tally outputs. Table 4-8 shows the results for the comparison of different methods. These results were taken from Core loading 58A. The uncertainties are less than 0.5% for all cases.

Table 4-8: Comparison of the KCODE-WW calculation versus FMESH and Fission Matrix Method per source particle for core loading 58A when all control rods are out

Detector	KCODE-WW	FMESH Method	Fission Matrix Method	Relative Difference	
	Tally Result	Result	Result	KCODE WW-FMESH	KCODE WW-FM
RSS FC	3.68E-07	3.43E-07	3.43E-07	7.29	7.29
Spare FC	1.82E-07	1.70E-07	1.71E-07	7.06	6.43
CIC	2.19E-05	2.06E-05	2.05E-05	6.32	6.83
GIC	1.69E-07	1.70E-07	1.69E-07	0.59	0.00

*Uncertainties are less than 0.5% for all cases

Figure 4-15 shows the relative fission source distribution over the fuel elements for the FMESH and Fission Matrix Method when all rods out from the reactor core for the core loading 58A. Figure 4-16 shows the locations of each fuel element and numbers.

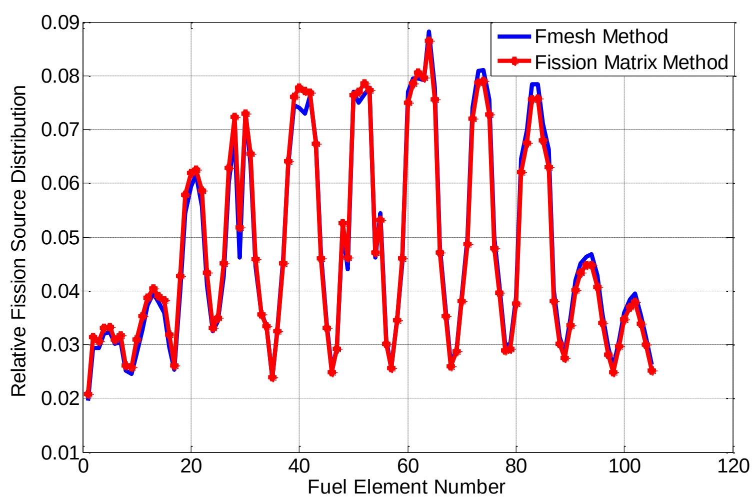

Figure 4-15. Relative fission source distribution over fuel elements for the FMESH and Fission Matrix Method when all control rods are out for core loading 58A

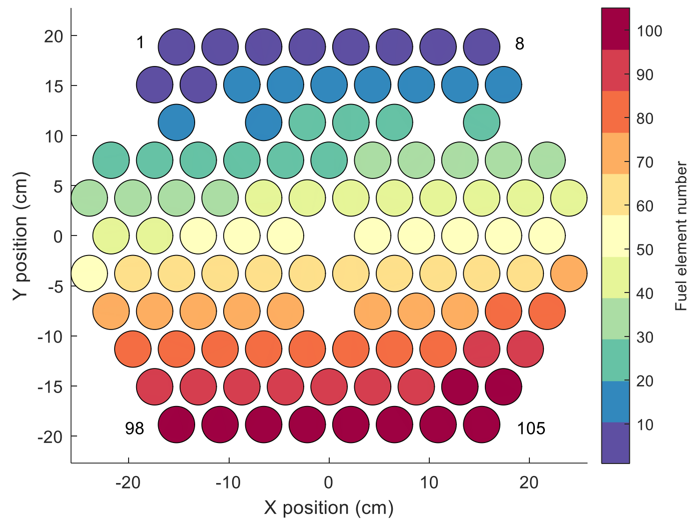

Figure 4-16. Fuel element numbers in 2D view

Similarly, another control rod position change was investigated to show that both methods match well with each other in term of fission source comparison. Figure 4-17 and Table 4-9 show the fission source comparison of the FMESH and Fission matrix method where control rods are inserted 9.525 cm for the core loading 58A.

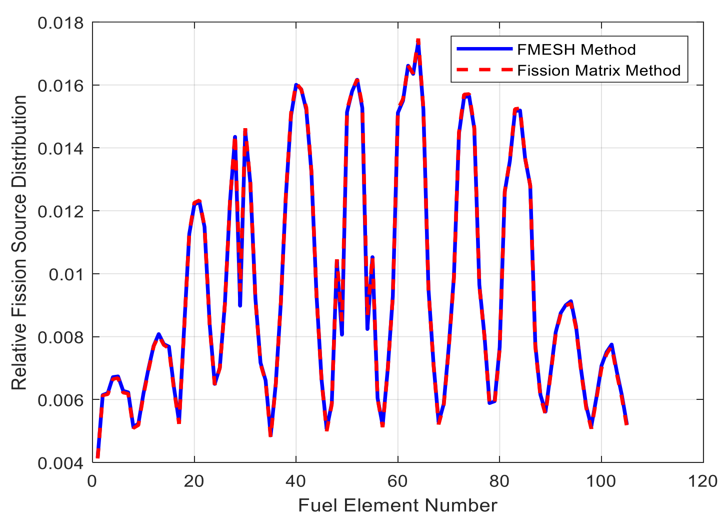

Figure 4-17. Fission source distribution over fuel elements for the FMESH and Fission Matrix Method when control rods are 9.525 cm inserted for core loading 58A

Table 4-9. Comparison of the KCODE-WW calculation versus FMESH and Fission Matrix Method per source particle for core loading 58A when all control rods are inserted 9.525 cm

Detector	KCODE-WW	FMESH Method	Fission Matrix Method	Relative Difference	
	Tally Result	Result	Result	KCODE WW-FMESH	KCODE WW-FM
RSS FC	3.76E-07	3.58E-07	3.59E-07	5.03	4.73
Spare FC	2.07E-07	2.01E-07	2.03E-07	2.98	1.97
CIC	2.39E-05	2.28E-05	2.31E-05	4.82	3.46
GIC	1.83E-07	1.80E-07	1.84E-07	1.67	0.54

*Uncertainties are less than 0.5% for all cases

The fission source distribution between FMESH and Fission Matrix Method is matching well with slight differences according to Figure 4-15, Figure 4-17, and Table 4-8. This proves that both methods are accurate enough to define detector response functions. These preliminary results show that different model calculations matched well with each other. The Fission Matrix Method is used throughout to thesis to check if the FMESH method results are matching with Fission Matrix Method.

4.6.3 Comparison of the KCODE, FMESH, and SSW-SSR method

This section investigates the SSW-SSR method compared with FMESH and KCODE models. The same procedure was followed resembling the previous section as open pool RSS fission chamber results were investigated in Table 4-10.

Table 4-10: Comparison of detector responses calculated using KCODE-WW, SSW-SSR, and FMESH methods at R1 location with all rods out for core loading 59

Detector	KCODE-WW		SSW-SSR Method		FMESH Method	
	Tally Result	Relative Unc.	Tally Result	Relative Unc.	Result	Relative Unc.
RSS FC	3.60E-07	0.0027	3.57E-07	0.0031	3.45E-07	0.0025
Spare FC	2.04E-07	0.0034	2.04E-07	0.0039	1.96E-07	0.0031
CIC	2.34E-05	0.0032	2.33E-05	0.0037	2.27E-05	0.0030
GIC	1.81E-07	0.0052	1.81E-07	0.0134	1.78E-07	0.0049

To summarize, the result and the trend of the detector results match each other for these three methods. The Fission Matrix Method is very fast after running the first iteration for developing the fission matrix. SSW-SSR calculations are also a very effective tool for estimating detector responses. SSR calculations are fast and accurate depending on the SSW output. The problem with this method is that it has very long computational times to acquire accurate SSW results since it can be run only with a single core. This method is not suitable if the source distribution is changing for each calculation, which may happen depending on control rod movements and core location, making the SSW method not suitable for the full detail calculations.

The KCODE-WW and FMESH method are also accurate and can give a detailed understanding of the detector responses. The difference between KCODE and FMESH method is not greatly important since the work done in the thesis mainly focuses on relative changes in various conditions. The total amount of relative changes is between uncertainty limits for these two methods. The main difference comes from the FMESH method that calculates source distribution over the reactor core for reaction rates per volume and then multiplies with the individual detector response function whereas the KCODE calculates direct tally result for the detector. For the rest of the thesis, the FMESH method generated from KCODE calculations and individual fuel element responses will be used.

Chapter 5

Investigation of Reactor Operation Parameters on Detector Responses

Estimating reactor power depends on many parameters. Reactor power is directly related to neutrons reaching to the detector region and interacting with the material inside the detector. Therefore, these parameters include detector calibration, reactor core configuration, and operational features that change the neutron flux around the reactor core.

One major goal of this thesis is to investigate the operation parameters that may change the neutron flux and thus the reactor power. The first parameter is the temperature of the fuel elements. The current MCNP model uses a uniform temperature distribution around the core. In real life, this may not be true and fuel elements should have different temperatures that may need to be investigated. An increase in the fuel temperature may change many parameters which eventually affect the neutron transport.

The second parameter is the control rod positions' effect on the reactor power. The control rods contain neutron absorber material and fuel follower regions (except the transient rod) that change the neutron spectrum drastically. Different control rod positions starting from low power to full power will be investigated by withdrawing control rods together from the core region.

The third parameter is asymmetric control rod insertion. The PSU TRIGA reactor is generally used in Auto control rod mode. This means the control rods move all together to the reach the desired power level. However, in some experiments, asymmetric control rod insertion and withdrawal are tested in the reactor which needs to be investigated for how that affects the neutron flux profile and thus the detector responses.

Since the transient rod does not have a fuel follower region like the other three control rods, asymmetric insertion and removal of the transient rod and the safety rod would change the neutron flux distribution. In addition to that, the closest control rod to the detector region is the transient rod. Thus, asymmetric insertion and removal of this rod would significantly affect the neutron flux distribution around the detector region and therefore the indicated reactor power.

The final parameter that was investigated is the locality of the reactor core. PSBR can be moved between four different operation locations; open pool (R1), near D_2O tank, Fast Neutron Irradiator (FNI), and Fast Flux Tube (FFT). It is known that the proximity to the different structures around the core affects the neutron flux behavior which will give different power readings with the same condition.

All the above-mentioned parameters are investigated and will be described in this chapter. It is important to understand each effect on detector response and reactor power measurement.

Figure 5-1 through Figure 5-7 show the individual fuel element contribution to detector responses, the fission source distribution with FMESH, and a combination of these to create detector response for the RSS fission chamber at 1000 kW. The data is created for five axial regions with more than hundred fuel elements. The visualization in these figures represents the summation of five axial regions for each fuel element. In addition, Figure 5-3 and Figure 5-6 show the axial effect on detector response and fission source.

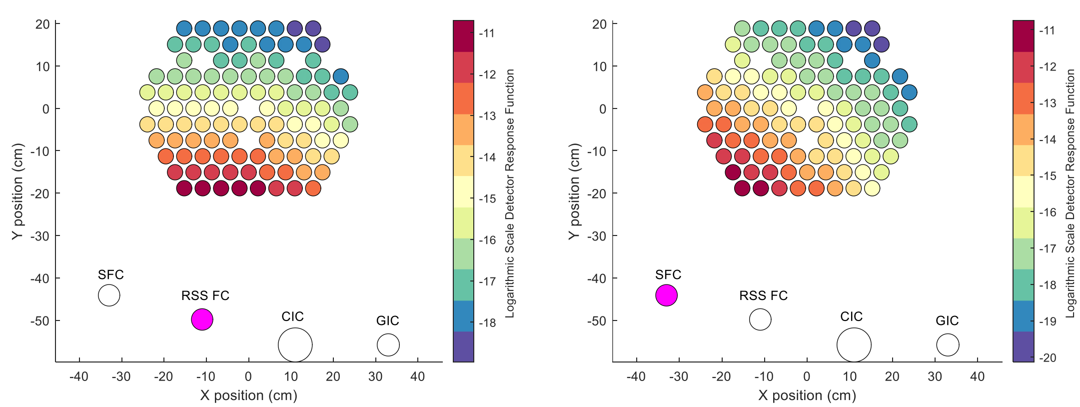

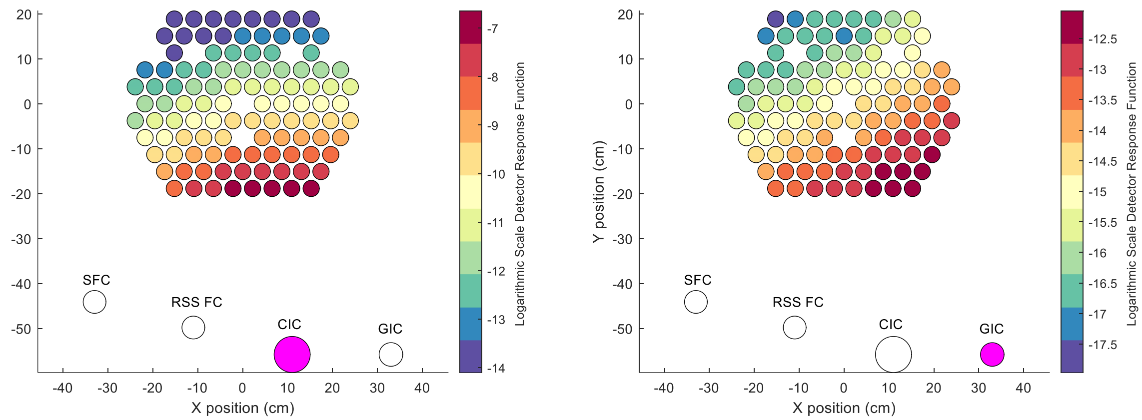

Figure 5-1. Individual fuel element tally contribution to each detector on a logarithmic scale

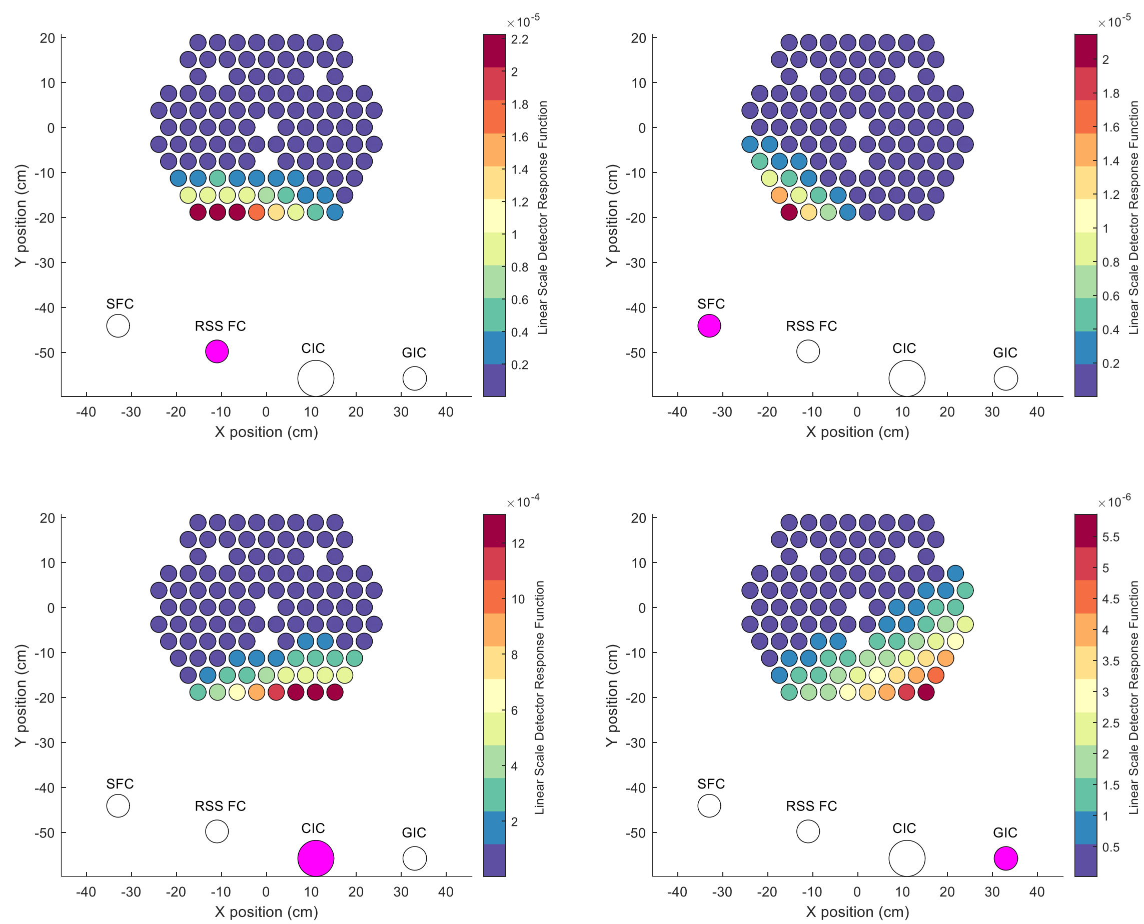

Figure 5-2. Individual fuel element tally contribution to each detector on a linear scale

Figure 5-1 and Figure 5-2 shows the contribution of the individual fuel elements tally results to each detector on a logarithmic and linear scale, respectively. It is expected that the closer fuel elements have a higher contribution to the detector tallies since statistically, moving further away from the detectors, there is less chance of neutrons reaching the detectors. This can be seen in each figure where fuel elements closer to the detectors give higher detector tally results.

The axial effect of detector response functions was also investigated. Figure 5-3 shows the axial fuel element effect on RSS fission chamber tally contribution. Data 1 shows the bottom fuel element and Data 5 shows the top fuel element for each.

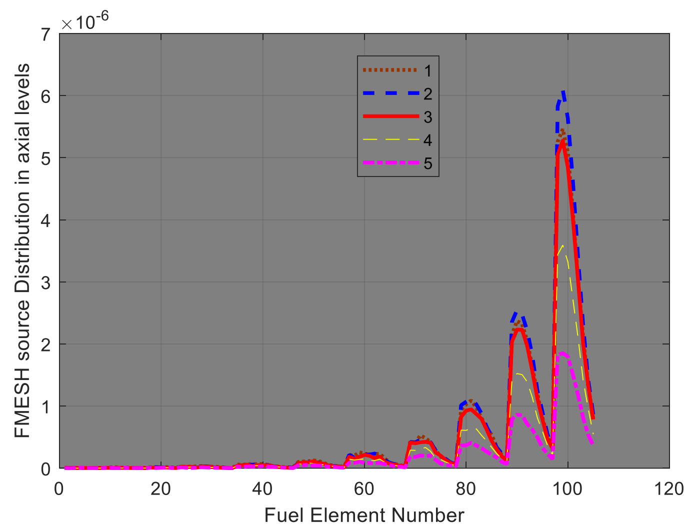

Figure 5-3. Individual fuel element response on RSS fission chamber for each axial location

Figure 5-3 shows the difference of each fuel element in the RSS fission chamber detector response. The second fuel element has the highest tally result. The next highest fuel element contribution comes from the first fuel element from the bottom and the others follow. This can be explained by the axial location and distance of fuel elements to the RSS fission chamber, which is shown in Figure 5-4. Each fuel element is divided up into five axial regions and different colors represent these axial regions inside the fuel element with graphite reflectors located on the top and bottom of the fuel elements.

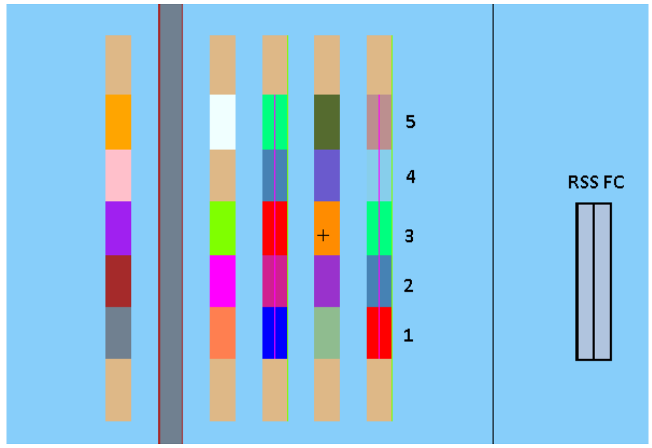

Figure 5-4. RSS Fission chamber axial location versus the fuel elements

Figure 5-4 proves the closest fuel element to the RSS FC is the second fuel element from the bottom. This matches with the detector tally results provided in Figure 5-3, where the second fuel element from the bottom has the highest tally result. After that, the first and third fuel elements have the maximum tally results, which are the second-closest fuel elements to the RSS Fission chamber.

Similar to this, the axial effect for the FMESH fission source was also investigated. Figure 5-5 shows the FMESH fission source change per fuel element for each axial location in the fuel.

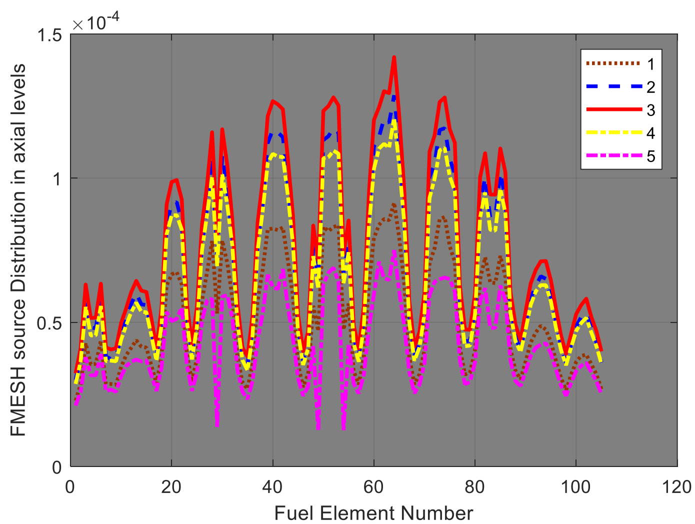

Figure 5-5. FMESH fission source change per fuel element for each axial location

According to Figure 5-5, the highest fission source occurs in central fuel elements for each fuel. This is followed by the second and fourth fuel elements, and then the first and fifth fuel elements. These results were expected since the highest fission rate occurs at the center of the reactor core. Axial location five and four have less fission source compared to axial location one and two, respectively. This can be explained by the axial neutron flux change due to control rod insertion. Since control rods are inserted from the top of the reactor core, the top fuel elements have less fission source.

The combination of the axial FMESH fission source is also investigated with 2D plots. Figure 5-6 shows the fission source distribution for the 1000 kW case when the reactor operates at the R1 open pool location.

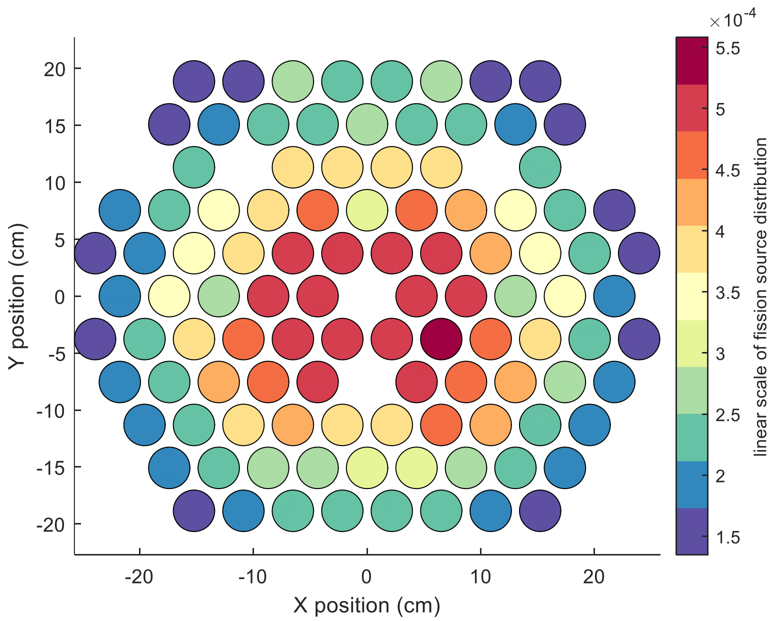

Figure 5-6. Fission source distribution with FMESH method at open pool location with 1000 kW

Figure 5-6 shows the fission source distribution with the FMESH method for 1000 kW power. The fission source is higher in the center of the core which is expected since higher fission density at the center of the reactor core. Figure 5-7 represents the FMESH detector response for all ex-core detectors for both linear and logarithmic scales.

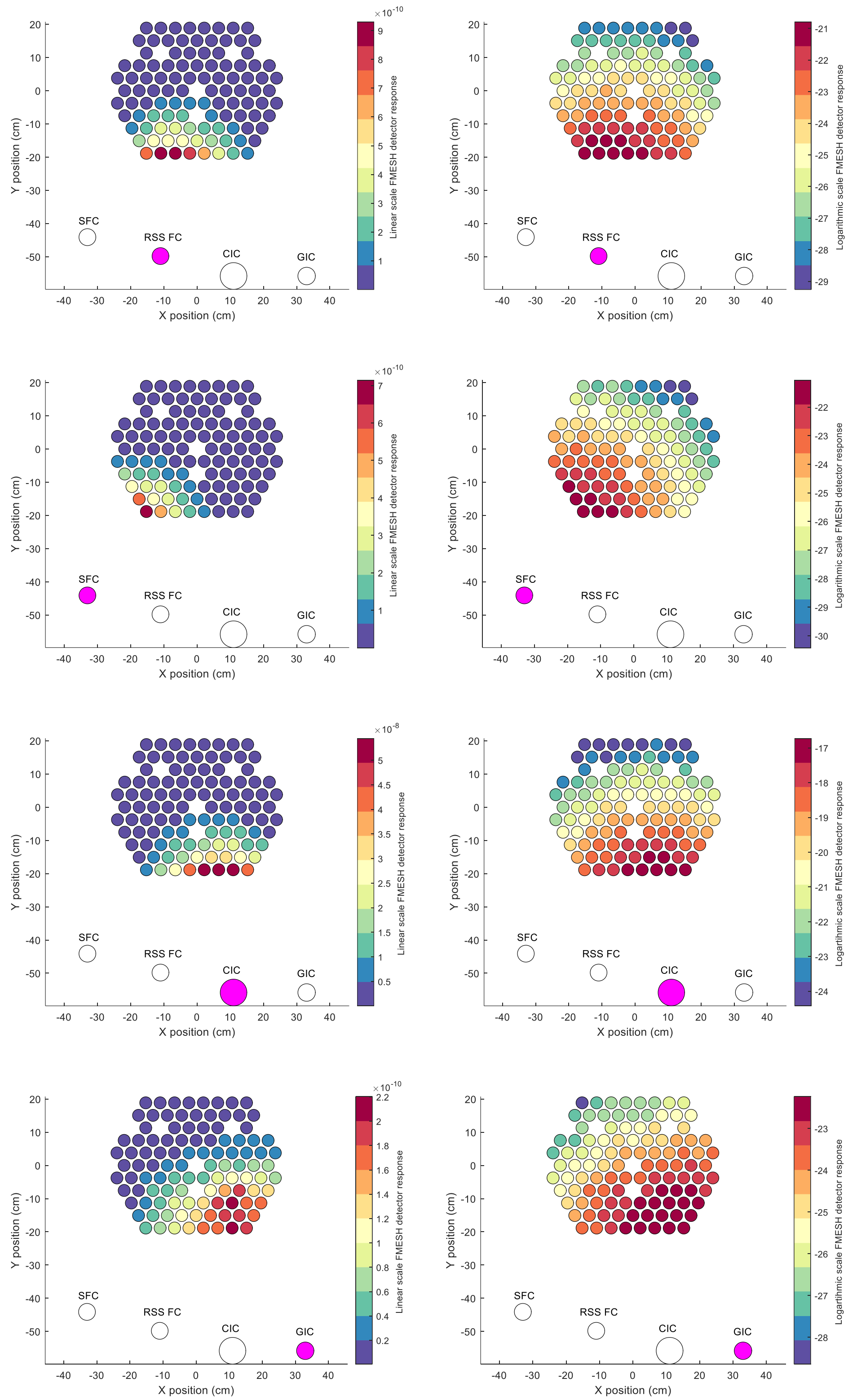

Figure 5-7. FMESH detector response model for the RSS fission chamber for both linear and logarithmic scale

Figure 5-7 shows the combination of the detector response created by the FMESH method that takes into account fission source and individual fuel element contribution. The importance of individual fuel element contribution arises in the result and difference for the detectors observed.

5.1 Fuel Temperature Effect on Detector Response

In this section, the fuel temperature effect on the detector response is investigated. In MCNP, individual fuel element material temperatures changed with two different temperatures: 300 Kelvin and 600 Kelvin. In addition to that, S (α, β) and tmp0 card data also changed for 300 K and 600 K. KCODE runs are done for two different temperatures with the same control rod position of all rods inserted at the open pool location. The temperature of the detector regions was kept constant at 300 K. Figure 5-8 through Figure 5-12 show the results for two different temperature levels of the fission chambers, compensated ion chamber, a gamma ion chamber, and a self-powered neutron detector.

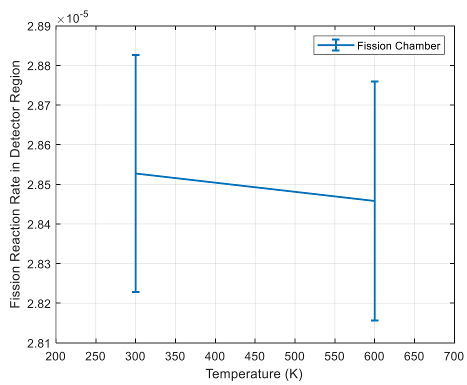

Figure 5-8. Fission Chamber fission reaction rate change with temperature

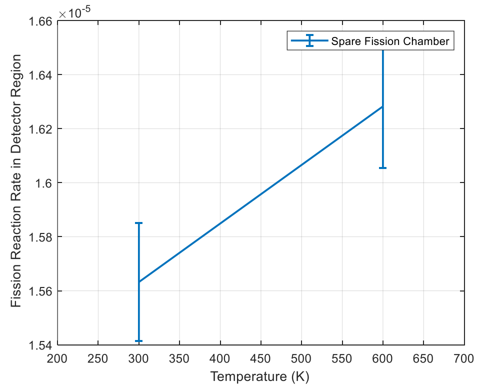

Figure 5-9. Spare Fission Chamber fission reaction rate change with temperature

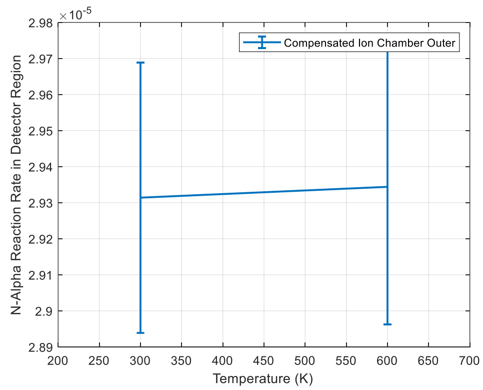

Figure 5-10. Compensated Ion Chamber Outer region n-alpha reaction rate change with temperature

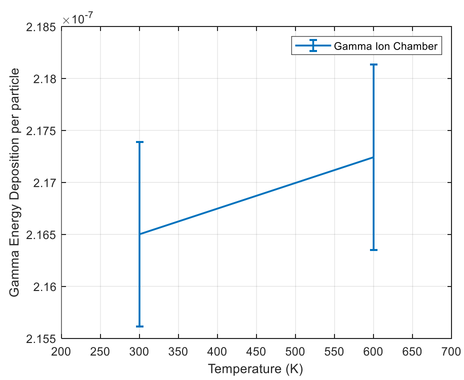

Figure 5-11. Gamma Ion Chamber gamma energy deposition per particle change with temperature

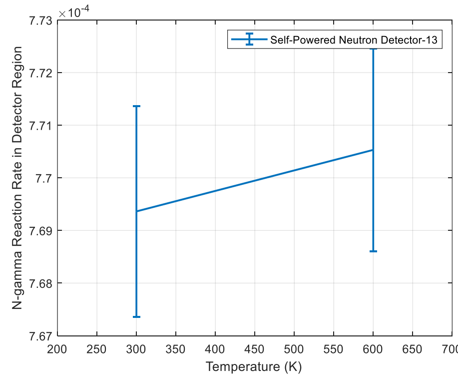

Figure 5-12. Self-powered neutron detector-13 which is placed in the central thimble, n-gamma reaction rate change with temperature

Table 5-1 shows the detector tally results with varying fuel temperature of 300 K and 600 K and percent changes between the two with the uncertainties.

Table 5-1. Detector tally results with varying fuel temperature of 300 K and 600 K

Detector	Tally Result at 300 K	Tally Result at 600 K	Percent Change (%)	Uncertainty(%)
RSS FC	2.853E-5	2.846E-5	0.25	1.10
Spare FC	1.565E-5	1.627E-5	-3.81	1.28
CIC	2.932E-5	2.934E-5	-0.07	1.27
GIC	2.165E-7	2.173E-7	-0.37	0.36

The results from Figure 5-8 through Figure 5-12 and Table 5-1showed that there is less than a 0.3% difference between the two temperature levels with KCODE calculations for most cases and less than 4% for the spare fission chamber. This work also assumed a uniform temperature distribution, which is not generally true; the center of the core will be at a higher temperature than the periphery. This non-uniform temperature will cause a power shift away from the hot center of the core toward the outside. Rau, A., and Walters, W.J. describe this in their paper [4] and it will be investigated in the next section.

5.1.1 Non-Uniform Fuel Element Temperature Distribution Effect on Detector Response

For the non-uniform fuel element temperature effect on detector responses, the Fission Matrix Method has been used. It has been proved before that the Fission Matrix Method can produce identical results to the FMESH method with a faster computational time.

For temperature analysis, power levels of 100, 250, 500, 750, and 1000 kW were simulated to calculate power distributions using Fission Matrix Method. Then, temperatures are derived from the different power levels using Sahin's fuel temperature correlation which is shown in Equation 5-1 [43].

$$T_S = f\left(\frac{P_S}{P_{I-17}} P_{Reactor}/10^3\right) \qquad \text{Equation 5-1}$$

and f is given for

$$f = \begin{cases} 294.07 + 1293.13x - 1933.8x^2 + 1391.94x^3 & P_{Reactor} \leq 400\ kW \\ 749.23x^{0.34} - 10 & P_{Reactor} \geq 400\ kW \end{cases}$$

where $P_{Reactor}$ is the reactor power in kW and T_S is in Kelvin, P_S is local power and P_{I-17} is the power in the I-17 fuel element location, usually referred to as maximum power.

The calculations were repeated using a variable temperature derived from the Equation 5-1. Figure 5-13 shows the fission source distribution using uniform and variable fuel temperature and relative differences between the two at full power near the R1 open pool.

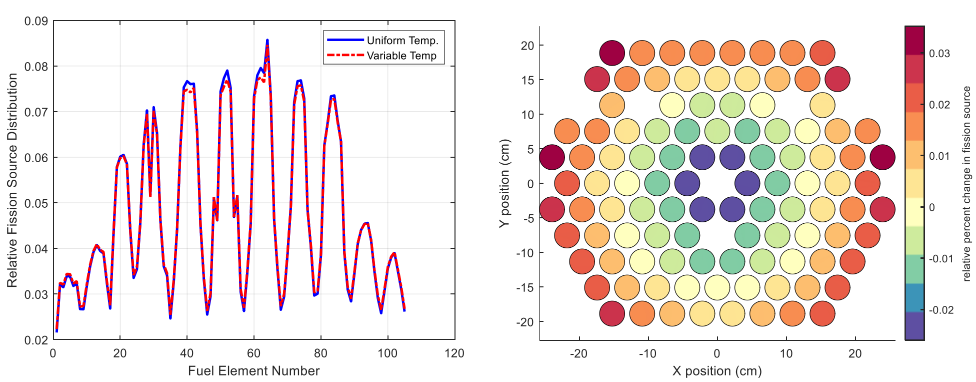

Figure 5-13. Fission source distribution using uniform and variable fuel temperature and relative differences between two at full power near the R1 open pool.

The results show that there is a slight change in the fission source distributions for the uniform and variable temperatures. The main relative difference happens at the fuel elements closer to the center where the highest difference is around 3 %. On the periphery, variable temperature has higher results, as much as 3%. These results matched with Rau's description about modeling the fuel temperature profile instead of an average uniform fuel temperature was found to alter the 3D fission source distribution by up to 5% [4]. Table 5-2 shows the Fission Matrix method calculation for the RSS fission chamber detector response using variable and uniform temperatures for the fuel elements.

Table 5-2. Fission Matrix Method RSS fission chamber detector response for several power levels at the R1 open pool

	1 W	100 kW	250 kW	500 kW	750 kW	1000 kW
Variable Temperature	3.612E-07	3.577E-07	3.578E-07	3.555E-07	3.538E-07	3.516E-07
Uniform Temperature	3.612E-07	3.572E-07	3.567E-07	3.539E-07	3.519E-07	3.498E-07
Relative Change (%)	2.73e-3	0.14	0.31	0.45	0.54	0.51

According to Table 5-2, there is a -0.52% change between using uniform and variable temperatures at full power. The change due to uniform versus variable temperature of the fuel elements drops significantly in low powers. This low change in detector response is due to fuel elements that are closer to the detectors having a higher contribution to the detector response and because they are not affected by variable and uniform fuel element temperature distributions according to Figure 5-13. Due to this reason, the non-uniform fuel temperature effect can be neglected for future runs, and uniform fuel temperature will be used.

5.2 Control Rod Position Effect on Detector Responses

After all the ex-core detectors and the reactor core are modeled in MCNP, preliminary runs were completed using the KCODE method in Chapter 4. These preliminary calculations showed that control rod movement changes the tally results due to a change in neutron flux profile. In this section, a detailed investigation will be done on the control rod position effect on detector responses when the reactor is placed at R1 open pool. Figure 5-14 shows fuel and control rods positions at the center of the reactor core with associated power levels that are taken from operational data on 4/15/22. The grey color represents the graphite reflectors on the top and bottom of the fuel elements and under the control rods. The red color represents the neutron absorber material inside the control rod. Each fuel element is divided into five axial regions and other colors represent these axial regions inside the fuel element.

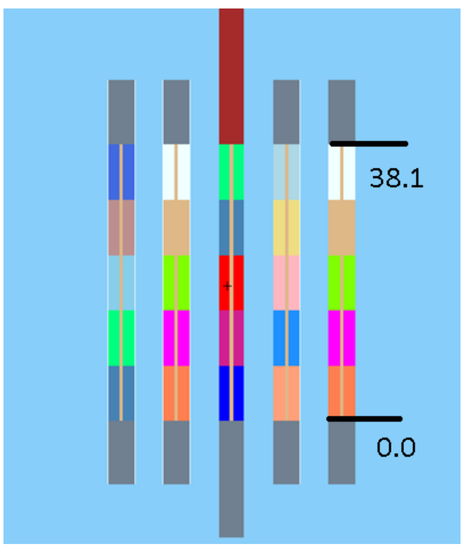

Reactor Power	R1 open pool position (cm)	D_2O tank position (cm)
All rods in	0.00	0.00
1W	23.27	21.41
100 kW	24.51	22.58
250 kW	26.19	24.16
500 kW	28.55	26.21
750 kW	30.78	28.14
1000 kW	33.12	29.95
All rods out	38.10	38.10

Figure 5-14. Control rod position comparing to fuel elements and reactor power for R1 and D_2O tank associated to the control rod withdrawal from the 0 cm rod position

According to the MCNP model, in theory, control rods can be removed from the core by about 38.1 cm which is equal to 15 inches. Control rods can be removed 15 inches individually but not evenly because it will exceed reactor power limitations. 38.1 cm withdrawal for single and double control rods will be investigated in the asymmetric rod insertion and experiment sections. The focus of this section is even control rod movement and how power is affected by it.

After the startup of the reactor, the control rods were withdrawn from the core slowly to reach criticality conditions. To achieve the same power level for R1 and D_2O tank locations, different control rod withdrawals are required since neutron flux shapes are different for these two locations due to tilting caused by the D_2O tank which results in a change in neutron moderation near the core and thus the power. The D_2O tank control rod positions are 2-3 cm less than R1 open pool locations which proves with the same control rod positions, the D_2O tank would have higher reactor power reading with the current detector configuration. The locality effect will be investigated in the upcoming section for the R1, D_2O tank, FNI, and FFT.

Similar to the preliminary runs, this section focuses on control rod position change, and an investigation is performed for ex-core detectors using the FMESH method. For the simulations, operational data was received from the reactor console. These operational data include calibrated reactor powers for each detector, control rod positions, and fuel temperature at each power. Since the control rod position data depends on the calibrated power at the reactor, proper normalization needs to be done for the simulation results.

Simulations were performed for various control rod positions at R1 open pool location. These rod positions are 23.27, 24.51, 26.19, 28.55, 30.78, and 33.10 cm withdrawal from the zero control rod position, and represent power levels of 0.001, 100, 250, 500, 750, and 1000 kW which was shown in Figure 5-14. In addition to that, 38.1 cm withdrawal is also included in the calculations which correspond to the hypothetical all-rods-out case. Figure 5-15 represents the RSS Fission chamber reaction rate per source particle change with all control rods evenly withdrawn from the reactor core. Data points represent the power levels described above and all-rods out case.

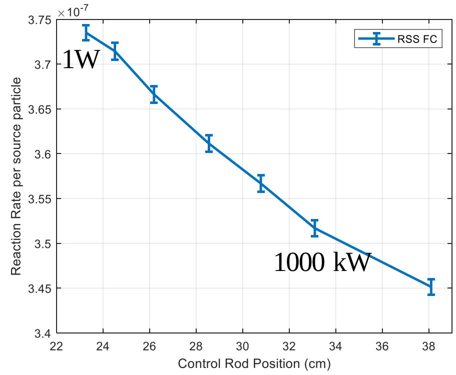

Figure 5-15. RSS Fission chamber reaction rate per source particle change with control rod withdrawal from the reactor core

Figure 5-15 shows that the reaction rate in the fission chamber per source particle has an overall decreasing trend. This phenomenon is explained in Section 4.2. As the control rods are inserted from the top, the axial flux distribution will shift its peak toward the lower core. Since the detectors are located close to the lower section of the reactor core, in low powers, more source particles are available in the detector region compared to the high powers. Low uncertainties result in insignificant variation of results. All control rods use the same detector response function, and in the FMESH method, the highest uncertainty contribution comes from the detector response function. For this reason, uncertainties do not vary. Figure 5-16 represents the reaction rate per source particle change with the control rod removal from the core for the spare fission chamber.

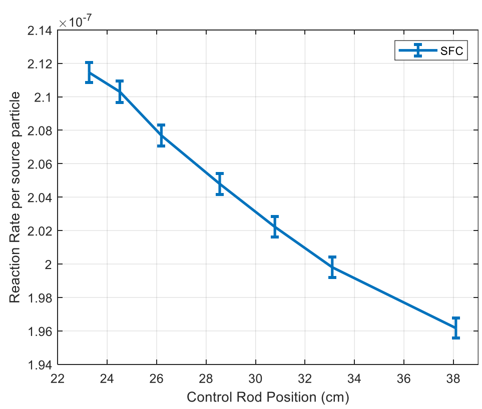

Figure 5-16. Spare Fission chamber reaction rate per source particle change with control rod withdrawal from the reactor core

The spare fission chamber has a similar trend to the RSS fission chamber with the control rod position change. The total change between 1 W and 1000 kW is less in the spare fission chamber compared to the RSS fission chamber. This can be explained by the locality of these detectors in relation to the reactor core. The RSS fission chamber is the closest detector that faces the reactor core which is more affected by any change in the reactor core. The spare fission chamber is located on the edge and further away from the reactor core. According to the simulation results in Figure 5-16, the spare fission chamber is less affected by the control rod position change compared to the RSS fission chamber.

Figure 5-17 shows the compensated ion chamber (CIC) reaction rate per source particle change with control rod withdrawal from the reactor core.

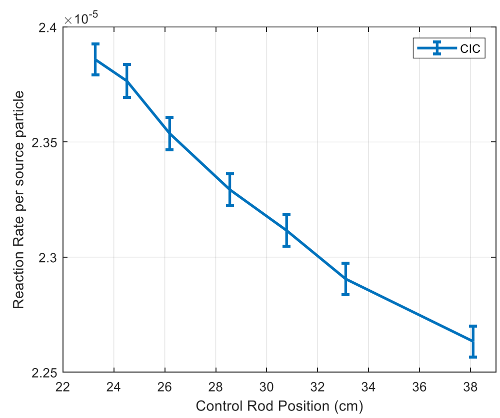

Figure 5-17. Compensated ion chamber reaction rate per source particle change with control rod withdrawal from the reactor core

The CIC, which is another detector that is close to the reactor central axis, follows a similar trend to the RSS fission chamber. The reaction rate per source particle change between 1 W and 1000 kW in the CIC is not as significant as the RSS fission chamber. The RSS fission chamber has about 23 cm long active region whereas the CIC has a 35 cm-long active region. This height difference also affects the detector responses since the CIC can capture more information due to control rod position change, thus giving less change in reaction rate per source particle.

Finally, Figure 5-18 represents the reaction rate per source particle change with control rod withdrawal from the core for the gamma ion chamber.

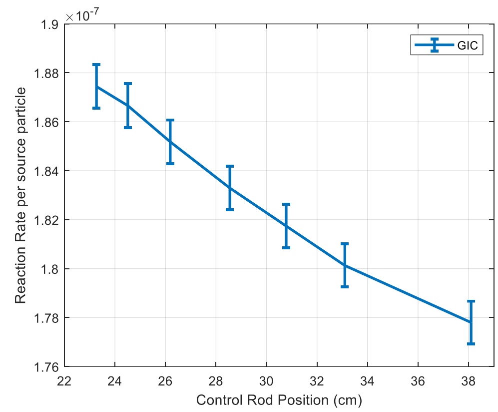

Figure 5-18. Gamma ion chamber reaction rate per source particle with control rod withdrawal from the reactor core

The trend in Figure 5-18 is similar to the trend in Figure 5-17 for the CIC. Since these detectors share the same locality, it is expected to see similar trends for all detectors with minor differences that may be caused by different parameters. The FMESH uncertainties of these detectors are between 0.2 % and 0.5 %, which is very small. Table 5-3 shows the percent change of FMESH results for each detector from 1 W to 1000 kW.

Table 5-3. Percent change of FMESH results for each detector from 1 W to 1000 kW at R1 open pool

	Percent Change (%)
RSS FC	6.20
SFC	5.82
CIC	4.16
GIC	4.06

According to Table 5-3, the highest change in FMESH results was observed in the RSS fission chamber. The lowest change was observed in the gamma ion chamber. The main reason for this difference comes from individual detector response functions being varied for each detector.

These results do not represent the reactor power directly. As mentioned previously, proper normalization is required to compare these results in terms of power. For example, RSS fission chamber results are multiplied with calibrated reactor power levels and, Figure 5-19 shows the results for power adjusted tally results from the MCNP and the linear trend line of this result.

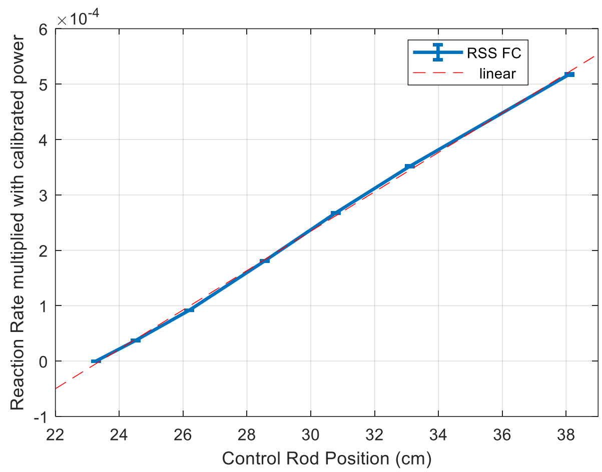

Figure 5-19. Reaction rate results multiplied with corresponding calibrated power values for RSS fission chamber

Figure 5-19 exemplifies the multiplication of the calibrated power with reaction rate results per source particle. A near linear response is achieved with the simulation results that use the data taken from the reactor console. Estimating the true reactor power will use a similar approach and this will be explained in the future sections.

Figure 5-15 through Figure 5-19 shows the combined FMESH result for each power level and compares them. Changing the control rod position affects the flux distribution around the core. To investigate this behavior, an MATLAB code was developed to visualize and compare five axial fuel regions for the calculations.

The FMESH method is applied to the different control rod results and relative differences investigated. Figure 5-20 shows the relative difference between the FMESH fission sources where the reactor powers are at 1000 kW and 1 W.

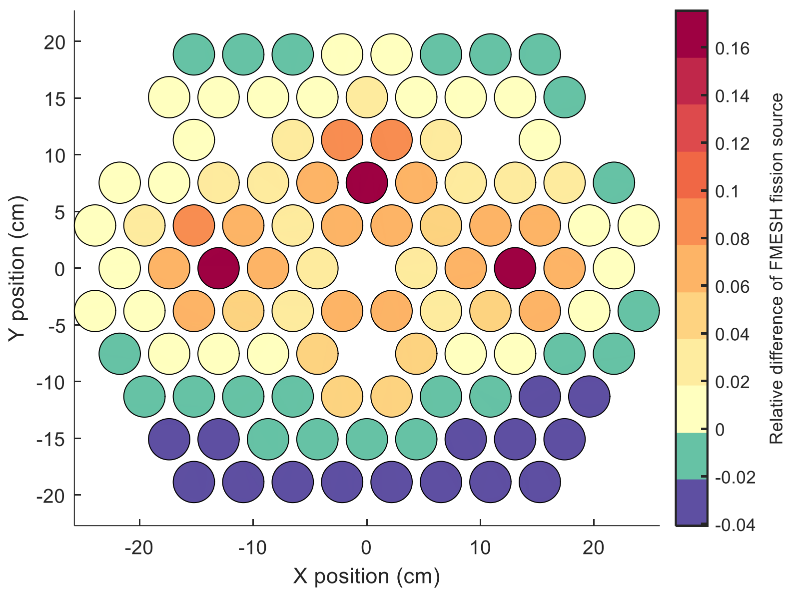

Figure 5-20. FMESH relative change on fission source at 1000 kW and 1 W

Since the control rods are inserted more in 1 W power level, flux is tilted to core edges. For this reason, the 1 W power level has a higher contribution on the north side of the reactor core. 1000 kW power level has a higher contribution where control rods are placed. Since safety, regulating, and shim rods have fuel follower rods, removing them from the core introduces a fuel element to the system, causing more fission in that region. Since the control rod was replaced by the fuel element, these regions have higher FMESH fission source results compared to the 1 W power level. The effect of not having fuel followers in the transient rod is also observed in this figure. The asymmetry can be easily seen due to this effect.

This section proves the importance of the control rod movement on detector response functions and fission sources. The results are shown for only the R1 open pool location for this section and other core localities will be investigated and compared in Section 5.4. Later, the fission sources created by the FMESH method will be used to estimate detector responses in various conditions.

5.3 Asymmetric Control Rod Effect on the Detector Response

The PSBR has four control rods and one of these control rods have different characteristics than the other control rods. The safety, shim, and regulating rods have a neutron absorber B_4C on top and a fuel follower region on the bottom section. When control rods were withdrawn from the reactor core, neutron absorber material is eliminated and the fuel element was placed in its location. On the contrary, the transient rod has air in the bottom section, so removing the transient rod introduces air to the reactor core rather than introducing additional fuel. PSBR can be pulsed up to 2000 MW in a very short amount of time, approximately 30-40 milliseconds. This is done by applying air pressure to the transient rod and removing it from the reactor core.

In the present reactor operation, the rods are usually placed at the same level using automatic control rod control, but in the past, they have generally been used unevenly. In one-rod automatic power control, the regulating rod is removed to reach the desired power level. If the regulating rod is not enough to reach the desired power level, the shim rod was withdrawn from the reactor core to reach the desired power level [44].

The individual movement of the control rods may cause flux tilting across the core and will be investigated in this section. It is expected that this flux change would affect the power calibration process. In practice, PSBR asymmetric insertion and removal is not used at full power, but it can be done at 500 kW. In this part, KCODE simulations are done with ADVANTG code for different control rod positions for asymmetric insertion. FMESH tally results are obtained from these KCODE calculations and detector responses are calculated by multiplying FMESH results with individual tally responses for the R1 open pool location.

First, all the control rods were moved to the 500 kW position for each location. The criticality constant k_{eff} is calculated by MCNP is 1.00092. Second, the transient rod was inserted two inches and the safety rod was withdrawn two inches, with the $k_{eff} = 1.00245$ value observed. Finally, the transient rod was withdrawn two inches, and the safety rod was inserted two inches with the $k_{eff} = 1.00158$. Detector tally responses are plotted in Figure 5-21 through Figure 5-26 which show the effect of asymmetric control rod movement.

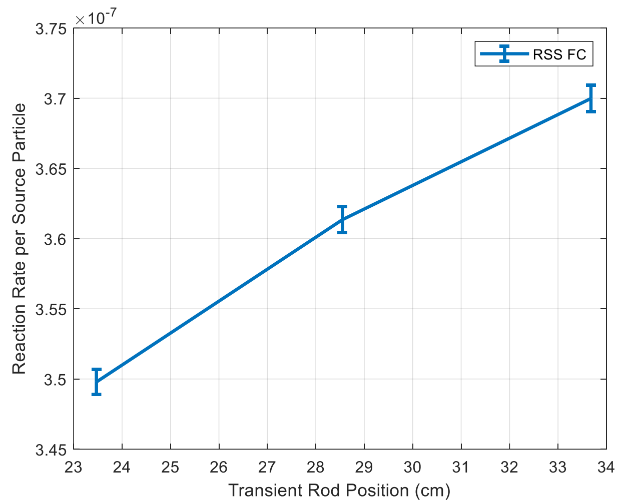

Figure 5-21. Asymmetric control rod effect on RSS fission chamber with changing transient and safety rod position for the R1 open pool position

Results from Figure 5-21 indicated that asymmetric control rod insertion and removal have a significant effect on detector results, about 5.8% for RSS FC. The reaction rate is less in the RSS fission chamber when the transient rod is inserted and the safety rod is removed. It is high when the transient rod is removed and the safety rod is inserted. This can be explained by the close proximity of the RSS fission chamber in relation to the transient rod, while the safety rod is further from the detector region. When the transient rod is inserted and the safety rod is removed, the flux profile shifts away from the detector region, thus less reaction rate happens in this area. The reactor console reads the same power at this detector region but these calculations prove actual power is different for these asymmetrical insertion levels. Figure 5-22 shows the relative change in the FMESH fission source when the transient rod is inserted and withdrawn. First, the transient rod is removed from the reactor core by two inches and the safety rod is inserted into the reactor core by two inches while keeping the shim and regulating rod at the same position. Finally, the transient rod is inserted into the reactor core by two inches and the safety rod is removed from the reactor by two inches. FMESH results for each fuel element were recorded for both cases and the relative difference between them was calculated and shown.

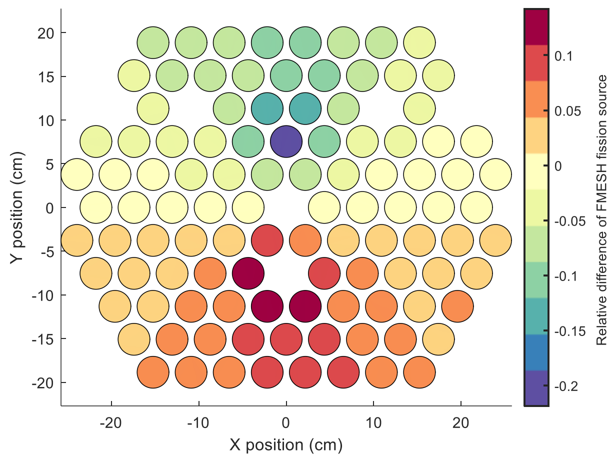

Figure 5-22. Relative change of FMESH fission source for the RSS fission chamber where transient rod removed and safety rod inserted versus transient rod inserted and safety rod is removed

Figure 5-22 proves that when the transient rod is removed and the safety rod is inserted, neutron flux distribution is tilted towards the detector region. This means, the control console will read the same amount of power for both cases but, when the safety rod is removed, the actual reactor power will be higher due to the reactor power shift away from the detector region.

Similar to the RSS fission chamber, the spare fission chamber, compensated ion chamber, and the gamma ion chamber is also investigated in Figure 5-23, Figure 5-24, and Figure 5-25.

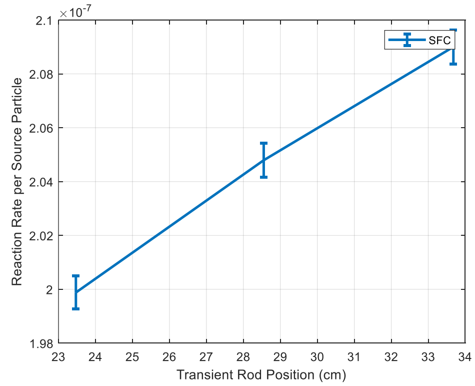

Figure 5-23. Asymmetric control rod effect on spare fission chamber with changing transient and safety rod position

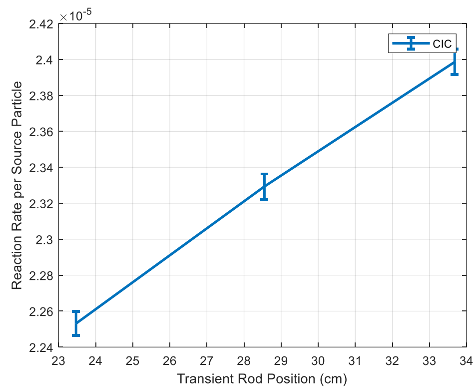

Figure 5-24. Asymmetric control rod effect on compensated ion chamber with changing transient and safety rod position

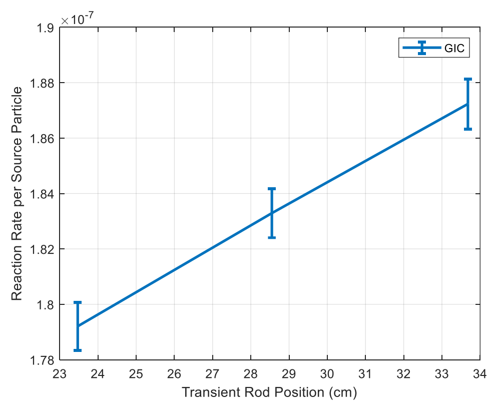

Figure 5-25. Asymmetric control rod effect on gamma ion chamber with changing transient and safety rod position

The effect of the asymmetric control rod insertion can be seen in Figure 5-21 through Figure 5-25. Withdrawal of the transient rod causes an increase in the reaction rates at the detector region due to the shift caused by the control rod effect.

All the ex-core detectors are affected by this asymmetrical insertion by the transient and safety rod. Since there is no detector located on the south side of the core, hypothetical SPND designs are implemented into the MCNP model at the south and north face of the reactor core. Figure 5-26 shows the change in the reaction rates close to the transient rod region and safety rod region using core loading 58A. SPNDs were created with five axial regions to show the importance of the control rod effect in an axial direction.

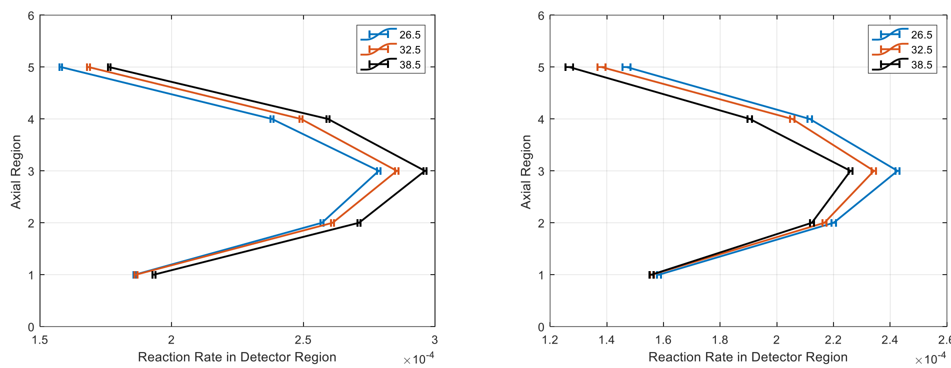

Figure 5-26. SPND 6 and SPND 12, where SPND 6 is close to the transient rod and SPND 12 is close to the safety rod

Figure 3-10 shows the location of the SPNDs compared to the core. SPND 6, which is closer to the detector region and the transient rod, has a greater reaction rate when the transient rod is withdrawn from the reactor core. SPND 12 has the opposite results since it is closer to the safety rod region. These figures also show the difference in axial fuel elements. The bottom fuel elements are less affected by asymmetrical insertion and withdrawal compared to the top fuel elements.

Table 5-4 shows the change in tally results on detectors when transient and safety rods were inserted and removed asymmetrically. The power levels for each asymmetry are calculated by taking a reference power of 500 kW with even control rods.

Table 5-4. Tally result (per source particle) of the detectors with two inches' insertion and withdrawal of the transient and safety rod, asymmetrically

Detector	Transient Rod Out-Safety Rod in	Even Rods	Safety Rod Out-Transient Rod in	TR Out-SF In Power	SF Out-TR In Power
RSS FC	3.6998e-07	3.6135e-07	3.4978e-07	488.34	516.54
SFC	2.0900e-07	2.0479e-07	1.9988e-07	489.92	512.28
CIC	2.3986e-05	2.3293e-05	2.2531e-05	485.55	516.91
GIC	1.8723e-07	1.8329e-07	1.7921e-07	489.48	511.41

*Uncertainties are less than 0.7% for all cases

The figures in this section and Table 5-4 prove that asymmetrical insertion and withdrawal of the transient and safety rods have a significant effect on detector responses. Because the transient and safety rods are closer and further to the detectors respectively, they have significant effects on detector response during asymmetrical movement conditions. Table 5-4 also shows the power correction if even rod position is assumed at 500 kW reactor power, and the other two cases show different power levels according to the tally results. The highest simulated reactor power was 516.91 kW and the lowest simulated reactor power was 485.55 kW.

The next investigation in this section is done with asymmetrical insertion and withdrawal of the shim and regulating rod. A similar approach was followed as two inches' withdrawal and insertion established asymmetrical conditions for these control rods. The other two control rod positions were held constant. Figure 5-27 shows the effect of asymmetrical insertion and withdrawal of shim and regulating rod over fission source.

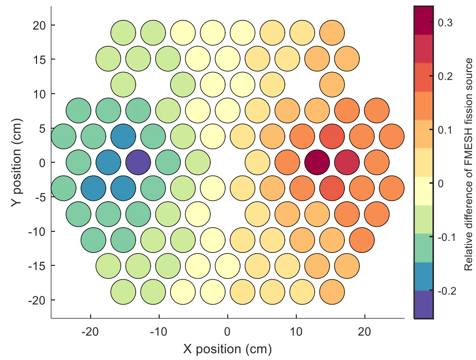

Figure 5-27. Relative change of FMESH with asymmetrical insertion of the shim and regulating rod

Figure 5-27 proves the FMESH results change with the asymmetrical insertion and withdrawal of the shim and regulating rod. In this figure, the regulating rod is withdrawn and the shim rod inserted first. Next, the regulating rod is inserted and the shim rod is withdrawn. In the first case, the fission source shift towards to east side of the reactor core. This asymmetrical configuration is important since it will affect the detector located at the edge. Because the gamma ion chamber is located at the east corner and the spare fission chamber is located at the west corner, these two detectors should have opposite FMESH results.

Table 5-5 shows the change in tally results over the detectors when the shim and the regulating rod were asymmetrically inserted and withdrawn from the reactor core. Reactor powers are calculated by the assumption that even rod position is assumed as 500 kW.

Table 5-5. Tally result (per source particle) of the detectors with two inches' insertion and withdrawal of the shim and the regulating rod, asymmetrically

Detector	Regulating Rod Out-Shim Rod in	Even Rods	Shim Rod Out-Regulating Rod in	REG Out-SH In Power	SH Out-REG In Power
RSS FC	3.5548e-07	3.6135e-07	3.6480e-07	508.25	495.27
SFC	1.9705e-07	2.0479e-07	2.1061e-07	519.64	486.18
CIC	2.3556e-05	2.3293e-05	2.2999e-05	494.42	506.39
GIC	1.8705e-07	1.8329e-07	1.7898e-07	489.94	512.04

*Uncertainties are less than 0.7% for all cases

Figure 5-27 and Table 5-5 prove the significant effect of the insertion and removal of the shim and regulating rod asymmetrically. The CIC was not affected significantly by this insertion since the location of the CIC is close to the center of the core. RSS FC is affected more than CIC, and it may be explained by distance to the reactor core since RSS FC is closer to the reactor face, thus affected more by the control rod insertion and withdrawal. Finally, the highest effect was observed in the spare fission chamber and then the gamma ion chamber. These two detectors are located at the edge of the core periphery and are affected more by the shim and the regulating rod asymmetrical movement. The highest simulated reactor power was 519.64 kW and the lowest simulated reactor power was 486.18 kW.

These results proved that asymmetric control rod movements affect detector responses and a power correction for power measurements is required for the individual control rod movements. Asymmetric control rod insertion and removal are also investigated in the next section for various core locations such as asymmetrical investigation of the RSS fission chamber for R1 open pool, D_2O tank, FNI, and FFT.

5.4 Reactor Core Location Effect on Detector Responses

When the neutron collides with a smaller atom like hydrogen, it can slow down and lose its energy. Water (H_2O) is an excellent moderator since it contains hydrogen, which slows down the fast neutrons. Water slows down neutrons more quickly, but absorbs more neutrons, while heavy water (D_2O) slows down neutrons more slowly but doesn't absorb as many [45]. Table 5-6 shows the slowing down parameters for the water and heavy water.

Table 5-6. Slowing down parameters for water and heavy water moderators [46]

Moderator	ξ	$\xi\Sigma_s(cm^{-1})$	$\frac{\xi\Sigma_s}{\Sigma_a}$
H_2O	0.920	1.350	71
D_2O	0.509	0.176	5670

ξ represents mean lethargy gain per collision, $\xi\Sigma_s$ is the moderating power and $\frac{\xi\Sigma_s}{\Sigma_a}$ is the moderating ratio. Moderating power shows how effective the moderator is at scattering the incident particles. Moderating power does not alone show the effectiveness of the moderator since absorption is another factor that needs to be considered. It is taken into account in the moderation ratio. The moderating power of hydrogen is higher compared to heavy water. However, heavy water is a better moderator because of the less absorption cross-section for neutrons, thus having a more moderation ratio. For this reason, having a D_2O tank near the reactor core causes more fission near the periphery thus shifting the neutron flux profile away from the detector region. For this reason, the calibration procedure takes place near the D_2O tank to ensure the power reading is maximum. According to Bascom [10], with the instrumentation calibrated at the previous D_2O tank arrangement, the actual thermal power in the R1 open pool position was 960 kW when the reactor console measured 1 MW.

This section will investigate the core locality effect on operational parameters such as control rod position change and asymmetrical rod insertions.

5.4.1 Core Locality Effect on Detector Responses

The next goal is a detailed investigation of the proximity of the reactor core to the FNI, FFT, D_2O, and R1 open pool location. Since the structures around the reactor core may affect neutron distribution inside and outside of the core due to moderation and reflection, it would affect detector response as well. Preliminary runs are completed with the D_2O tank and open pool locations and results were compared for the detectors. The detector response (and thus indicated power) was approximately 4% lower when measured at the D_2O tank compared to the open pool using the same control rod position for both cases.

To investigate this power inaccuracy, the reactor core, components, and detectors were modeled into R1, D_2O tank, FNI, and FFT which can be seen in Figure 3-11 through Figure 3-14.

Similar to the previous section, control rod positions are changed to positions corresponding to 0.001, 100, 250, 500, 750, and 1000 kW. First, fission source distribution changes due to the locality effect were investigated. Figure 5-28 shows the relative fission source change between the D_2O tank versus the FNI, FFT, and R1 open pool location at reactor power simulated at 1000 kW.

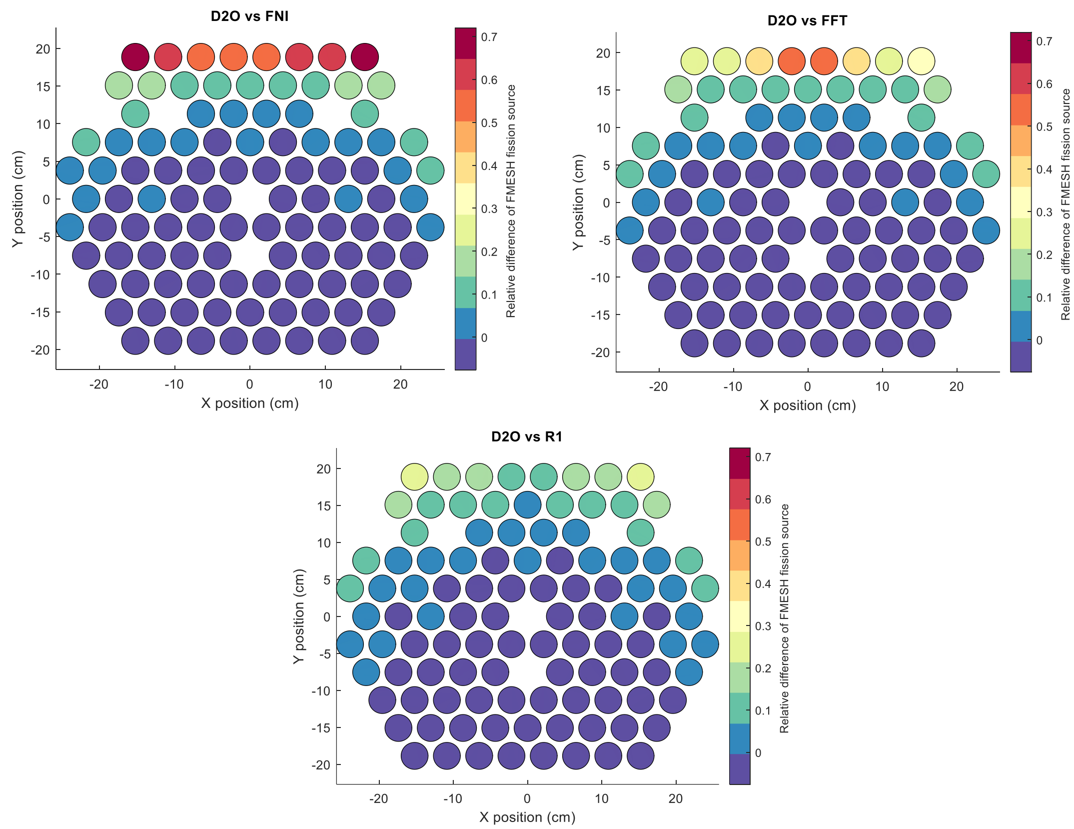

Figure 5-28. Relative fission source change for D_2O versus FNI, FFT, and R1, respectively

Figure 5-28 proves the importance of the core locality over the fission source distribution. In R1 open pool location operation, there is no structural material around the reactor core. In the D_2O tank location, the core is surrounded by the D_2O tank, which shifts the fission source to the D_2O tank due to better moderation. The FNI and FFT contain lead and borated aluminum structures. When the reactor is operated at FNI and FFT, these structures take over the place of pool water. Therefore, moderation by the pool water will be lost. In addition to that, higher thermal neutron absorption will occur in the borated aluminum. All of these factors will result in a decrease in fission source at the periphery of the reactor core that is near the FNI and FFT fixtures. An approximate 70% decrease in FNI, 50% decrease in FFT, and 30% decrease in R1 calculated fission source versus D_2O tank fission source were observed. All of these factors will contribute to the FMESH method and thus the reactor power measurements. Similarly, these effects were investigated by taking R1 open pool as a reference case.

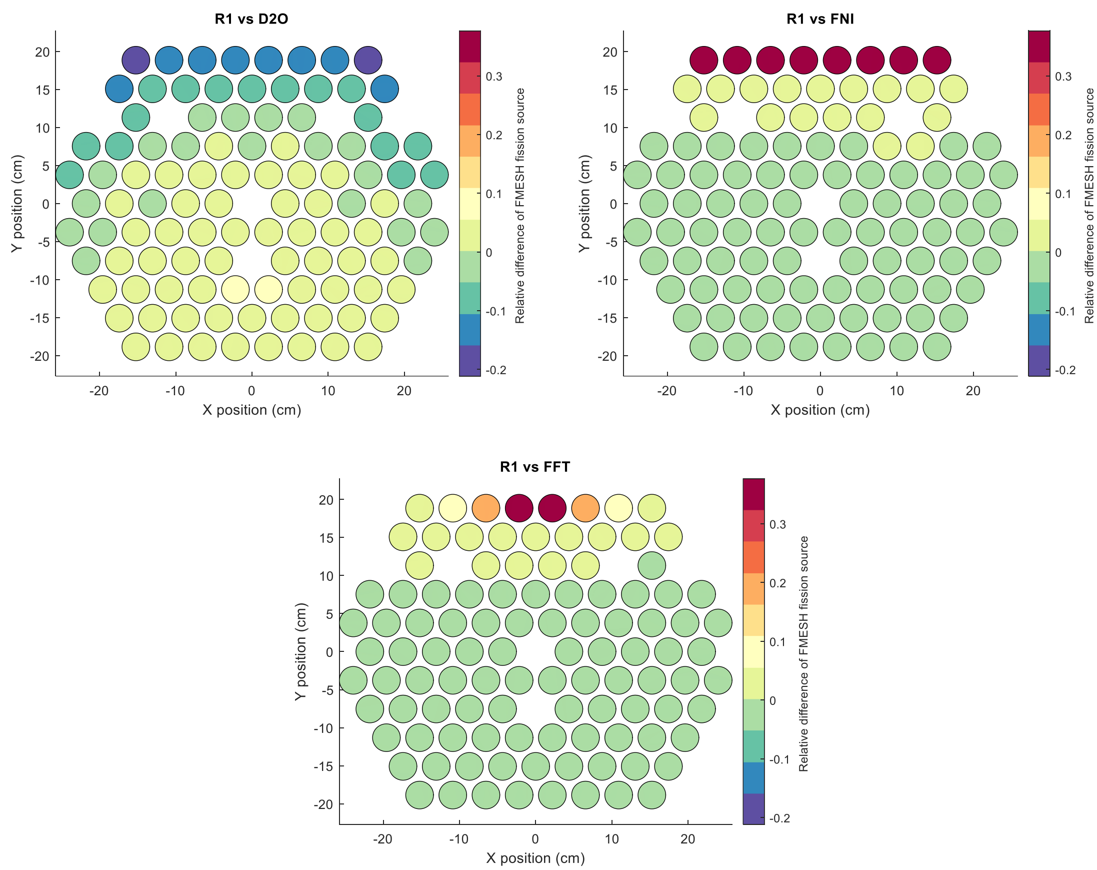

Figure 5-29. Relative fission source change for R1 versus D_2O, FNI, and FFT, respectively

Figure 5-29 shows the effect of locality on fission source at reactor power simulated at 1000 kW. Similar to Figure 5-28, the effect of having a structural material near the reactor core on the fission source was observed.

All of these locations` simulations were completed with the FMESH method for all power levels. Table 5-7 shows the FMESH method results in reaction rate in the detector region per source particle for all core localities and ex-core detectors at 1000 kW reactor power. In addition, relative change between the FMESH method for D_2O versus other core localities is shown.

Table 5-7. The reaction rate in detector region per source particle for ex-core detectors and relative percent change of localities versus D_2O tank at 1000 kW

	D_2O	R1	FNI	FFT	D_2O vs R1	D_2O vs FNI	D_2O vs FFT
RSS FC	3.3834E-7	3.5168E-7	3.5829E-7	3.5590E-7	3.79	5.57	4.93
SFC	1.9271E-7	1.9980E-7	2.0425E-7	2.0125E-7	3.55	5.65	4.24
CIC	2.1618E-5	2.2905E-5	2.2960E-5	2.3117E-5	5.62	5.85	6.46
GIC	1.8267E-7	1.8013E-7	1.8415E-7	1.8331E-7	-1.41	0.80	0.35

*Uncertainties are less than 0.7% for all cases

The results of the FMESH method in Table 5-7 show the difference in the core localities with the simulation. The fission source differences were approximately between 30% and 70 % which is shown in Figure 5-28. The FMESH results are significantly less than that since ex-core detectors are located at the other end of the reactor core compared to experimental fixtures. For this reason, the FMESH method results are slightly affected by the fission source distribution due to the effect of individual fuel element contribution being the dominant factor in calculations.

Referencing Table 5-7, if reactor power is assumed to be 1000 kW at the D_2O tank location as measured by the RSS fission chamber, the reactor powers will be 962.1, 944.3, and 950.7 kW at the R1, FNI, and FFT, respectively. RSS fission chamber and spare fission chamber results are consistent between each other and within uncertainty limits. The CIC shows the greatest change between the core locality effects.

5.4.2 Core Locality Effect and Control Rod Position Change

In this section, a combination of core locality and control rod position change effects were investigated for all detectors. Figure 5-30 shows the FMESH method detector responses for each core localities and control rod positions.

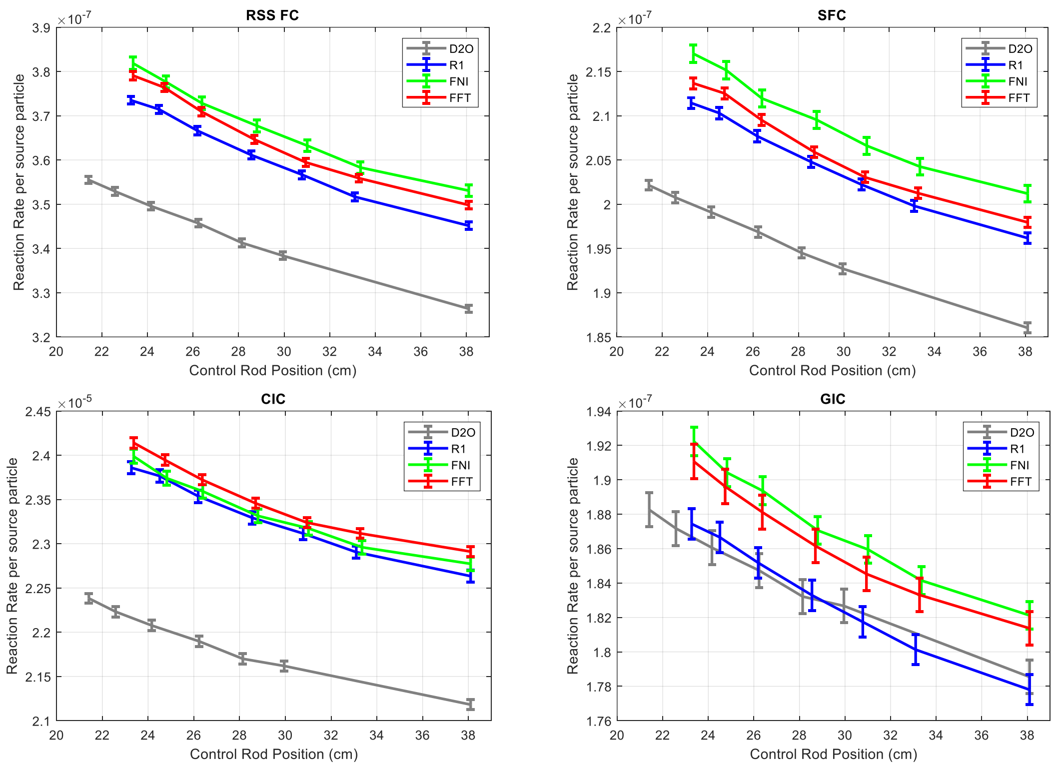

Figure 5-30. FMESH reaction rate per source particle values for detector responses for different core localities and control rod positions

According to Figure 5-30, all detector responses decreased with the control rod withdrawal in each core locality which is expected and explained in previous chapters. Withdrawing the control rod shifts the fission source distribution to the center of the core, thus resulting in a decrease in the ex-core detector region.

In addition, D_2O tank FMESH results have the lowest detector responses in all the figures above. This proves that the highest reactor power will be achieved at the D_2O tank location with the lowest control rod withdrawal. In the RSS Fission chamber and spare fission chamber, R1 has the lowest result, then FNI and FFT follow. In the compensated ion chamber, FNI and FFT results are observed to be opposite. This shows that R1 has the highest reactor power compared to these three locations. FNI and FFT results vary by the detector which needs to be corrected in the detector response section. Finally, the gamma ion chamber has similar results to each other even with the low uncertainty, it is hard to do a comparison between the D_2O tank and R1 open pool; FNI, and FFT.

Since the ex-core detectors have different behaviors for various core localities, FMESH results are compared by looking at percent change between 1 W vs 1000 kW and 1 W vs all-rods out case in Table 5-8, respectively.

Table 5-8. FMESH detector response percent change between 1 W vs 1000 kW and 1 W vs all-rods out case, respectively

	D_2O	R1	FNI	FFT	D_2O	R1	FNI	FFT
RSS FC	5.07	6.20	6.57	6.51	8.93	8.22	8.15	8.37
SFC	4.90	5.83	6.25	6.17	8.67	7.79	7.86	7.94
CIC	3.53	4.16	4.47	4.42	5.66	5.41	5.33	5.36
GIC	3.06	4.06	4.39	4.23	5.44	5.42	5.55	5.34

*Uncertainties are less than 0.7% for all cases

The percent change differences for each detector for using two different reference powers shown in Table 5-8. These results will be used in the detector response section to correct reactor power.

This section proves that there is significant power inconsistency between core localities that needs to be corrected. The computational results obtained in this chapter will be used in the detector response and power correction section.

5.4.3 Core Locality Effect with Asymmetrical Control Rod Insertion and Withdrawal

This section focuses on the investigation of the asymmetrical control rod insertion and withdrawal incorporating core locality effects on detector responses. Similar to the previous section, the reactor core was simulated near R1 open pool, D_2O tank, FNI, and FFT experimental locations. All locations were simulated at 500 kW reactor power as the reference case. Hereafter, control rods are asymmetrically inserted and withdrawn from the reactor core using transient and safety rods by two inches. Finally, the same asymmetrical insertion and withdrawal are executed by shim and regulating rod for all core localities.

Figure 5-31 shows the two inches of asymmetrical insertion and withdrawal of the transient and safety rod effect on each ex-core detector for the four different experimental localities.

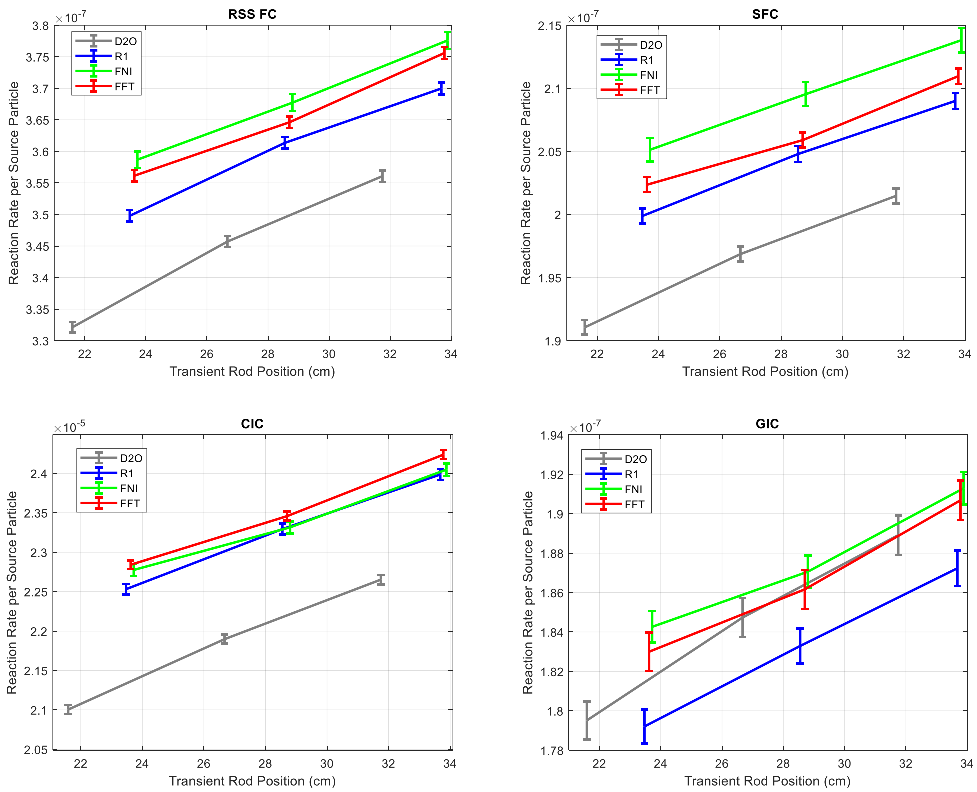

Figure 5-31. Two inches' asymmetrical insertion and withdrawal of the transient and safety rod effect on each ex-core detector for the four different experimental localities

According to Figure 5-31, all of the detectors have a higher reaction rate per source particle when the transient rod is withdrawn and the safety rod is inserted into the core. This means, in this configuration, the neutron flux profile shifts towards to detector region, thus giving higher FMESH results. In this configuration, the reactor power should be less since power multiplication with the reaction rate per source particle would give the same result.

Observing the behaviors of the detectors with asymmetrical control rod movement indicates that the, D_2O tank results are less from other core localities for the RSS fission chamber, spare fission chamber, and compensated ion chamber. RSS fission chamber and spare fission chamber trends are similar for R1 open pool, FNI, and FFT locations. There is a minimal change for these locations in the compensated ion chamber. Finally, the gamma ion chamber results are close to each other. Table 5-9 shows the percent changes from transient rod withdrawal to transient rod insertion asymmetrical control rod movement.

Table 5-9. Percent changes from transient rod withdrawal to transient rod insertion in asymmetrical control rod movement by two inches'

	D_2O	**R1**	**FNI**	**FFT**
RSS FC	7.23	5.77	5.27	5.47
SFC	5.44	4.55	4.24	4.25
CIC	7.86	6.48	5.62	6.13
GIC	5.23	4.46	3.80	4.21

Table 5-9 shows the percent changes for withdrawal and insertion of the transient and safety rod. The D_2O tank is the highest affected core locality for the asymmetrical insertion and withdrawal of the transient and safety rods. It was explained previously that the D_2O tank tilts the neutron flux profile away from the ex-core detectors through to the D_2O tank. This effect is combined with the asymmetrical control rod movements, thus giving the highest difference in this configuration since the transient rod is the closest control rod to the ex-core detector location and safety rod is the closest control rod to the experimental fixtures such as the D_2O tank. The lowest percent change was observed in the gamma ion chamber and R1 has the second-highest, while the FFT has the third-highest percent change for all detectors.

Similar to the asymmetrical control rod movement of transient and safety rods, shim and regulating rod asymmetry was also investigated for all core localities using ex-core detectors.

Figure 5-32 shows the two inches asymmetrical insertion and withdrawal of the shim and regulating rod effect on each ex-core detector for the four different experimental localities.

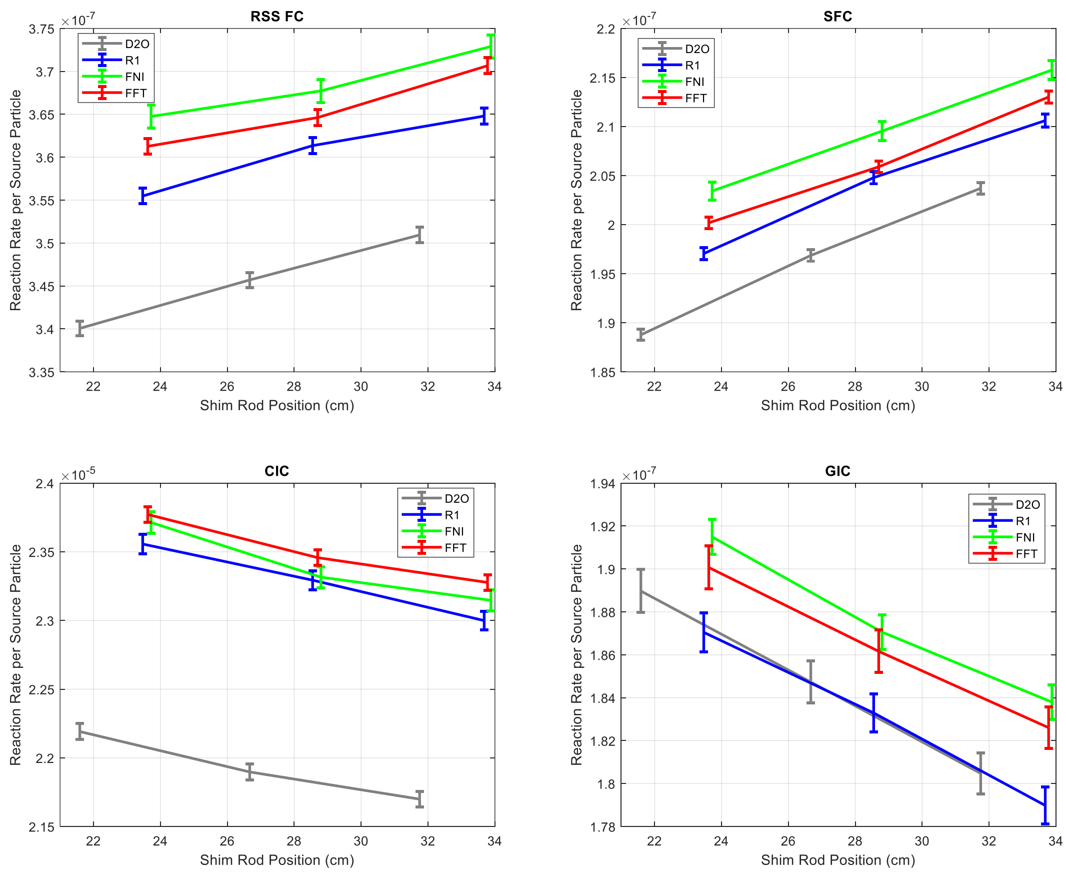

Figure 5-32. Two inches' asymmetrical insertion and withdrawal of the shim and regulating rod effect on each ex-core detector for the four different experimental localities

According to Figure 5-32, the behavior of the detector responses is different depending on the detector and type of the asymmetry. This is due to the locality of the control rods and how far they are located compared to the ex-core detector locations. In this configuration, the neutron flux profile shifts towards to east or west side of the reactor core.

By looking at the behaviors of the detectors with asymmetrical control rod movement, the D_2O tank results are smaller than other core localities for the RSS fission chamber, spare fission chamber, and compensated ion chamber. The RSS fission chamber and spare fission chamber trends are different this time for the R1 open pool, FNI, and FFT locations since the RSS fission chamber is located close to the reactor core center, but the spare fission chamber is located close to the edge of the east side. The Compensated ion chamber and gamma ion chamber results are opposite compared to the RSS fission chamber and spare fission chamber due to a change in fission source caused by the asymmetrical rod insertion. Table 5-10 shows the percent changes from shim rod withdrawal to shim rod insertion in two inches' asymmetrical control rod movement.

Table 5-10. Percent changes from shim rod withdrawal to shim rod insertion in two inches' asymmetrical control rod movement

	D_2O	R1	FNI	FFT
RSS FC	3.17	2.62	2.25	2.60
SFC	7.89	6.85	6.10	6.39
CIC	-2.21	-2.38	-2.36	-2.06
GIC	-4.50	-4.28	-4.02	-3.95

Table 5-10 proves the different trends and percent changes caused by the asymmetrical control rod movement due to insertion and withdrawal of the shim and regulating rod over to detector responses in four core localities. The RSS fission chamber and spare fission chamber have positive changes, while the compensated ion chamber and the gamma ion chamber have a negative change in results. This is due to the RSS fission chamber and spare fission chamber being located on the east side of the reactor core and compensated ion chamber and gamma ion chamber being located on the west side of the reactor core. The spare fission chamber is the most affected in this asymmetrical control rod movement configuration due to neutron flux shifting towards the east and west of the reactor core, where this detector is located at the east of the reactor core. Core locality changes have a similar effect on detectors except for the compensated ion chamber. D_2O tank results at this location have a smaller difference which means this configuration of asymmetry does not affect the compensated ion chamber results drastically.

This section proves that the asymmetry provided by four different control rods has a significant effect and change on the results. In the future, if an experiment is planned to contain the asymmetrical movement of the control rods, more precautions should be taken when estimating reactor power.

Chapter 6

Experiment of ex-core detectors and new miniature fission chamber

This chapter describes the experiment conducted at the PSBR. This experiment is to demonstrate how neutron flux is affected by the asymmetrical control rod movement inside and outside of the reactor core. The best way to do this is to create an experimental approach that implements the simulations into a real-life application. The detectors at the PSBR are located at the back of the reactor core. There is no detector located inside the reactor core, thus no information can be gathered during the operation about the neutron flux. One way to investigate this is by placing a detector inside the central thimble. By doing this, the neutron flux change can be investigated and compared for the ex-core detector region versus the reactor core center. The PSBR has extensive capabilities to experiment with various configurations. Researchers can irradiate materials and detectors in multiple reactor operation locations with a wide range of reactor power depending on the needs of the research.

In this experiment, the WL-7186 fission chamber will be placed into a central thimble, and asymmetrical insertion of various configurations will be investigated for all detectors at low power. Then, the WL-7186 will be removed from the core and a high-power experiment will be performed for ex-core detectors.

The PSBR has various safety protocols to ensure the safety of any irradiation experiments. Researchers have to prepare an experimental evaluation and authorization form, often referred to as Standard Operation Procedure-5 (SOP-5). The SOP-5 form contains several sections that need to be addressed before the experiment. These sections are the description of the experiment with details such as the average neutron exposure data, radioactivity calculations for each material after a given decay time, Ar-41 production, reactivity change due to experiment in the core, other considerations such as failure mechanisms, and iodine inventory calculations in case of accident scenarios. Section 6.1 describes the WL-7186 miniature fission chamber and how required parts are manufactured. Section 6.2 explains and shows the followed procedure to create the SOP-5 form for the experiment which includes activity and dose calculations, the iodine inventory calculation, and the reactivity calculation. Section 6.3 shows the detector plateau and high voltage determination, section 6.4 shows the low power asymmetrical control rod movement effect on the detectors, and section 6.5 shows the high power ex-core detector behavior investigation for all core localities. Section 6.6 investigates the high power asymmetrical control rod effect on detectors for all core localities. Finally, section 7.3 compares the experimental results with the simulations.

6.1 WL-7186 Description

As mentioned previously, in the current reactor operation, there is no information about the neutron flux profile in the center of the reactor core since ex-core detectors are located outside of the reactor core. The detector that will be placed into the central thimble should be very small and work under the water. Also, this detector should be sensitive to the thermal neutrons. RSEC has various neutron and gamma detectors that are available for research. The only candidate that could work for this experiment conditions was the Westinghouse WL-7186 fission chamber which was available in RSEC inventory.

The WL-7186 miniature fission chamber contains 0.0027 grams of 90% enriched Uranium 235. Thermal neutrons incident on the coating produce fission fragments which ionize the argon-nitrogen gas fill, producing pulses. Pulse shaping is required using a preamplifier, amplifier, and single-channel analyzer. The unit has a stainless steel waterproof body. The length of the tubing is around 54 inches and the dimensions can be seen in Figure 6-1.

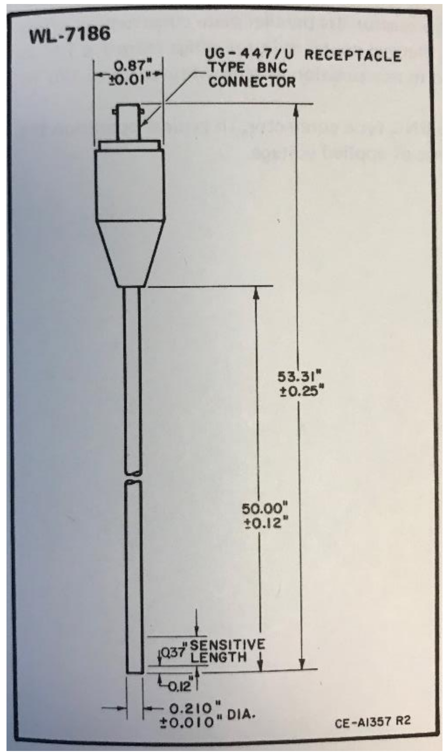

Figure 6-1. WL-7186 miniature fission chamber dimensions [47]

Radiation detectors permit the electrical current between electrodes when they are exposed to penetrating radiation. At low levels of neutron flux, the current pulses created by the incident particle do not create a steady current. For this reason, in low flux applications, high sensitivity radiation detectors such as fission counters are used in pulse counting. The detector output is fed into the preamplifier and then the amplifier. Pulses created by the detector are proportional to the number of incident particles, thus the neutron flux at the detector location.

This fission chamber must be able to operate under the water. The stainless steel and detector regions can operate under the water. However, the brass heading contains a BNC connector that cannot be exposed to the water environment to avoid shorting the circuit. Since the reactor core is located about 24 ft. under the water, the brass heading with the BNC connector region needs to be waterproofed before the experiment. Figure 6-2 shows the side view and the top view of the WL-7186 fission chamber heading.

Figure 6-2. Side view and top view of the WL-7186 fission chamber brass heading and BNC connection

Several ideas were considered to develop a fission chamber module and the final design is provided in Figure 6-3 including a brass heading, adapter, BNC cable, and waterproof housing.

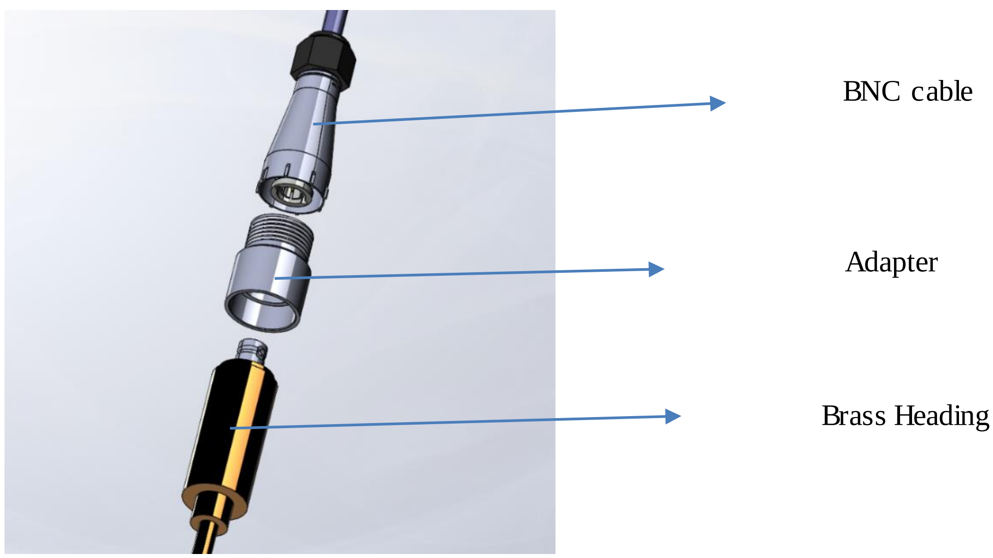

Figure 6-3. Fission chamber brass heading connection design

An adapter was designed that fit on top of the brass heading and surrounds the entrance of the BNC connection. Epoxy is placed around the junction point of the brass heading and adapter to make sure water cannot penetrate inside the crack. An O ring was placed at the end of the screw region of the adapter and connected to the Pasternack IP68 waterproof coaxial cable.

Figure 6-4 shows the adapter assembly connected to the brass heading of the detector and the adapter assembly connected to the waterproofed BNC cable housing.

Figure 6-4. Adapter connected to the brass heading and waterproofed BNC cable housing

After the manufacturing of the adapter was finalized, the connection points of the brass and adapter were sealed with epoxy and waited for a week to cure. After the cure time, the detector assembly was placed into the PSBR pool water to test for water leaks. After 3 days, no leak was detected inside the brass heading and BNC connector area. Final detector assembly and waterproof testing can be seen in Figure 6-5.

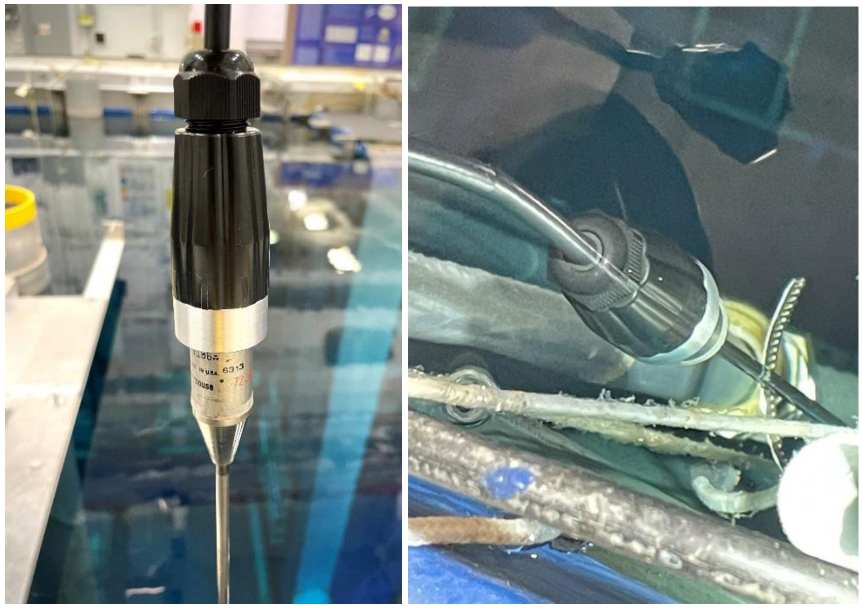

Figure 6-5. Final assembly of the fission chamber brass heading to waterproof

The specification of the detector does not give the masses of the materials. Several assumptions were made to estimate the correct mass amount of the materials for calculations. These calculations are important when determining post-irradiation activity to predict and minimize worker/experimenter dose. First, the volume of each material is calculated. Then with given densities, masses of the materials are calculated for brass and stainless steel. The total mass of the detector system was given to be 225 g. To have conservative results, both brass and stainless-steel masses were assumed to be 225 g. Defining the mass of the other materials is challenging because there is no mechanical description for them. For Argon-nitrogen gas, the volume of the active region is calculated. Using the ideal gas law at room temperature and 2 atm pressure, the mass of the gas was calculated as 0.0027 g. To have conservative results, this number was rounded up to 0.01 g. Teflon, alumina, and steel are assumed to be inner electrode and insulation material which is very thin. For a regular wire, the diameter is assumed 0.6 cm where each material has a 0.1 cm radius. The total volume of each was calculated as 4.15, 12.44, and 20.73 cm^3 for the steel rod, Teflon, and alumina, respectively. WL-7186 material descriptions are given in Table 6-1 with weights and compositions.

Table 6-1. WL-7186 Material Descriptions

Material	Mass (g)	Weight Fraction							
Brass	225	Fe 0.000868	Cu 0.665381	Zn 0.325697	Sn 0.002672	Pb 0.005377			
Stainless Steel	225	C 0.0004	Si 0.005	P 0.00023	S 0.00015	Cr 0.19	Mn 0.01	Fe 0.70173	Ni 0.0925
U308	0.3	O 0.153488	U-235 0.76185	U-238 0.0846504					
Teflon	30	C 0.240183	F 0.759818						
Alumina	80	O 0.470749	Al 0.529251						
Ar-N2	0.01	Ar 0.0058	N2 0.0041						
PE Tube	10	C 0.8563	H 0.14371						
Steel	32	C 0.005	Fe 0.955						

6.2 SOP-5 Calculations

As mentioned above, several calculations need to be performed before irradiating a sample in the reactor core. These calculations ensure there will be no safety violations during the experiment. The dose rate after removing the detector should be in mrem/h levels. In addition, iodine inventory cannot exceed 1.5 Ci at any time of the experiment. Finally, reactivity due to foreign material should not exceed 0.1$. This section explains the required calculations for the SOP-5 including activity, dose rate, iodine inventory, and reactivity calculations.

6.2.1 Activity and Dose Rate Calculations

The experimental procedures and the activity predictions are based on a combination of the archived information available in RSEC records and new activity prediction calculations performed by Sahin [48]. These predictions are also compared with the online tools available by NIST, Wise Uranium Project, and The Technical University of Munich activity predictor tools. Activity calculations made here are done for the fission chamber being irradiated for 3 hours in a 1 kW reactor operation, which is a very long time at a 1 kW operation for this experiment, but calculations are done to show the most conservative results. The experiment is planned to be done at 1 W, but calculations are done for 1 kW to get the most conservative calculations for the safety limits.

The experimental irradiations will take place in the central thimble with a WL-7186 fission chamber. This fission chamber consists of a BNC connector on top attached to the brass head, which is approximately 130 cm away from the reactor core center, stainless steel body length of 127 cm, and its center approximately 65 cm away from the reactor core. The active region is placed on the bottom of the structure which will be centered with the reactor core.

Neutron flux will be varied axially and is highest in center of the reactor core where active region of the fission chamber will be placed. The flux will be reduced in the upper regions where the stainless-steel and brass section of the detector will be placed. To investigate the difference in neutron flux, F4 flux tallies were created in three locations with MCNP: fission chamber active region, the center of the stainless-steel tube, and the center of the brass. Table 6-2 shows estimated flux values at the three locations for 1 W reactor operation. Uncertainties are high where the stainless steel and brass are located, for this reason, the highest value is taken that includes uncertainty. MCNP tally results are normalized per source particle. These tally results are multiplied with a factor that includes the reactor power, average neutrons per fission, and average energy per fission at 1 MW of power which is shown in Equation 6-1.

$$Factor = 1\ MW \times \frac{10^6 W}{1\ MW} \times \frac{1\frac{J}{s}}{1\ W} \times \frac{1\ MeV}{1.60218^{-13} J} \times \frac{1\ fission}{200\ MeV} \times \frac{2.4\ neutrons}{fission} \quad \text{Equation 6-1}$$

$$Factor = 7.7 \times 10^{16}$$

Neutron flux can be calculated by multiplying the MCNP tally result and the factor described above which is shown in Equation 6-2.

$$Neutron\ Flux\left(\frac{neutrons}{cm^2 - s}\right) = MCNP\ Tally\ Result\left(\frac{neutrons}{cm^2 - source\ particle}\right) \times Factor \quad \text{Equation 6-2}$$

In addition, since the brass section is about 130 cm away from the reactor core, zero tally results were achieved for this tally. The results shown below for the brass are calculated based on the linear change between the detector region to stainless steel and stainless steel to the brass section.

Table 6-2. Flux estimations for three axial locations at the central thimble (n/cm^2-sec)

	MCNP Thermal Flux Tally	MCNP Fast Flux Tally	Factor for multiplication	Thermal Neutron Flux n/cm^2-sec	Fast Neutron Flux n/cm^2-sec
Detector	5.27E-04	4.53E-04	7.70E+16	3.92E+7	3.40E+7
SS	1.17E-07	2.88E-08	7.70E+16	8.69E+3	2.1E+03
Brass	2.58E-11	1.83E-12	7.70E+16	1.92	0.133

*Uncertainties are less than 1% for detector location

Activity and gamma-ray exposure rates were calculated using the RSEC Activity Predictor Program by D. Sahin which is a standard method to calculate activities and exposure rates in RSEC. In this program, the user selects the desired irradiation location and the program calculates the neutron flux using the previous experiments. Users can define new materials or use the existing material list to model the experiment. Then, the program calculates activities and dose rates depending on the irradiation time, the calculated flux at the position, decay constant, and cross-section for each isotope. Results of these calculations are compared with the other activity tools and the highest values are considered.

As mentioned before, four different activity predictors were used which were developed by NIST, Wise Uranium Project, and The Technical University of Munich. The assumption made here was that the reactor power is at 1 kW for three hours to get the most conservative activity predictions. Results were compared between four different activity predictor tools and the most conservative results were selected.

For the gamma-ray exposure rate, a gamma-ray constant table was used from ORNL/RSIC-45 "Specific Gamma-ray Dose Constants for Nuclides Important to Dosimetry and Radiological Assessment", May 1981 [49]. Gamma Dose rate calculations are shown in Equation 6-3.

$$\textbf{Gamma Dose Rate}\left(\frac{\textbf{mrem}}{\textbf{h}}\right) = \Gamma\left(\frac{\text{Gamma} - \text{Ray}}{Dose\ Constant}\right)\frac{rem \times m^2}{Ci\ \times\ h} \times \frac{1}{Distance^2(m^2)} \times Activity(Ci) \times 10^3 \qquad \text{Equation 6-3}$$

Only the highest activity isotopes are considered to calculate gamma-dose rate calculations since they have a higher contribution.

Similarly, the beta-dose rate calculation is done with Equation 6-4.

$$\boldsymbol{Beta\ Dose\ Rate}\left(\frac{\boldsymbol{mrem}}{\boldsymbol{h}}\right) = 300 \times \frac{1}{Distance^2(feet^2)} \times Activity(Ci) \times 10^3 \qquad \text{Equation 6-4}$$

The formulas provided above were tested for several isotopes and compared with the online tools available. The results matched well with each other and can be seen in Table 6-3.

Table 6-3. WL7186 D_2O tank activity and dose rate predictions

Material	Brass	Stainless Steel	U308	Teflon	Alumina	Ar-N	PE	Steel
1 h Irradiation 1 kW (mCi)	6.66E-5	1.97E-2	1.80E-3	3.39	5.23E-2	1.92E-2	0	1.78E-5
Decay of 1 hours (mCi)	1.38E-5	1.42E-2	3.45E-4	2.59E-4	1.49E-5	1.31E-2	0	1.36E-5
Gamma-ray Dose Rate (mrem/h)	1.78E-5	0.142397	5.97E-4	2.00E-3	0.00018	0.10155	0	1.39E-4
Beta Dose Rate (mrem/h)	4.00E-6	4.13E-3	9.72E-5	7.50E-5	4.33E-6	3.81E-3	0	3.94E-6

Total Beta Dose Rate:8.12E-3 mrem/h, Total Gamma Dose Rate: 2.47E-1 mrem/h

Table 6-3 shows that the activities are less than 5 mCi even right after the irradiation. For this reason, no additional calculations were done for the open pool location experiment, and it is expected to be a similar result to D_2O tank calculations. For conservative results, Table 6-3 results are multiplied by two. Gamma and beta dose rates were calculated for each experiment and added to the result.

6.2.2 Iodine Inventory Calculations

The total iodine inventory for isotopes 131 - 135 for a fueled experiment must be less than 1.5 Ci. This section describes how iodine inventory calculations are done for this experiment.

Since the fission chamber has highly enriched U-235, the iodine inventory is expected to be higher than the 5 mCi lower limit which needs a detailed investigation for the iodine inventory. The experiment was divided into two sections to make sure iodine inventory was not exceeding the limit of 1.5 Ci for open pool and D_2O tank locations.

For the calculations, thermal flux and fast flux are taken from the previous section at 1 kW operation for 3 hours (1 hour 1 W at Open Pool, 1hour 1 W at D_2O tank, and 1kW test for 1 hour). This conservative iodine calculation results showed in Table 6-4 and a sample Excel sheet to calculate iodine inventory is shown in Figure 6-6.

Table 6-4. Iodine Calculation Results

	Activity (mCi)
1 kW Irradiation for 3 hours	23.74 mCi
1 hour of decay	1.72 mCi

1	**Input**							
2	Reactor Power		1000	kW				
3	Enrichment Level		90	%				
4	Irradiation Time		600	s				
5	Sample		0.003					
6	U-235	Mass	0.0027	g		# of Atoms	U-235	6.92E+18
7	U-238		0.0003				U-238	7.59E+17
8								
9	**Output**							
10	# of Fissions	U-235	4.62E+11	per sec		# of Fissions	U-235	2.77E+14
11		U-238	1.67E+05			at the end	U-238	1.00E+08
12							**TOTAL**	**2.77E+14**
13								
14	**Calculations For Iodine Production Limits**					Decay Time	43200 s	
15								
16	From U-235							
17	Nuclide	Half-life (s)	Fraction Cum Yield		lambda (1/s)	Activity (Bq)	Activity (mCi)	
18			Thermal	Fast			End of Irrad	After Decay Time
19	I - 131	694656	0.028784	0.033648	9.9783E-07	8.64E+06	2.34E-01	2.24E-01
20	I - 132	8208	0.042953	0.046953	8.4448E-05	1.05E+09	2.85E+01	7.41E-01
21	I - 132m	4993.2	0.000088216	0.00028347	1.3882E-04	7.16E+06	1.93E-01	4.81E-04
22	I - 133	74880	0.065948	0.066091	9.2568E-06	1.70E+08	4.58E+00	3.07E+00
23	I - 133m	9	0.00093422	0.0024508	7.7016E-02	3.62E+10	9.77E+02	0.00E+00
24	I - 134	3156	0.07743	0.076924	2.1963E-04	4.70E+09	1.27E+02	9.63E-03
25	I - 134m	222	0.0040956	0.010251	3.1223E-03	6.21E+09	1.68E+02	4.43E-57
26	I - 135	23688	0.063853	0.060085	2.9262E-05	5.03E+08	1.36E+01	3.84E+00
27							1.32E+03	7.89E+00
28	From U-238							
29	Nuclide	Half-life (s)	Fraction Cum Yield		lambda (1/s)	Activity (Bq)	Activity (mCi)	
30			Thermal	Fast			End of Irrad	After Decay Time
31	I - 131	694656		0.03321	9.98E-07	3.31E+00	8.95E-08	8.57E-08
32	I - 132	8208		0.047572	8.44E-05	4.02E+02	1.09E-05	2.83E-07
33	I - 132m	4993.2		6.6932E-06	1.39E-04	9.29E-02	2.51E-09	6.24E-12
34	I - 133	74880		0.067129	9.26E-06	6.21E+01	1.68E-06	1.13E-06
35	I - 133m	9		0.00012612	7.70E-02	9.71E+02	2.62E-05	0.00E+00
36	I - 134	3156		0.068226	2.20E-04	1.50E+03	4.05E-05	3.07E-09
37	I - 134m	222		0.0010176	3.12E-03	3.18E+02	8.58E-06	2.26E-64
38	I - 135	23688		0.064209	2.93E-05	1.88E+02	5.08E-06	1.43E-06
39							9.30E-05	2.93E-06
40						**TOTAL**	**1.32E+03**	**7.89E+00**

r1 flux

Flux Ratio	
Thermal	Resonance + Fast
3.50E+13	3.50E+13
Normalizaed to one	
5.000E-01	5.000E-01

U-235

	Range
Thermal	0.0001 eV – 0.55 eV
Fast	0.55 keV – 20 MeV

# of	Fissions
Total # of	

92-U-235(n, total fission) ENDF/B-VII.1

Energy (MeV)	XS (cm^2)
1.12E-10	9388.24
1.46E-10	8226.34
1.91E-10	7179.04
2.49E-10	6289.66
3.27E-10	5488.19
4.25E-10	4807.52
5.58E-10	4194.09
7.27E-10	3672.88
9.54E-10	3203.12
1.24E-09	2803.94
1.63E-09	2443.91
2.12E-09	2138.05
2.79E-09	1861.75
3.63E-09	1626.14
4.76E-09	1412.98
6.20E-09	1232.01
8.13E-09	1068.99
1.06E-08	931.122
1.39E-08	806.985
1.90E-08	683.747
2.35E-08	609.832
2.53E-08	585.472

Figure 6-6. Sample iodine inventory calculator sheet using Excel spreadsheet

The detector is removed from the core and higher power results will be obtained without any foreign material in the core, thus there will be no need to do extra iodine calculations for the SOP-5.

6.2.3 Reactivity Calculations

To estimate the reactivity change due to the insertion of the WL-7186 fission chamber into the central thimble, a MCNP model is created. The first model does not contain this fission chamber and in the second model, the WL-7186 geometry and material list are included in the MCNP model. KCODE calculations are done with 100000 particles with 300 cycles for a 1 MW reactor operation. Reactivity is calculated by Equation 6-5.

$$\rho = \frac{k_{eff} - 1}{k_{eff}} \qquad \text{Equation 6-5}$$

k_{eff} is estimated as 1.01362 with a standard deviation of 0.00134 with the detector installed to the central thimble. k_{eff} is estimated as 1.01160 with standard deviation of 0.00111without the detector installed on the central thimble. Reactivity change calculated:

$$\rho_1 = \frac{1.01362 - 1}{1.01362}$$

$$\rho_1 = 0.01343 \pm 0.00134$$

$$\rho_2 = \frac{1.01160 - 1}{1.01160}$$

$$\rho_2 = 0.01147 \pm 0.00111$$

$$\rho_1 - \rho_2 = 0.00196 \pm 0.00174$$

$$\Delta\rho/\beta = 0.00196/0.0065 = 0.30 \pm 0.26\$$$

MCNP has challenges to calculate small changes in reactivity due to the high uncertainty in the k_{eff}. This uncertainty could be reduced by using more particles. The reactivity change due to the fission chamber is investigated during the experiment and it was determined that less than 0.1$ of reactivity is inserted into the core by the WL-7186 fission chamber.

6.3 Detection System and High Voltage Plateau Determination

The detection system consists of a preamplifier that is connected to the BNC output of the fission chamber. The preamplifier is connected to a high voltage power supply to provide the required high voltage for the detector which is between 250-450 V. The preamplifier is also connected to the amplifier. Similarly, the amplifier is connected to the Single Channel Analyzer (SCA) and the SCA is connected to both the counter and oscilloscope. The detection system scheme can be seen in Figure 6-7 and the NIM bin configuration can be seen in Figure 6-8. Before the experiment, each component of the detection system is tested with a pulser by varying input and observing the output by oscilloscope.

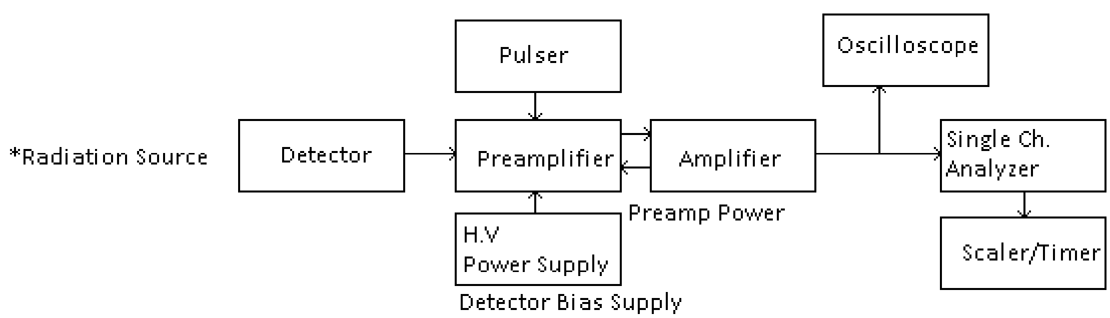

Figure 6-7. Circuit diagram of the radiation detection system that was used in the experiment

Figure 6-8. NIM Bin that house detection system equipment

The detector, WL-7186 was bought in 1978 but has never been used in radiation or any other environment. The new detectors need a good warmup period, 90 minutes for a new miniature fission chamber detector or as little as 30 minutes for a used one according to the manufacturer. This allows time to establish an equilibrium fission product distribution prior to setting the plateau voltages. Used detectors with a lot of operating history may already have established equilibrium of the long-lived fission products. The detector was placed into the central thimble from the top of the reactor bridge with the aid of equipment to accurately place the active region of the detector matching with the center of the reactor core. About 2.5 hours of warmup period was used.

After a warmup period with high voltage, the amplifier gains, and SCA upper and lower window limit is tuned. The neutron interaction in the detector should create a voltage signal that needs to go to the preamplifier and then it is amplified by the system. Only meaningful signals should be selected by the SCA window. Figure 6-9 shows the logic pulse created by the SCA due to interaction at the fission chamber.

Figure 6-9. Logic pulse created in the SCA by the neutron interaction in the fission chamber

Depending on when the detector was last used, re-finding the plateau voltage may be necessary to ensure an accurate measurement since the high voltage plateau may drift with time. When setting up a pulse counting measurement, it is often desirable to establish an operating point that will provide maximum stability over long periods of time. In general, regions of minimum slope on the integral distribution are called counting plateaus and represent areas of operation in which minimum sensitivity to drifts in discrimination level is achieved and gives minimal impact to the number of pulses recorded [50]. The fission chambers usually have a pretty wide plateau but can drift over time depending on when it was last measured. The WL-7186 is rated for 250-450 V of operating voltage with 500 V maximum voltage. To acquire a detector voltage plateau, high voltage power is increased from 0 to 450 V in 50 V steps. In each voltage, 2 minutes of counts are taken and recorded.

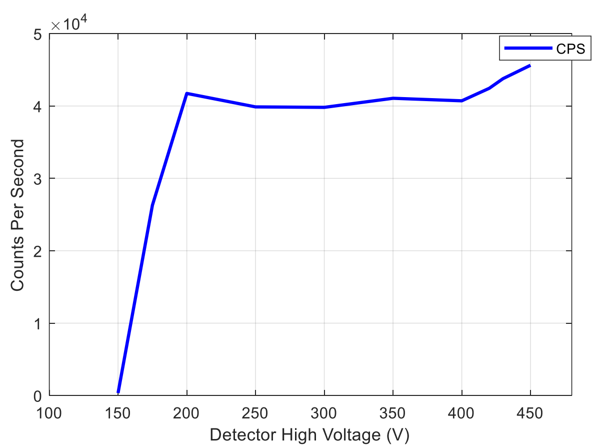

Figure 6-10. WL-7186 fission chamber high voltage plateau curve

It can be seen from the Figure 6-10 that the WL-7186 has a flat detector voltage plateau in the specified operating range. Since it is an ionization chamber type detector, it makes sense that the plateau is flat in the operating range and then increases at the end which corresponds to the proportional region like in Figure 6-11.

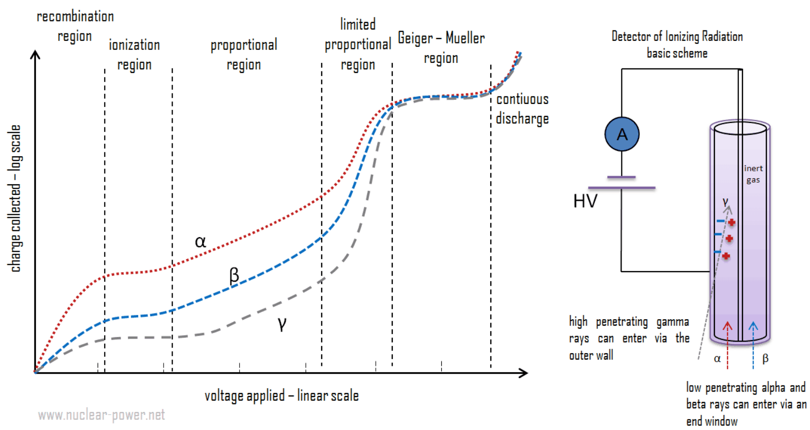

Figure 6-11. Regions of gaseous ionization detectors [51]

After the detector voltage plateau determination and checking that the electronics work properly, it was decided to operate the detector in the middle of the plateau which is about 350 V. Background measurements were also taken at zero power and 1W of reactor operation.

6.4 Low Power Asymmetric Control Rod Movement

The PSBR can operate up to 1MW power with a thermal flux of $3 \times 10^{13}\ n/cm^2s$ in the central thimble. The available fission chamber, WL-7186, can work up to $8 \times 10^7\ n/cm^2s$ according to the manual, which means the reactor power should be limited to around 1 W if this detector is to operate in the central thimble. Since the goal of the experiment is investigating neutron flux shape inside the reactor core, the WL-7186 fission chamber is placed into the central thimble and measurements are taken with 1 W reactor power. At this power, the thermal flux should be around $4.5 \times 10^7\ n/cm^2s$.

The first part of the experiment is done at the R1 location and it consists of a 1 W reactor operation with even control rods and taking the measurement from the detectors. The reactor was being started and the operator increased the power to 1 W with automatic control rod position which means all the control rods are even. After steady-state power measurement is observed from the console, two minutes of measurements are taken with the WL-7186 fission chamber. All the required information is recorded from the control console as well. After this, the operator takes the reactor in manual mode and removes the safety rod to the maximum control rod out position, 14.98 inches from the bottom, and inserts the transient rod to balance reactivity, thus balancing the reactor power. When steady-state reactor power is observed at 1 W from the control console, measurements are taken from the detector and control console. Finally, the operator removes the regulating rod to the maximum rod out position and balances the reactor power by inserting the shim rod. Similarly, measurements are taken with the detector and data is recorded from the control console. All results are shown in Table 6-5 for the R1 open pool location. All the temperatures recorded for this section were gathered from the instrumented fuel element.

Table 6-5. R1 open pool asymmetrical rod insertion at 1 W of reactor operation

RSS FC Power (kW)	Spare FC Log Power	GIC Power (kW)	WL-7186 (CPS)	TR Position (inches)	SF Position (inches)	SH Position (inches)	REG Position (inches)	Temperature (°C)
0.000950	-6.859	0.56	41558	9.19	9.16	9.16	9.16	19.9
0.001035	-6.839	0.56	42612	5.46	14.98	9.16	9.16	19.9
0.001085	-6.826	0.54	42653	5.46	14.98	5.24	14.98	19.9

After R1 open pool measurements are completed, the reactor is shut down and moved to the D_2O tank position. The same procedure is followed and measurements are taken. The results are shown in Table 6-6.

Table 6-6. D_2O tank asymmetrical rod insertion at 1 W of reactor operation

RSS FC Power (kW)	Spare FC Log Power	GIC Power (kW)	WL-7186 (CPS)	TR Position (inches)	SF Position (inches)	SH Position (inches)	REG Position (inches)	Temperature (°C)
0.001052	-6.841	0.58	43563	8.44	8.43	8.43	8.42	20.1
0.001028	-6.831	0.54	44056	2.93	14.98	8.43	8.42	20.0
0.001021	-6.891	0.54	44098	2.93	14.98	2.71	14.98	20.0

Results from Table 6-5 and Table 6-6 show a slight change in RSS FC and Spare fission chamber power readings. It is hard to say anything about the RSS fission chamber due to the reactor console reading fluctuating every second with great uncertainty. This number was recorded by the experimenter momentarily. The gamma ion chamber shows very high reactor power even in low powers. The reason is that the gamma ion chamber carries the fission product and delayed gamma–ray residuals which contribute to the interaction inside the gamma ion chamber. The results shown in Table 6-5 and Table 6-6 for the RSS fission chamber are instantaneous values observed by the experimenter.

The main focus of this chapter was to investigate how control rods are changing the detector responses with asymmetrical insertion and withdrawal. In the first part of the experiment, a miniature fission chamber was placed inside the central thimble. Counts were taken along with the ex-core detectors for the R1 open pool and D_2O tank locations. In these experiments, the reactor operated at 1 W to obtain a base case. Then, the safety rod was withdrawn from the core to the maximum position. Reactor power was kept constant at 1 W by inserting a transient rod. After steady state reactor power was observed, counts were taken and the regulating rod was removed from the core to the maximum position while keeping the transient and safety rod at earlier positions. Then, the shim rod was inserted to keep the reactor power steady. Counts were taken for all three cases for both the R1 open pool and D_2O tank location.

The miniature fission chamber is modeled inside the MCNP input file. The MCNP model consists of stainless steel tubing, an active region where fissile material is coated on the stainless steel and argon-nitrogen gas in the middle. An F4 flux tally is created like the ex-core fission chambers. The experimental control rod positions are also modeled in the input file. Figure 6-12 shows the estimated power versus asymmetrical insertion of control rods' effect on ex-core detectors and miniature fission chamber using MCNP at the D_2O tank. These results are also compared with the experimental values acquired for the miniature fission chamber which are shown in CPS. All values are normalized to one for the base case and relative change is estimated.

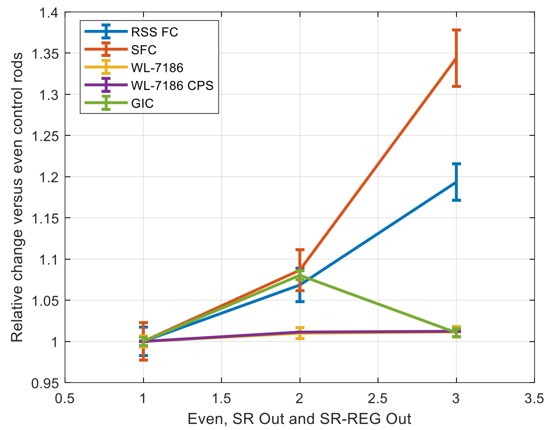

Figure 6-12. Estimated Power versus asymmetrical control rod insertion for ex-core detectors, miniature fission chamber by MCNP simulation, and experimental results from miniature fission chamber shown as CPS for D2O tank

Figure 6-12 shows the estimated reactor power for both simulation and experimental results for the miniature fission chamber along with ex-core detector simulations. In all cases, the reactor console reads 1 W of reactor power at the control console with existing detectors. Even position control rods case is assumed as a reference case which is 1 W of reactor operation for the Figure 6-12. Since the reactor console reads the same power in all cases, the same amount of fission reaction happens in the detectors for three cases. This means the same amount of thermal neutrons are available in the experiment for these three cases and reactor power is measured at 1 W. However, simulation results show that there is a change in reaction rates per source particle for three cases, which shows actual reactor power is not the same. There is a 32% difference in the spare fission chamber and an 18% difference in the RSS fission chamber. However, the miniature fission chamber experimental and simulation values show a similar trend in Figure 6-12. This also proves the detector in the central thimble is less affected by the reactor power shift compared to the ex-core detectors. This can be explained by Figure 6-13 and Figure 6-14 which shows the neutron flux shift due to asymmetrical insertion and locations of the control rods and the reactor core along with the detectors.

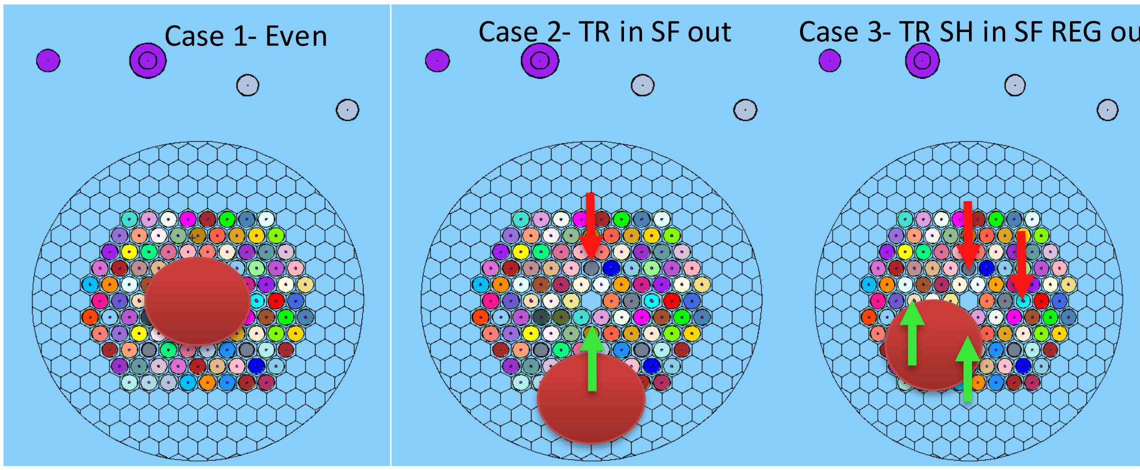

Figure 6-13. Expected neutron flux shift with asymmetrical control rod insertion and withdrawal

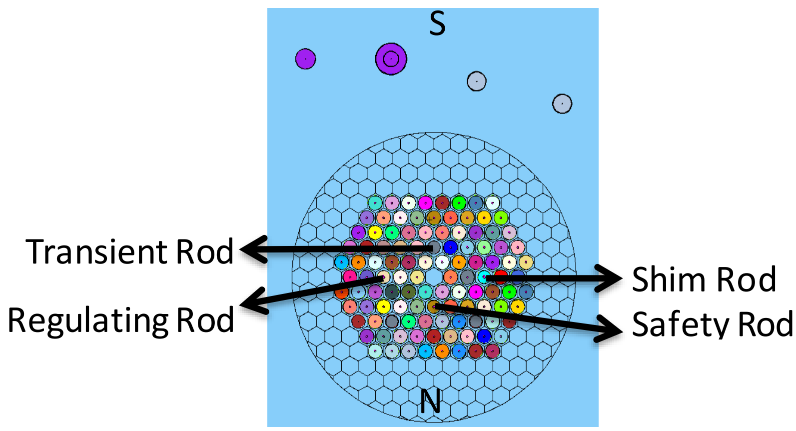

Figure 6-14. Control rod locations compared to the reactor core and ex-core detectors

In Figure 6-13, when the control rods are even, flux distribution is close to the reactor core center. Once the safety rod is withdrawn from the core and the transient rod is inserted, flux is shifted away from the ex-core detectors to the south region. After two rods` asymmetrical insertion and withdrawal are implemented, flux is shifted to the southwest corner. Actual reactor power must be higher in these two cases due to the power shift and simulation and experimental results prove that in Figure 6-12.

A similar experiment is done at the R1 open pool location and the results of the experiment are used to develop simulation conditions. Figure 6-15 shows the estimated reactor power for both simulation and experimental results for the miniature fission chamber along with ex-core detector simulations.

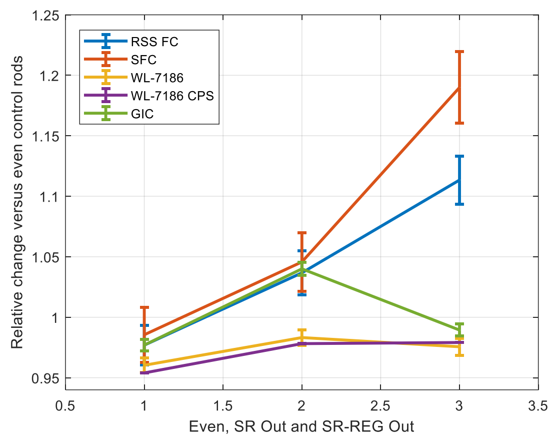

Figure 6-15. Estimated Power versus asymmetrical control rod insertion for ex-core detectors, miniature fission chamber by MCNP simulation, and experimental results from miniature fission chamber shown as CPS at R1 open pool

A similar trend with a smaller scale was observed with R1 open pool simulation and experiment results. This is expected since the neutron flux shifts more towards the D_2O tank location which is explained in previous chapters. Miniature fission chamber counts per second values are also higher in the D_2O tank location, which also proves that in normal operation and the asymmetrical insertion, the D_2O tank has higher power than the R1 location.

This chapter proves that the asymmetrical insertion and withdrawal have a significant effect on ex-core detectors and actual reactor power is changing with it. This inaccuracy needs to be corrected for future experiments since the reactor console always shows the same reactor power. The results also show that the core locality effect on detector responses needs to be corrected as well.

6.5 Control rod position change effect on each detector R1, D_2O tank, FNI, and FFT

After low power measurements, the WL-7186 detector is removed from the reactor core since it is not operable under high neutron flux. The second part of the experiment focuses on recording the ex-core detector power data, fuel temperature, and the control rod position in 100, 250, 500, 750, and 1000 kW at the R1 open pool, D_2O tank, FNI, and FFT from the reactor console. Measurements are taken when reactor power is steady-state and are shown in Table 6-7 for the R1 open pool.

Table 6-7. High power measurements for ex-core detectors at R1 open pool

RSS FC Power (kW)	SFC Power (kW)	GIC Power (kW)	TR Position (inches)	SF Position (inches)	SH Position (inches)	REG Position (inches)	Temperature (°C)
99.50	86.96	114.48	9.66	9.65	9.65	9.65	146.3
249.27	228.73	254.88	10.31	10.31	10.31	10.31	262.3
500.26	477.89	486.83	11.25	11.24	11.24	11.24	360.7
750.15	723.30	734.50	12.13	12.12	12.12	12.12	448.0
998.44	998.44	984.44	13.06	13.03	13.03	13.03	516.0

These measurements are important for the research since the control rod positions obtained in the experiment will be used as simulation inputs for MCNP. RSS fission chamber values are averaged from the excel spreadsheet generated by the console data historian. In this method, when steady-state reactor power is achieved, reactor powers are summed for every second, and the average power level is obtained. The spare fission chamber was not calibrated during the experiment. The power shown in the reactor console was about 4 times less than in the RSS fission chamber. For this reason, a linear calibration was applied to the spare fission chamber assuming the full power value is equal to the RSS FC data. In addition, D_2O tank FNI and FFT data are taken at the same power levels for the detectors and the control rods. Table 6-8 through Table 6-10 show the results.

Table 6-8. High power measurements for ex-core detectors at the D_2O tank

RSS FC Power (kW)	SFC Power (kW)	GIC Power (kW)	TR Position (inches)	SF Position (inches)	SH Position (inches)	REG Position (inches)	Temp. (°C)
99.69	89.73	102.46	8.89	8.89	8.89	8.89	126.8
250.15	236.01	251.23	9.50	9.51	9.51	9.51	235.0
497.89	470.91	499.05	10.31	10.33	10.33	10.33	361.8
749.05	729.35	748.06	11.06	11.08	11.08	11.08	445.1
1006.78	1006.78	1002.8	11.78	11.79	11.79	11.79	518.2

Table 6-9. High power measurements for ex-core detectors at the FNI

RSS FC Power (kW)	SFC Power (kW)	GIC Power (kW)	TR Position (inches)	SF Position (inches)	SH Position (inches)	REG Position (inches)	Temp. (°C)
0.001	0.0005	3.47	9.22	9.20	9.20	9.21	26.7
99.88	88.96	84.38	9.77	9.77	9.77	9.77	146.9
250.66	234.00	214.10	10.41	10.39	10.39	10.40	260.7
499.93	477.77	445.18	11.34	11.34	11.34	11.33	363.4
752.21	723.13	697.66	12.21	12.20	12.21	12.21	447.5
998.20	998.20	970.61	13.13	13.11	13.09	13.10	515.0

Table 6-10. High power measurements for ex-core detectors at the FFT

RSS FC Power (kW)	SFC Power (kW)	GIC Power (kW)	TR Position (inches)	SF Position (inches)	SH Position (inches)	REG Position (inches)	Temp. (°C)
0.001	0.0005	7.13	9.19	9.20	9.20	9.20	30.1
99.93	89.591	86.76	9.74	9.74	9.74	9.74	148.5
250.14	230.28	216.14	10.37	10.38	10.38	10.38	260.8
502.10	481.13	447.56	11.32	11.32	11.32	11.32	363.6
755.02	745.19	694.77	12.17	12.18	12.19	12.19	448.3
1005.23	1005.23	965.41	13.11	13.09	13.11	13.10	515.2

The results from Table 6-7 through Table 6-10 show the detector responses and control rod positions. Detector responses vary between the core localities and control rod positions. The gamma ion chamber shows the highest results near the D_2O tank and other locations follow. The spare fission chamber shows less power output than the RSS fission chamber. Finally, the RSS fission chamber detector indicators show varying results between core localities.

These results are used to develop input files for the MCNP simulations. Temperature and the control rod positions data are implemented into the MCNP and Serpent input files to simulate

FMESH and Fission Matrix Methods, which will be used to calculate detector responses. In addition, the control rod position change effect compared to experimental and simulation results in section 7.3.1

6.6 Asymmetric Control Rod Insertion and Withdrawal by Transient and Safety Rod at D_2O Tank and R1 Open pool

After high power measurements, reactor power is dropped to 500 kW for the D_2O tank and R1 open pool location. The goal in this section is similar to low power asymmetric insertion, removing the safety rod by 2 inches and inserting the transient rod by 2 inches at high power this time. Due to limited time, only the safety rod is removed and the transient rod is inserted, but other configurations can be simulated by MCNP. Table 6-11 shows the reactor power, detector results, temperature, and the control rod positions for the R1 open pool and D_2O tank where transient and safety rod is asymmetrically inserted and withdrawn from the reactor core at 500 kW, respectively.

Table 6-11. Asymmetrical rod insertion and withdrawal at 500 kW for R1 open pool and the D_2O tank

Core Location	RSS FC Power (kW)	Spare FC Log Power	GIC Power (kW)	TR Pos. (inches)	SF Pos. (inches)	SH Pos. (inches)	REG Pos. (inches)	Temp. (°C)
R1 Even	500.26	477.21	486.83	11.25	11.24	11.24	11.24	360.7
R1 Asymmetrical	502.41	466.34	509.71	9.24	13.26	11.57	11.52	366.9
D_2O Even	497.89	470.21	499.05	10.31	10.33	10.33	10.33	361.8
D_2O Asymmetrical	503.81	481.16	515.29	8.31	12.32	10.50	10.51	365.4

According to Table 6-11, D_2O tank results show higher indicated power for the RSS fission chamber, spare fission chamber, and the gamma ion chamber in an asymmetrical control rod movement compared to R1 location asymmetry. The control rod positions in this experiment were used to develop asymmetrical comparison by the MCNP. In section 7.3.2, high power asymmetrical rod movement is compared for simulation and experimental results.

Chapter 7

Correction of the Detectors using Detector Responses

The previous chapters described how the detector and core are modeled into MCNP, and what types of methods are used to calculate tally results for the detectors with different operational parameters. Detector response functions can be calculated by running several simulations for each fuel element and calculating how those operational parameters contribute to the detector tally results. Detector response functions can be found by running fixed source calculations which are described in Chapter 4 and Chapter 5. Detector response functions are multiplied with source calculations to estimate detector responses in Chapter 5. In this chapter, correction of the ex-core detectors will be done using the detector responses developed in this thesis.

7.1 Correction of the Detectors for Different Core Locality and Control Rod Position

Chapter 5 proved the effect of the core locality and control rod position change over detector responses. Inserting the control rods increased the reaction rate per source particle in the detector region by the FMESH method. Similarly, an investigation was done at various experimental locations. The D_2O position had the lowest reaction rate per source particle among the other core localities. Which is followed by R1 open pool, FFT, and FNI with different trends depending on the detector.

In this section, a combination of the core locality and control rod position effect will be investigated and a detector response will be created for each detector using various reactor power data calculated by the FMESH method.

7.1.1 RSS Fission Chamber Detector Correction

FMESH method is used to determine detector responses for all four core localities using rod positions corresponding to seven reactor power levels which are also shown in Figure 5-30. These powers are 0.001, 100, 250, 500, 750, 1000 kW. In addition to these power levels, the all rods out case was also investigated. Figure 7-1 shows the FMESH detector responses in reaction rate per source particle for all core localities and reactor powers mentioned above.

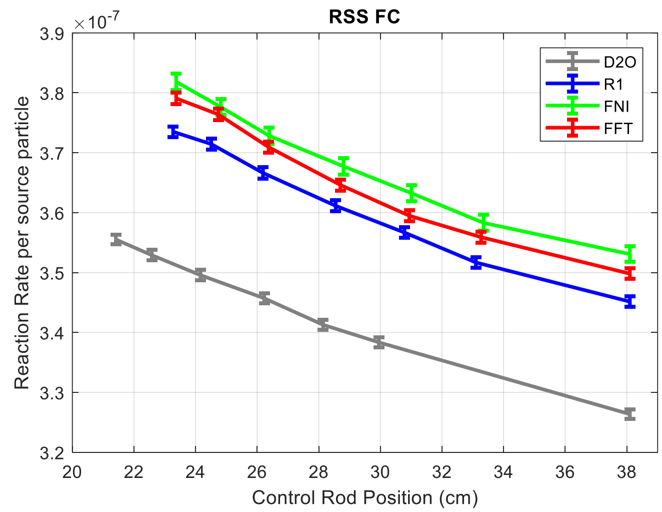

Figure 7-1. FMESH detector responses for core localities and different control rod positions for RSS fission chamber

The percent changes are shown in Table 5-8 for various detectors and core localities used in this section. During normal operation, reactor power does not exceed 1000 kW. For this reason, when calculating the detector responses, the 1 W versus 1000 kW case will be used.

Since thermal power calibration is done near the D_2O tank and detectors are calibrated at that position, simulation results should also be taken with the D_2O tank as a reference. 1000 kW reactor power is taken as a reference at the D_2O tank and other power levels are corrected using linear regression. Assuming reaction rate per source particle at P_X kW reactor console power is X and at 1000 kW is Y, corrected power at P_X kW would be :

$$P_{X-Corrected} = \frac{{P_X}^2}{\frac{X \times P_X}{Y \times 1000} X1000}$$

Figure 7-2 shows the corrected reactor power using the FMESH method for the RSS fission chamber using four different core localities.

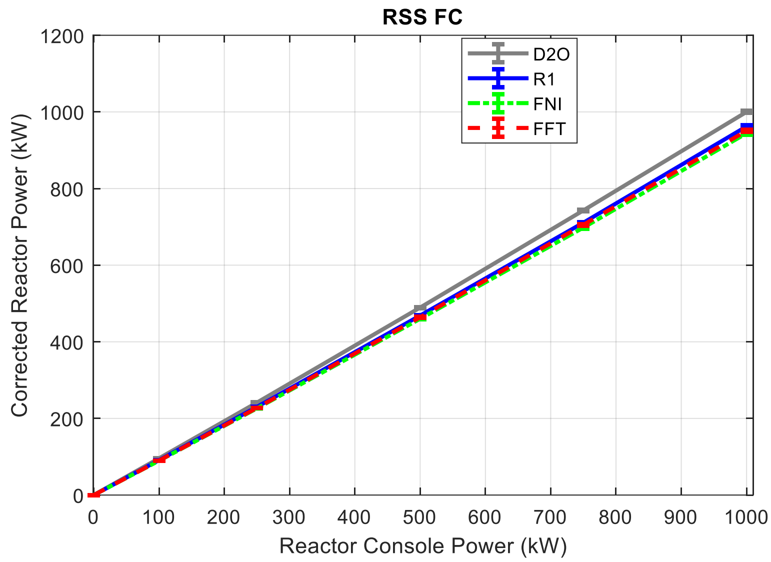

Figure 7-2. Reactor console power reading versus corrected reactor power using FMESH method for the RSS fission chamber at four locations

Figure 7-2 shows the detector response corrections for the RSS fission chamber at four different core localities. The 1000 kW at D_2O tank FMESH result is assumed to be the base case for all powers and core localities. All FMESH results are corrected using this point.

After this, absolute and linear changes in reactor power at the D_2O tank were investigated for reactor console power versus corrected power. Figure 7-3 shows the absolute and relative difference between linear fitting and corrected power versus console power at the D_2O tank.

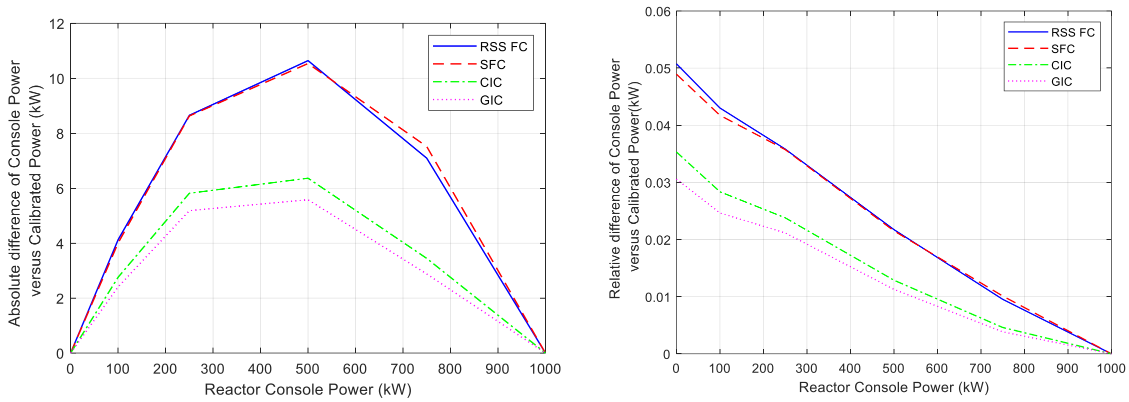

Figure 7-3. The absolute and relative difference of linear fitting and corrected power versus console power at the D_2O tank.

In the linear fitting approach, zero and 1000 kW power values are taken as a fixed point and linear fitting is performed. According to Figure 7-3, the absolute difference is higher in the middle power levels and the relative difference is higher in the low power section. For this reason, quadratic and cubic fitting were investigated. In this investigation, zero power and 1000 kW power were assumed constant, and fitting was applied for all data points by using the MATLAB default curve fitter. The cubic fitting has the lowest difference among all and is shown in Figure 7-4.

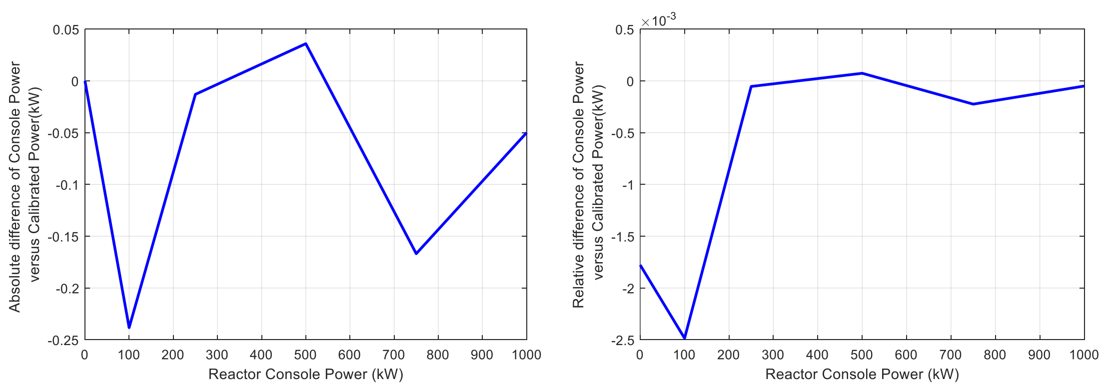

Figure 7-4. The absolute and relative difference of cubic fitting and corrected power versus console power at the D_2O tank.

For the rest of the analysis, cubic fitting is applied for all core localities and detectors. Table 7-1 shows the cubic fitting equations for all core localities and results.

Table 7-1. The cubic fitting equation for all core localities that is corrected using 1000 kW D_2O tank FMESH result for RSS fission chamber

Core Location	Cubic Fitting $y = ax^3 + bx^2 + cx$ a	b	c	100 kW	250 kW	500 kW	750 kW	1000 kW
D_2O	-1.526e-8	6.521e-5	0.9500	95.63	241.33	489.39	742.74	1000.00
R1	1.263e-9	5.116e-5	0.9096	91.47	230.61	467.75	711.51	962.02
FNI	2.793e-9	4.653e-5	0.8950	89.97	226.70	459.48	698.60	944.32
FFT	-2.691e-8	8.691e-5	0.8907	89.91	227.69	463.71	705.55	950.70

Table 7-1 shows the corrected power and how different the results are with varied core localities. At full power, the actual reactor power should be 962.02, 944.32, and 950.70 kW for R1, FNI, and FFT, respectively. These cubic fitting equations may be used to estimate corrected power at all localities using the RSS fission chamber. If an experimenter did an experiment where reactor console power is 600 kW at the R1 open pool, the true power that should be used in their research is calculated by the cubic fitting as 564.45 kW.

7.1.1.1 Spare Fission Chamber Detector Correction

Similar to the RSS fission chamber, core locality and control rod change affect data used to correct the spare fission chamber detector response. Figure 7-5 shows the FMESH detector responses for all core localities with different control rod positions for the spare fission chamber.

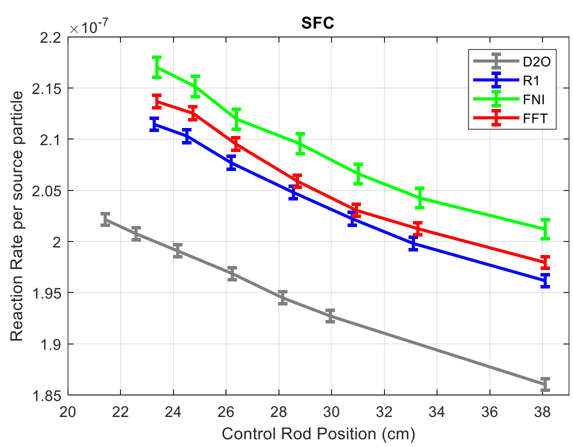

Figure 7-5. FMESH detector responses for core localities and different control rod positions for spare fission chamber

Detector responses were corrected in a similar approach in the previous section. Figure 7-6 shows the corrected reactor power versus the console power for all core localities using the spare fission chamber.

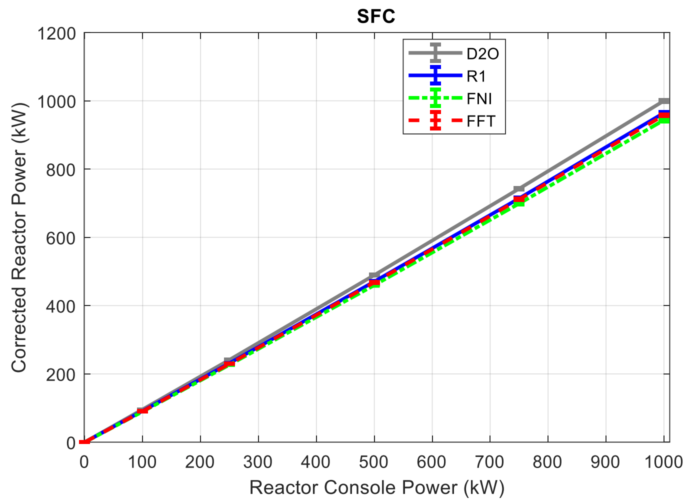

Figure 7-6. Reactor console power reading versus corrected reactor power using FMESH method for the spare fission chamber at four locations

A similar cubic fitting was applied to the spare fission chamber. Cubic fitting plotted for each core locality and equation is shown in Table 7-2. Corrected reactor powers are also listed for given reactor console power.

Table 7-2. The cubic fitting equation for all core localities that is corrected using 1000 kW D_2O tank FMESH result for spare fission chamber

Core Location	**Cubic Fitting $y = ax^3 + bx^2 + cx$** a	b	c	**100 kW**	**250 kW**	**500 kW**	**750 kW**	**1000 kW**
D_2O	-1.063e-8	5.852e-5	0.9521	95.78	241.52	489.35	742.51	1000.00
R1	-6.445e-9	5.831e-5	0.9126	91.84	231.69	470.07	714.53	964.46
FNI	-6.644e-9	5.758e-5	0.8926	89.83	226.65	459.86	699.03	943.53
FFT	-3.263e-8	9.308e-5	0.8971	90.61	229.58	467.74	711.42	957.55

The correction of the spare fission chamber and RSS fission chamber shows the results are between $\pm 5\ kW$. This demonstrates that the same type of detectors are affected similarly by the core locality and the control rod movement.

7.1.1.2 Compensated Ion Chamber Detector Correction

The same procedure was followed for the compensated ion chamber to obtain detector response. Figure 7-7 and Figure 7-8 show the FMESH detector responses for all core localities with different control rod positions for the compensated ion chamber and corrected reactor power versus the reactor console power for all core localities.

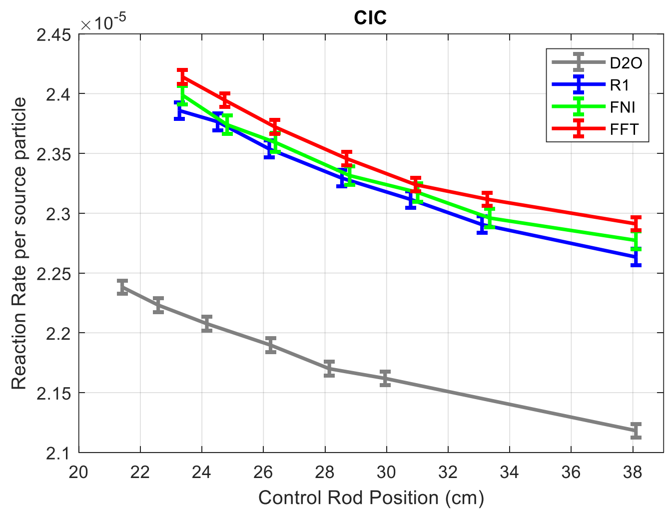

Figure 7-7. FMESH detector responses for core localities and different control rod positions for compensated ion chamber

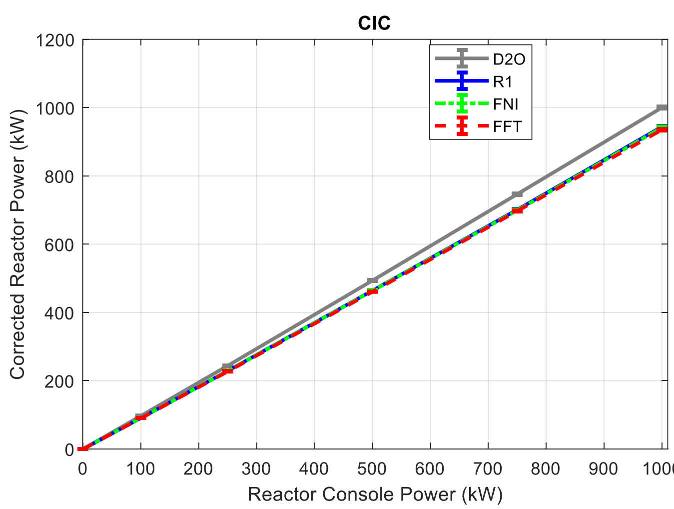

Figure 7-8. Reactor console power reading versus corrected reactor power using FMESH method for the compensated ion chamber at four locations

According to Figure 7-8; R1, FNI, and FFT corrections are very close to each other due to their small variations in FMESH result. Table 7-3 shows the cubic fitting equations for the compensated ion chamber response for all core localities and corrected reactor powers versus the console power.

Table 7-3. The cubic fitting equation for all core localities that is corrected using 1000 kW D_2O tank FMESH result for compensated ion chamber

Core Location	Cubic Fitting $y = ax^3 + bx^2 + cx$ a	b	c	100 kW	250 kW	500 kW	750 kW	1000 kW
D_2O	-2.327e-8	6.003e-5	0.9632	96.90	244.19	493.69	746.35	1000.00
R1	-5.558e-10	3.492e-5	0.9094	91.29	229.52	463.36	701.46	943.76
FNI	1.319e-9	3.065e-5	0.9095	91.25	229.31	462.58	699.92	941.46
FFT	-2.345e-8	6.31e-5	0.8955	90.16	227.45	460.59	697.22	935.15

The corrected powers for the compensated ion chamber are less than the RSS fission chamber and spare fission chamber powers. Having an experimental fixture such as FNI and FFT near the reactor core has minimal effect on compensated ion chamber. One reason could be the distance of the compensated ion chamber to the reactor periphery. It is two centimeters further away from the reactor periphery compared to the RSS fission chamber. Another explanation might be that the interaction happens inside the compensated ion chamber. ^{10}B has a high (n, alpha) reaction cross-section along the entire neutron energy spectrum, which means a contribution of the fast neutrons is still possible with the change of core locality. A single detector response may be used for these three core localities. Corrected power changes between R1, FNI, and FFT are about eight kW and it drops when reactor power is lower.

7.1.1.3 Gamma Ion Chamber Detector Correction

Similar to the other detectors, core locality and control rod change affect data used to correct gamma ion chamber detector response. Figure 7-9 shows the FMESH detector responses for all core localities with different control rod positions for the gamma ion chamber and Figure 7-10 shows the corrected reactor power versus reactor console power for all core localities.

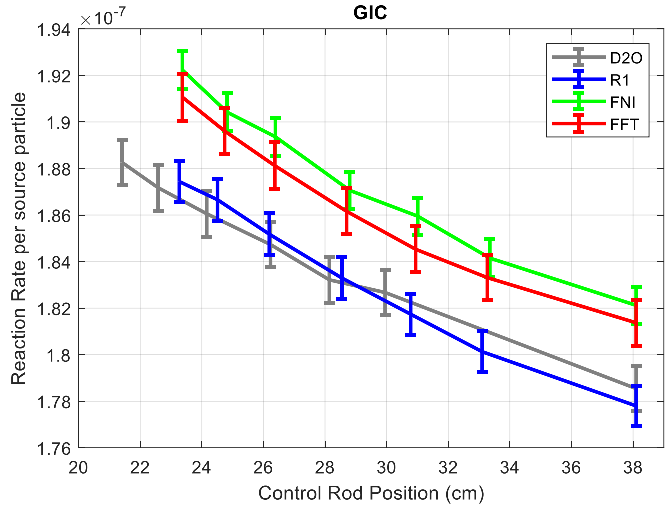

Figure 7-9. FMESH detector responses for core localities and different control rod positions for gamma ion chamber

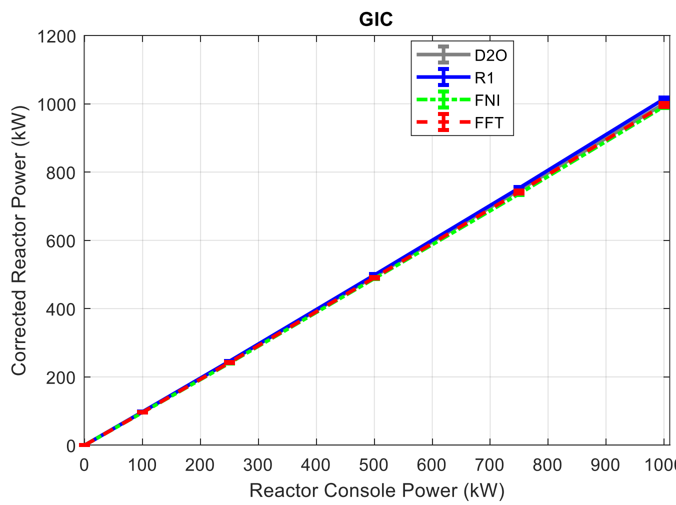

Figure 7-10. Reactor console power reading versus corrected reactor power using FMESH method for the gamma ion chamber at four locations

There is minimal change observed in detector responses in the gamma ion chamber. D_2O and R1 have close corrected power results. The FNI and FFT also have close corrected reactor power calculations. Table 7-4 shows the cubic fitting applied to the gamma ion chamber response for each core locality and compared with console power.

Table 7-4. The cubic fitting equation for all core localities that is corrected using 1000 kW D_2O tank FMESH result for gamma ion chamber

Core Location	Cubic Fitting $y = ax^3 + bx^2 + cx$ a	b	c	100 kW	250 kW	500 kW	750 kW	1000 kW
D_2O	-2.236e-8	5.550e-5	0.9668	97.21	244.82	494.48	746.88	1000.00
R1	-2.311e-9	4.066e-5	0.9757	97.97	246.43	497.72	753.67	1014.01
FNI	3.127e-9	3.066e-5	0.9581	96.12	241.49	487.11	737.14	991.88
FFT	-1.456e-8	5.374e-5	0.9573	96.25	242.45	490.26	742.06	996.48

The difference between R1and D_2O versus FNI and FFT was explained before by having lead fixtures around the FNI and FFT. Uncertainties and associated results with the FMESH method are very close between R1 and D_2O and FNI, and FFT. For this reason, a single correction may be used for both locations. According to Figure 7-9, D_2O and R1 locations results are inside the uncertainty bands, thus results in Table 7-4 do not represent any violation of power limits.

The cubic fitting equations for each detector and each core locality can be used for future reactor power calculations. When the reactor console power reading is “x”, corrected power “y” can be easily found using cubic fitting equations provided in Table 7-1 through Table 7-4 depending on the core locality and the detector.

7.2 Asymmetric Control Rod Insertion and Withdrawal Detector Response Correction

This section focuses on detector response correction for asymmetrical control rod insertion and withdrawal. Chapter 5 proved the significant effect of asymmetrical insertion and withdrawal over the detectors at high power using various core locations. Chapter 6 proved the asymmetric insertion and withdrawal effect on detector response with the aid of experiments and simulations. These effects will be investigated in this chapter and detector responses will be corrected for asymmetrical control rod movement.

7.2.1 Low Power Asymmetric Insertion and Withdrawal Experimental versus Simulation Detector Response Correction

Chapter 6 showed the experiment performed at the PSBR by placing the WL-7186 miniature fission chamber when the reactor power is at 1 W. Results proved that the insertion and withdrawal of control rods asymmetrically changes the neutron flux profile inside the reactor core. Since reactor power is measured by the ex-core detectors, depending on the location of the power shift, true reactor power would be different in asymmetrical insertion. The ex-core detectors always show 1 W for all cases in the reactor console, but true power would be different due to the power shift caused by the asymmetrical control rod movement.

After the experiment was done with asymmetrical control rod movement, control rod positions were recorded and simulations were done using experimental data for ex-core detectors and the WL-7186 miniature fission chamber. Figure 6-12 and Figure 6-15 show the computational results for those detectors and experimental detector counts per second. These figures prove that the neutron flux shift affects the detectors differently due to their locality. Experimental counts per second for the WL-7186 match with computational results. The ex-core detectors have different responses which also proves the reactor power is significantly different compared to the reactor console power readings. Table 7-5 shows the percent changes of the detectors by the asymmetrical control rod movement at the D_2O tank.

Table 7-5. Experimental and simulation comparison of the detector responses at the D_2O tank

	Even Control Rods	TR in – SF out	TR and SH in - SF and REG out
RSS FC	1	1.0685	1.1934
SFC	1	1.0865	1.3439
GIC	1	1.0803	1.0106
WL-7186 (Experiment)	1	1.0113	1.0123
WL-7186 (Simulation)	1	1.0099	1.0116

Similar to this, percent changes of the detectors by asymmetrical control rod movement for R1 open pool location are shown in Table 7-6.

Table 7-6. Experimental and simulation comparison of the detector responses at R1 open pool

	Even Control Rods	TR in – SF out	TR and SH in - SF and REG out
RSS FC	0.9769	1.0367	1.1134
SFC	0.9855	1.0457	1.1899
GIC	0.9770	1.0401	0.9894
WL-7186 (Experiment)	0.9540	0.9782	0.9791
WL-7186 (Simulation)	0.9603	0.9832	0.9756

Since the spare fission chamber is located at the corner of the reactor core, it is affected more by asymmetrical insertions. The WL-7186 experimental and simulation results show the effect of the asymmetrical insertion. However, in the center of the core, this detector is affected less compared to the ex-core detectors.

Correction of power can be done using any detector. Due to their locality, they are affected differently, thus corrected reactor power would be different for each case. The correction also depends on the asymmetry type and also which control rods are inserted and withdrawn. This makes estimating true reactor power in asymmetrical conditions challenging. With similar asymmetrical insertion at low power, reactor power changed about six percent for the D_2O tank, and four percent for the R1 open pool.

In the future, these corrections can be used for asymmetrical insertion since the configuration done at the experiment is the most conservative asymmetrical insertion. It has the maximum possible asymmetrical control rod movement that PSBR is capable of. However, the asymmetrical insertion difference from this configuration needs to be re-evaluated and modeled into MCNP using the FMESH method. For multiple calculations, the Fission Matrix Method can be used for faster simulations.

7.2.2 High Power Asymmetric Insertion and Withdrawal Detector Response Correction

High power asymmetrical control rod movement is shown in Section 5.3 and Section 5.4.3. In these sections, an investigation is done at all core localities at 500 kW reactor power. Asymmetry is established by two rods: first transient rod versus safety rod and then shim rod and regulating rod. In each case, when the first rod is inserted, the opposite-side control rod is withdrawn from the reactor core and the opposite insertion and withdrawal are also simulated.

Similar to Section 7.1, the D_2O tank 500 kW simulation is assumed as the base case, and calculations were performed to estimate reactor power for other core localities and with the asymmetrical control rod movement. Table 7-7 shows the asymmetrical control rod corrected powers for the RSS fission chamber for all core localities.

Table 7-7. Asymmetrical control rod corrected powers for the RSS fission chamber for all core localities

	500 kW	TR in SF out	SF in TR out	SH in REG out	REG in SH out
D_2O	489.39	509.40	475.12	497.58	482.07
R1	467.75	483.21	456.83	475.49	463.34
FNI	459.48	471.04	447.76	463.23	453.11
FFT	463.71	474.74	450.15	468.01	456.15

Because the RSS fission chamber is located near the transient rod, insertion of the transient rod causes the neutron flux to shift away from the RSS fission chamber, thus true power should be higher than shown power. In addition, the RSS fission chamber is also located close to the center of the reactor core; shim and regulating rod insertion and withdrawal do not significantly change the FMESH results for the RSS fission chamber. The power is changed about $\pm 20\ kW$ for the transient and safety rod asymmetry, $\pm 9\ kW$ for the shim and regulating rod asymmetry.

Similar to the RSS fission chamber, the spare fission chamber's asymmetrical insertion and withdrawal for all control rods are investigated and the results are shown in Table 7-8.

Table 7-8. Asymmetrical control rod corrected powers for the spare fission chamber for all core localities

	500 kW	TR in SF out	SF in TR out	SH in REG out	REG in SH out
D_2O	489.35	504.23	478.12	510.32	472.89
R1	470.07	481.62	460.60	488.53	457.09
FNI	459.86	469.75	450.65	473.67	446.58
FFT	467.74	475.89	456.48	481.06	452.11

In the previous chapter, it is shown that the transient and safety rod asymmetrical movement causes similar changes for all ex-core detectors since these movements to shift the neutron flux to the south or the north part of the reactor core. However, asymmetrical movement of the shim and regulating rod has a different effect on the detectors due to neutron flux shifts to the east and west, thus changing detector responses, especially for the detectors located at the corner of the reactor core. The power is changed about $\pm 15\ kW$ for the transient and safety rod asymmetry, $\pm 21\ kW$ for the shim and regulating rod asymmetry which is very different from than RSS fission chamber.

In addition, compensated ion chamber asymmetrical insertion and withdrawal were also investigated for the two different configurations, and the results are shown in Table 7-9.

Table 7-9. Asymmetrical control rod corrected powers for the compensated ion chamber for all core localities

	500 kW	TR in SF out	SF in TR out	SH in REG out	REG in SH out
D_2O	493.69	514.78	477.23	487.17	498.19
R1	463.36	479.03	449.99	458.19	469.28
FNI	462.58	473.77	448.50	454.82	465.95
FFT	460.59	473.01	445.76	454.49	464.15

The power is changed about $\pm 19\ kW$ for the transient and safety rod asymmetry, $\pm 8\ kW$ for the shim and regulating rod asymmetry. These differences are very close to the RSS fission chamber results. This is expected since both detectors are located at the same distance to the center of the core where the RSS fission chamber is located in the west and compensated ion chamber is located in the east. For this reason, shim and regulating rod asymmetry results are flipped for these two detectors.

Finally, the gamma ion chamber asymmetrical insertion and withdrawal of the control rods were investigated, and the results are shown in Table 7-10.

Table 7-10. Asymmetrical control rod corrected powers for the gamma ion chamber for all core localities

	500 kW	TR in SF out	SF in TR out	SH in REG out	REG in SH out
D_2O	494.48	508.86	483.54	483.38	506.15
R1	497.72	509.05	487.25	487.71	509.71
FNI	487.11	494.51	476.34	475.84	495.75
FFT	490.26	498.73	478.64	480.10	499.82

The power is changed about $\pm 15\ kW$ for the transient and safety rod asymmetry, $\pm 12\ kW$ for the shim and regulating rod asymmetry. These differences are very close to the spare fission chamber results. This is expected since both detectors are located at the same distance to the center of the core where the spare fission chamber is located in the west corner and the gamma ion chamber is located in the east corner. For this reason, shim and regulating rod asymmetry results are opposite for these two detectors.

The results in this section show the correction of the reactor power using the created detector response functions. Effects of the asymmetry over ex-core detectors are different due to the location of the detectors and the distance between control rods and detectors.

The asymmetry of the control rods may be done in various configurations with a wide range of control rod insertion and withdrawal. This makes it harder to create a simple detector response for the asymmetrical control rod movement using the FMESH method since fission source distribution has to be created for each calculation. On the other hand, the Fission Matrix Method could be used for each configuration since this method requires less computational time and has proven to be given similar results to the FMESH method.

7.3 Comparison of Experiment and Simulations

In this section, a comparison of the experimental results in Chapter 6 for high power control rod movement and asymmetrical control rod movement effect compared with the MCNP simulations.

7.3.1 High Power Control Rod Movement Effect with Core Locality

The high power reactor operation and high power asymmetrical insertion and withdrawal data are used to develop the FMESH method using MCNP. The control rod positions for the corresponding power are taken from the control console. A script was created to read all the variables from the control console, translate them into an MCNP input file, and run the computational simulation. Some results are shown in the previous chapter in high power computational analysis and these results will be used to develop detector response correction.

Figure 7-11 shows the relative percent difference change between the SFC versus the RSS FC and GIC versus the RSS FC for each reactor power and core locality and for both experimental and simulations.

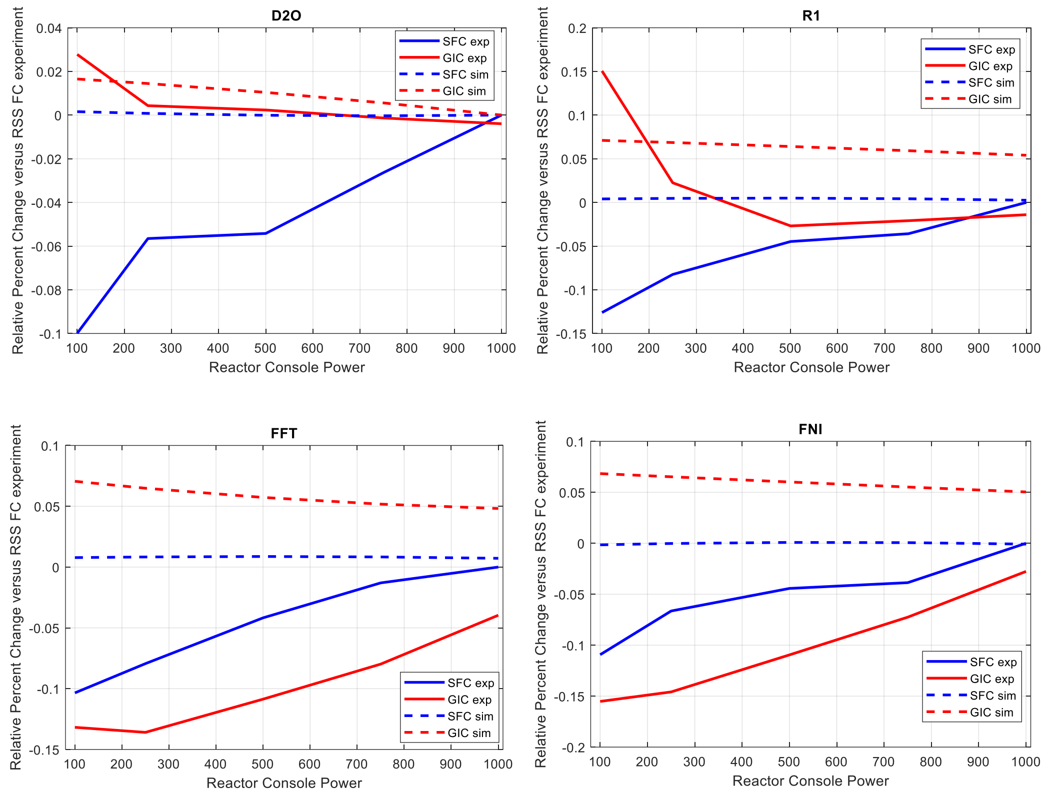

Figure 7-11. RSS FC and GIC high power relative differences for each power and core locality

According to Figure 7-11 at low powers, the detectors have a very high difference from each other. This difference is reduced when power is increased, especially for the experimental results. The results also show simulations have a consistent trend over all power ranges for each detector. The main reason for the high change in experimental results may be due to the RSS fission chamber data being averaged for about 10 minutes of data while the GIC and SFC data is taken from a single data point by the experimenter. This introduces very high uncertainty to the experimental results since power is fluctuating in the reactor console indicator. Another contributing factor is that the SFC was not calibrated during the experiment. Calibration with linear fitting applied for spare fission chamber using full power value. For this reason, SFC data varies from RSS FC, especially at low powers. The GIC operates in the power range, and due to fission products, effects of delayed gamma rays, and calibration being done at high power, GIC is not a suitable detector at low power.

7.3.2 High Power Asymmetrical Control Rod Movement

Similar to the previous section, experimental values of control rod positions were used to create the MCNP simulation for the high power asymmetrical control rod movement. Table 7-11 shows the high power asymmetrical control rod movement data for R1 open pool and D_2O tank location incorporated with experiments and simulations.

Table 7-11. High power asymmetrical control rod movement data for both R1 and D_2O tank locations, comparing experiment and simulations

	Core Location	RSS FC Power (kW)	Spare FC Power (kW)	GIC Power (kW)	TR Position (inches)	SF Position (inches)	SH Position (inches)	REG Position (inches)	Temperature (℃)
Experiment	R1 Even	500.26	477.21	486.83	11.25	11.24	11.24	11.24	360.7
	R1 Asymmetrical	502.41	466.34	509.71	9.24	13.26	11.57	11.52	366.9
	D_2O Even	497.89	470.21	499.05	10.31	10.33	10.33	10.33	361.8
	D_2O Asymmetrical	503.81	481.16	515.29	8.31	12.32	10.50	10.51	365.4
Simulation	R1 Even	467.75	470.07	497.72	9.24	13.26	11.53	11.53	N/A
	R1 Asymmetrical	483.21	481.62	509.05	9.24	13.26	11.53	11.53	N/A
	D_2O Even	489.39	489.35	494.48	8.31	12.32	10.50	10.50	N/A
	D_2O Asymmetrical	509.40	504.23	508.86	8.31	12.32	10.50	10.50	N/A

Table 7-11 data is used to make a comparison between experimental results and simulations for each detector. RSS fission chamber results are compared with the spare fission chamber and gamma ion chamber results. Figure 7-12 shows the comparison of the D_2O tank and R1 location high power asymmetrical control rod movement results for spare fission chamber and gamma ion chamber with respect to RSS fission chamber where case 1 is even rods and case 2 is asymmetrical control rod movement case.

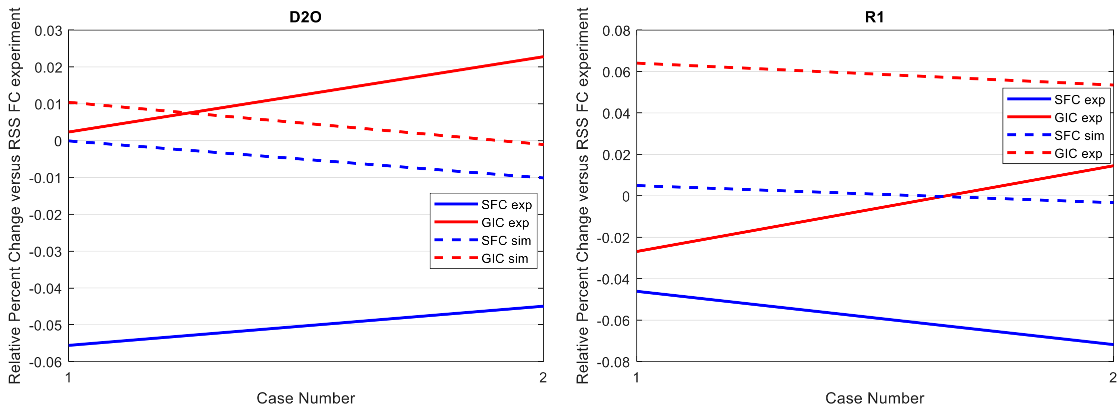

Figure 7-12. Comparison of the D_2O tank and R1 location high power asymmetrical control rod movement results for spare fission chamber and gamma ion chamber with respect to RSS fission chamber where case 1 is even rods and case 2 is asymmetrical control rod movement case

Once more, the simulation results show a linear trend in both cases and a decreasing trend in SFC and GIC compared to the RSS FC. Experimental results show different behaviors of the detectors and it is not possible to make any conclusion about them. The difference in experimental data is explained in the previous section. It is found that after this experiment, the console data historian recordings of the detectors have very high uncertainties. Reactor staff will update the historian logic to reduce uncertainties and data will be more useful in future experiments.

Chapter 8

Implementing the Detector Response Corrections to the Logbook Computer at PSBR and Implications on Fuel Burnup

Chapter 7 showed the detector response calculations for the power correction. Each detector has a different correction factor that should be incorporated with the real console readings. This can be done by updating the reactor power values shown in the control console. This implementation is not possible at the moment since a more detailed investigation is required to update this method on the reactor control system.

For now, this method can be implemented into a logbook computer. The PSBR control console is equipped with a laptop that contains all the reactor operation data such as control rod positions, indicated reactor powers from the detectors, fuel temperatures, and other data as well. All of this information is recorded in an Excel spreadsheet in every reactor operation. Figure 8-1 and Figure 8-2 show the interface of the Excel spreadsheet created to record important reactor operation parameters in the PSBR control console.

	DATE	TIME	Core Loading	CRP (Y or N)	Powe Setpoint [kW]	Location in Pool	WIDE RANGE RSS LCD RSS [%]	WIDE RANGE RSS LOG [MW]	WIDE RANGE DCC-X DIG [kW]	WIDE RANGE DCC-Z Spare Log [dec]	WIDE RANGE DCC-Z Spare SQRT [$\%^{1/2}$]	POWER RANGE RSS LCD [%]	POWER RANGE DCC-X DIG [kW]	POWER RANGE DCC-Z Spare GIC [kW]	CIC DCC-Z Spare CIC [kW]	FUEL TEMPERATURE RSS 1 [°C]	FUEL TEMPERATURE RSS 2 [°C]	FUEL TEMPERATURE DCC-Z 1 [°C]	FUEL TEMPERATURE DCC-Z 2 [°C]	RBHVI ON NORMAL (Y or N)	Initials	Operator Comments
0050	5-May	1249	59	N	100	FNI	10	0.1	99.88	-1.620	0.140	12	103.75	84.38	95.60	140	150	134.2	146.9	Y	ZVH	Gokhan Data
0051	5-May	1258	59	N	250	FNI	25	0.25	250.66	-1.200	0.220	25	245.6	214.10	261.60	240	270	232.8	260.7	Y	ZVH	Gokhan Data
0052	5-May	1307	59	N	500	FNI	50	0.5	499.93	-0.890	0.310	49	478.77	445.18	507.30	340	370	325.0	363.4	Y	ZVH	Gokhan Data
0053	5-May	1316	59	N	750	FNI	75	0.7	752.21	-0.710	0.370	72	716.67	697.66	785.10	400	450	40.3	447.5	Y	ZVH	Gokhan Data
0054	5-May	1326	59	N	1000	FNI	99	0.9	993.2	-0.570	0.430	95	957.06	970.61	1083.20	480	510	466.0	515.0	Y	ZVH	Gokhan Data
0055	5-May	1352	59	N	0.001	FFT	0	1.00E-06	0	-6.850	0.000	2	15.85	7.13	0.20	30	30	30.3	30.1	Y	ZVH	Gokhan Data
0056	5-May	0001	59	N	100	FFT	10	0.09	99.93	-1.620	0.140	12	107.56	86.76	95.40	140	160	134.9	148.5	Y	ZVH	Gokhan Data
0057	5-May	1412	59	N	250	FFT	25	0.25	250.14	-1.210	0.220	26	248.9	216.14	242.00	220	270	232.6	260.8	Y	ZVH	Gokhan Data
0058	5-May	1422	59	N	500	FFT	50	0.5	502.1	-0.890	0.310	49	483.46	447.56	505.80	340	370	327.1	363.6	Y	ZVH	Gokhan Data
0059	5-May	1431	59	N	750	FFT	75	0.8	755.02	-0.700	0.370	72	751.52	694.77	788.00	400	450	405.1	448.3	Y	ZVH	Gokhan Data
0060	5-May	1441	59	N	1000	FFT	100	1	1005.23	-0.570	0.430	96	962.81	965.41	1096.00	480	510	466.4	515.2	Y	ZVH	Gokhan Data
0061	6-May	0837	59	N	900	FNI	90	0.9	903.2	-0.620	0.410	87	861.92	872.37	968.10	460	500	444.5	491.2	Y	THD	
0062	6-May	1048	59	N	900	FNI	90	0.9	898.26	-0.620	0.410	88	872.98	888.16	960.10	450	500	446.3	492.8	Y	THD	
0063	6-May	1409	59	n	200	R1	20	0.2	199.1	-0.700	0.190	21	200.23	176.07	189.50	220	230	209.5	230.7	Y	JAN	
0064	6-May	1527	59	n	200	R1	20	0.2	200.49	-1.310	0.190	21	202.96	177.43	188.50	220	240	211.4	232.2	y	SB	
0065	9-May	0859	59	Y	0.05	R1	0	4.00E-05	0.05	-5.270	0.000	0	0.27	-2.89	-0.80	25	25	20.8	20.4	Y	DB	CRP
0066	9-May	0929	59	N	0.25	FFT	0	2.00E-04	0.25	-4.670	0.010	0	0.54	-2.72	-0.50	25	25	21.4	21.0	Y	DB	
0067	9-May	1007	59	Y	750	R1	72	7.00E-01	750.1	-0.710	0.370	72	719.1	705.81	786.30	400	450	404.2	448.0	Y	DB	CRP
0068	9-May	1017	59	Y	1000	R1	100	1	1000.37	-0.570	0.430	97	963.08	976.79	1082.10	575	520	467.3	516.8	Y	DB	CRP
0069	9-May	1355	59	N	50	FFT	4	0.5	49.77	-1.990	0.090	6	47.27	36.00	42.60	90	90	80.2	87.1	Y	ZVH	
0070	12-May	1431	59	N	1	FFT	0.1	9.00E-04	1.01	-4.260	0.010	0	0.85	-2.55	0.20	30	30	26.0	24.3	Y	ZVH	
0071	12-May	1540	59	N	5	FFT	0.5	4.00E-03	5.04	-3.150	0.030	0	4.12	0.34	2.90	40	30	29.7	28.7	Y	ZVH	
0072	13-May	1018	59	N	200	R1	20	2.00E-01	202.36	-1.300	0.190	21	200.23	173.18	193.20	220	240	209.1	232.6	Y	JAN/ARP	

Figure 8-1. PSBR control console logbook computer sheet created by Excel, Part 1

DATE	TIME	Core Loading	CRP (Y or N)	Power Setpoint [kW]	Reactor Location in Pool	CONTROL ROD POSITIONS [1/100 inch]				TOTAL WORTH REMOVED [$]	POOL TEMP [°C]	GAMMA RADIATION					AIR PARTICULATE RADIATION		INITIALS	Operator Comments
						TR	SA	SH	RR			EAST BAY [mr/hr]	WEST BAY [mr/hr]	COBALT BAY [mr/hr]	NEUTRON BEAM LAB [mr/hr]	SOUTH BAY [mr/hr]	EAST [cpm]	WEST [cpm]		
5-May	1249	59	N	100	FNI	977	977	977	977	8.39	24.2	1.429	3.06	0.621	0.263	0.84	1418	1669	ZVH	Gokhan Data
5-May	1258	59	N	250	FNI	1041	1039	1039	1040	9.01	24.2	1.784	6.137	0.100	0.254	1.84	1478	1557	ZVH	Gokhan Data
5-May	1307	59	N	500	FNI	1134	1134	1134	1133	9.82	24.3	4.313	14.73	0.333	0.37	1.25	1244	1567	ZVH	Gokhan Data
5-May	1316	59	N	750	FNI	1221	1220	1221	1221	10.43	24.5	5.292	24.93	0.100	0.247	0.93	1372	1608	ZVH	Gokhan Data
5-May	1326	59	N	1000	FNI	1313	1311	1309	1310	10.90	25.0	6.421	36.06	0.502	0.291	1.56	1060	1780	ZVH	Gokhan Data
5-May	1352	59	N	0.001	FFT	919	920	920	920	7.78	25.4	0.505	0.1	0.100	0.3	1.05	1275	1373	ZVH	Gokhan Data
5-May	0001	59	N	100	FFT	974	974	974	974	8.35	25.4	1.699	2	0.152	0.513	1.15	1346	1560	ZVH	Gokhan Data
5-May	1412	59	N	250	FFT	1037	1038	1038	1038	9.00	25.5	1.955	3.6	0.371	0.511	0.83	1232	1366	ZVH	Gokhan Data
5-May	1422	59	N	500	FFT	1132	1132	1132	1132	9.80	25.5	4.813	8.642	0.122	0.344	0.10	1310	1325	ZVH	Gokhan Data
5-May	1431	59	N	750	FFT	1217	1218	1219	1219	10.41	25.6	6.668	11.25	0.753	0.481	1.06	1105	1283	ZVH	Gokhan Data
5-May	1441	59	N	1000	FFT	1311	1309	1311	1310	10.89	25.8	7.816	19.5	0.457	0.123	0.98	1632	1699	ZVH	Gokhan Data
6-May	0837	59	N	900	FNI	1303	1302	1302	1302	10.86	24.4	6.661	31.89	0.186	0.615	1.10	1544	1589	THD	
6-May	1048	59	N	900	FNI	1311	1311	1311	1311	10.90	21.4	6.528	31.25	0.533	0.483	1.02	1666	1939	THD	
6-May	1409	59	n	200	R1	1025	1029	1029	1029	8.89	21.1	1.748	1.79	0.339	0.223	1.38	1009	1137	JAN	
6-May	1527	59	n	200	R1	1026	1028	1027	1027	8.89	22.1	1.701	1.692	0.577	0.492	1.28	1043	877	SB	
9-May	0859	59	Y	0.05	R1	908	908	908	908	7.65	21.8	0.183	0.1	0.147	0.407	0.94	1671	1602	DB	CRP
9-May	0929	59	N	0.25	FFT	921	921	921	921	7.80	21.8	0.415	0.1	0.100	0.334	1.22	1659	1690	DB	
9-May	1007	59	Y	750	R1	1193	1193	1192	1192	10.25	22.1	6.339	7.1	0.100	0.366	3.90	1660	1698	DB	CRP
9-May	1017	59	Y	1000	R1	1278	1276	1276	1276	10.73	23.0	7.496	10.04	0.341	0.269	3.75	1624	1555	DB	CRP
9-May	1355	59	N	50	FFT	947	949	949	949	8.10	23.6	1.013	1.186	0.405	0.554	0.98	915	886	ZVH	
12-May	1431	59	N	1	FFT	920	921	921	921	7.80	22.5	0.397	0.2	0.343	0.1	0.63	1007	1000	ZVH	
12-May	1540	59	N	5	FFT	922	923	923	923	7.83	22.5	0.466	0.257	0.748	0.366	1.05	1188	1317	ZVH	
13-May	1018	59	N	200	R1	998	1000	1000	998	8.60	22.5	1.788	1.785	0.122	0.316	1.44	1147	1223	JAN/ARP	

Figure 8-2. PSBR control console logbook computer sheet created by Excel, Part 2

According to Figure 8-1 and Figure 8-2, reactor power readings are recorded in the Excel file by the reactor operator after ten minutes of steady-state reactor operation at the corresponding power level. This Excel spreadsheet is updated with the cubic equations calculated before for each core locality. For now, only the RSS fission chamber power correction is used since the main power indicator signal comes from this detector. Reactor powers which are column four in Figure 8-2 are multiplied with the functions for each core locality and corrected powers recorded. The corrected power calculated in the Excel spreadsheet may be used by the researchers.

A major source of uncertainty in the fuel burnup determination relates to uncertainty in reactor power measurements [52]. Fuel burnup calculations are done directly by the control console in PSBR. The newly developed control console contains an algorithm that reads linear power from the reactor safety system main power indicator, multiplies it with operation time, and calculates the fuel burnup at any time in MW-days. This block in the control console can be updated with newly developed detector responses and fuel burnup can be accurately estimated in the future.

For now, fuel burnup changes due to detector responses investigated using the logbook computer. One problem encountered here was, that operators only record the time when they take a measurement. For this reason, elapsed time cannot be calculated for some operations, and operation time is unknown for them. For proof of concept, a random time generator is implemented into the Excel spreadsheet. This random generator assigns one to five hours' operation time for each power level to show the difference between current burnup and newly calculated burnup by the corrected power just for the preliminary calculations. Both corrected power and console power are multiplied with these operational times to calculate burnup. The core loading 59 from June 8, 2020, through May 13, 2022, was investigated and burnups are shown in Table 8-1.

Table 8-1. Burnup comparison for the current method and corrected power with detector responses

	Burnup (MW-days)
Current Burnup from Logbook Laptop	79.24
Corrected Burnup with Detector Response	76.45

The results show that there is a 2.81 MW-days burnup difference between the two methods and about a 3.67% relative difference. This means the fuel burnup calculations can be done a 3.67% more efficiently by implementing the power correction method.

This method can be used in the future by correcting the timing which requires the operators need to enter the time when the reactor is steady and the end-time of the corresponding power level due to shut down or power setpoint change. Another way to calculate burnup is updating the current control system burnup calculation by implementing detector responses into the control console and using corrected power instead of console power.

This chapter proves that detector responses are very important for the true reactor power and burnup calculations. The method developed in this thesis could be used to estimate true reactor power and fuel burnup. Also, other TRIGA reactors can use a similar methodology to correct their power. This would increase their fuel utilization and gives better financial outcome.

Chapter 9

Conclusion and Future Work

9.1 Conclusion

To summarize, this thesis focuses on improving the accuracy of power measurement at the PSBR with the aid of computational methods using MCNP and Serpent 2. The PSBR MCNP model is edited to acquire faster computational results. Ex-core detectors; fission chambers, gamma ion chamber, and compensated ion chamber models were implemented into the PSBR MCNP Model. In addition, self-powered neutron detectors and a WL-7186 miniature fission chamber are modeled inside the PSBR MCNP model. To reduce uncertainties in the calculations, the ADVANTG automated weight window generator was used. For each core locality, a weight window file is created using ADVANTG. The weight window method reduced the uncertainties in the tally results and the FMESH method. Also, weight windows increased the figure of merit by a factor of 194 times for the RSS fission chamber.

MCNP modeling was done for neutron and photon transport with the desired physics model. Preliminary runs were completed for fission source distribution determination using MCNP KCODE calculations that utilize FMESH tallies and the Fission Matrix Method developed in Serpent 2. In addition to that, MCNP Surface Source Write (SSW) and Surface Source Read (SSR) methods are compared with the other fission source methods. Detector responses were investigated and compared to the different operation parameters: fuel temperature and control rod positions. All of these simulations produce a tremendous amount of data. To process the data and visualize the results, MATLAB® and BASH scripts were written. These scripts help create thousands of input files with a single command, run the simulations on the supercomputer, and finally process the data into the visible formats. The locality of the reactor core was investigated for the D_2O, R1 open pool, FNI, and FFT locations.

To see the importance of individual fuel element contribution to the detector responses, MCNP models were made using fixed source definitions for each fuel element. The results showed that the fuel elements closer to the detector region have a higher contribution to detector results, about 37% of the contribution comes from the first three fuel elements, and 51 % of the contribution comes from the first row of the fuel elements. The figure of merit of these calculations was also increased significantly by using ADVANTG automatic weight window generator. The individual fuel element contribution is later multiplied with the FMESH fission source to generate detector responses which are used throughout the thesis for various operating conditions.

The asymmetric control rod effect was investigated for the transient rod-safety rod, the shim rod-regulating rod asymmetrical insertion, and withdrawal. The results indicated that asymmetric control rod insertion creates neutron flux tilting around the reactor core and affects the detector responses. The RSS fission chamber, spare fission chamber and compensated ion chamber have about 4% change, and the gamma ion chamber has a 2.5% change due to asymmetrical control rod insertion and withdrawal.

An experiment was performed in the PSBR using ex-core detectors and the WL-7186 miniature fission chamber that is placed inside the central thimble. In the first part of the experiment, asymmetrical control rod insertion and withdrawal were investigated at low power using all of the detectors at R1 open pool and D_2O tank location. In the second part of the experiment, the WL-7186 miniature fission chamber is removed from the reactor core, and high power measurements are taken at various reactor powers at R1 open pool, D_2O tank, FNI, and FFT. These results are used in the computational part of the thesis and compared with the experimental values. WL-7186 counts per second measured in the experiment matched with the simulation result from MCNP. In addition to this, the RSS fission chamber and spare fission chamber results show a great change in the simulations. However, in the experiment, reactor power stayed at 1 W.

Finally, all of these operational parameters and results are used to develop detector responses for each detector. A cubic function relating the console power to the corrected power was developed for each experimental location. The experimental value described by Bascom [10] where reactor power is measured by the console is 960 kW at the open pool location which was 1000 kW for the D_2O tank location in core loading 58A. This value was calculated as 955 kW with 0.3% uncertainty for the core loading 59 which proves the defect in the power measurement, and that the correction method is accurate. This correction is applied to the logbook computer and can be used for future experiments when precise reactor power is needed. With the new power correction, better fuel utilization can be done by calculating fuel burnup which is shown in the final chapter.

To summarize:

- Developed an MCNP model for ex-core detectors, self-powered neutron detectors, and WL-7186 miniature fission chamber.
- Investigated the neutron flux shape change with the control rod positions, and how this affects the behavior of the detectors.
    - Control rod insertion shifts the reaction rate per source particle to the edge of the reactor core, thus affecting the power calculations.
- Investigated temperature effect on detector responses.
    - Uniform and variable fuel temperature effects were investigated and less than 5% effect was observed.

- Investigated the effect of reactor operation parameters on the detector response including fuel temperature, control rod positions, and core locality (near D_2O, FNI, FFT, and open pool).
    - The effect of these operational parameters individually and together investigated for the detector responses. The core locality has a significant effect on detector responses with the highest calculated power observed in the D_2O tank position
- Investigated asymmetric control rod position effect on neutron flux and the detector behaviors
    - Asymmetry of the control rods has a significant effect on detector responses. Transient and safety asymmetry showed a $\pm$20 kW difference in 500 kW power measurements and a $\pm$21 kW difference in shim and regulation rod asymmetrical movement.
- Investigated the importance of individual fuel rods on the detector response
    - The contribution of each fuel element to the detector response was investigated. Closer fuel elements to the detector region have a significant contribution to the tally result compared to the fuel elements located further away.
- Performed an experiment with an in-core detector and ex-core detectors to validate the computational model.
    - Low power asymmetrical control rod movement showed the simulation results matched with experimental values for the WL-7186 miniature fission chamber that is placed inside the central thimble. The simulation

results also showed that reactor power should be higher according to the ex-core detectors.

- Developed a method to quickly estimate detector response under varying conditions by coupling FMESH and Fission Matrix Method calculations with detector response functions.
    - Detector response functions were created for each detector using every fuel element contribution and multiplied with the FMESH and Fission Matrix Method source distribution to estimate detector responses.
- Developed a correction for the power calibration based on operating conditions and a metric for power tilt based on operation detectors to improve power measurements and fuel burnup
    - Using the power correction developed in this thesis, any power reading from the reactor console can be corrected for each detector and any core locality. Fuel burnup can be also corrected with new detector response functions. With the current core loading, 3.7% less burnup was calculated using newly developed detector responses.

9.2 Future Work

- A more detailed model for the detectors may be implemented into the MCNP by incorporating detailed geometry and material description and additional physics with MCNP
- Using the FMESH method and Fission Matrix Method, detector responses need to be updated after each core loading by the scripts developed in this thesis
- Detailed investigation of the non-uniform fuel temperature by the MCNP may be done by changing material temperature in each fuel element, tmp card, and $S(\alpha, \beta)$ values.
- Asymmetrical control rod power correction for various operational parameters may be developed by the Fission Matrix Method by incorporating a script that reads user input that changes the temperatures, control rod positions, and core localities.
- Detector power corrections should be implemented into previous core models (i.e., core loading 57, 58, 58A) to verify that the correction factor is insensitive to the core loading. If not, for each core loading, new detector responses and power corrections should be created.
- Updating the control console with newly developed detector responses in this thesis. This can be done with a calculation block at Foxboro DCS.
- Investigation of central thimble detector responses at high power using an in-core detector that is suitable for the high flux operation.

Bibliography

[1] NRC, “Power Uprates for Nuclear Plants,” *Backgrounder, Office of Public Affairs*, 2018. https://www.nrc.gov/docs/ML0311/ML031120472.pdf.

[2] NRC, “Approved Applications for Power Uprates,” 2019. https://www.nrc.gov/reactors/operating/licensing/power-uprates/status-power-apps/approved-applications.html.

[3] T. Kaiba *et al.*, “Validation of neutron flux redistribution factors in JSI TRIGA reactor due to control rod movements,” *Appl. Radiat. Isot.*, vol. 104, pp. 34–42, 2015, doi: 10.1016/j.apradiso.2015.06.026.

[4] A. Rau and W. J. Walters, “Validation of coupled fission matrix – TRACE methods for thermal-hydraulic and control feedback on the Penn State Breazeale Reactor,” *Prog. Nucl. Energy*, vol. 123, p. 103273, May 2020, doi: 10.1016/j.pnucene.2020.103273.

[5] W. J. Walters, A. Haghighat, M. Wenner, S. Sitaraman, and Y. Ham, “A methodology for determination of detector response for inspection of a spent fuel pool,” 2010, pp. 3412–3425, [Online]. Available: https://pennstate.pure.elsevier.com/en/publications/a-methodology-for-determination-of-detector-response-for-inspecti.

[6] K. Ünlü, B. Heidrich, M. Trump, and C. Davison, “Relicensing and Utilization of the Penn State Breazeale Reactor (PSBR),” *TM-40035 IAEA, Vienna, Austria*, 2010.

[7] G. Corak, “State Feedback Reactor Control Using a Vanadium and Rhodium Self-Powered Neutron Detector,” The Pennsylvania State University, 2018.

[8] B. J. Heidrich, “TRIGA Reactor Control and Monitoring System.” [Online]. Available: https://www.google.com/url?sa=t&rct=j&q=&esrc=s&source=web&cd=&cad=rja&uact=8&ved=2ahUKEwiO4cKhhI_4AhVvlIQIHdGJBYcQFnoECAUQAQ&url=http%3A%2F%2Fwww.igorr.com%2FDocuments%2F2005-WASHINGTON%2FHeidrich%2520-%2520PSBR%2520Control.pdf&usg=AOvVaw2h0ClZi3No8RraYE.

[9] A. J. Bascom, “Analysis of the Nuclear Heat Source for the Thermoacoustic Power Sensor Prototype at the Pennn State Breazeale Reactor (PSBR),” The Pennsylvania State University.

[10] A. J. Bascom, “Improvements to the PSBR Fuel Management and Neutronics Model in Support of the New Core Moderator Assembly,” The Pennsylvania State University, 2019.

[11] N. Connor, “What is Fission Chamber – Wide Range Detector – Definition.” .

[12] B. J. Heidrich, “Penn State TRIGA Reactor Thermal Power Calibration,” The

Pennsylvania State University, 2003.

[13] Ž. Štancar, L. Snoj, and L. Barbot, "Analysis of the TRIGA Mark II Reasearch Reactor Ex-Core Detector Response," *Proc. Int. Conf. Nucl. Energy New Eur. 2015*, no. C, pp. 307.1-307.8, 2015.

[14] T. Žagar, M. Ravnik, and A. Peršič, "Analysis of TRIGA Reactor Thermal Power Calibration Method," *Nucl. Energy Cent. Eur. '99*, 1999.

[15] A. Z. Mesquita, H. C. Rezende, and R. M. Gomes Do Prado Souza, "Thermal power calibrations of the IPR-R1 TRIGA reactor by the calorimetric and the heat balance methods," *Prog. Nucl. Energy*, vol. 53, no. 8, pp. 1197–1203, 2011, doi: 10.1016/j.pnucene.2011.08.003.

[16] A. Z. Mesquita, H. C. Rezende, and E. B. Tambourgi, "Power calibration of the TRIGA Mark I nuclear research reactor," *J. Brazilian Soc. Mech. Sci. Eng.*, vol. 29, no. 3, pp. 240–245, 2007, doi: 10.1590/S1678-58782007000300002.

[17] Y. D. Ding, P. F. Wang, Q. Bin Wang, and Q. J. Zhang, "Study on the energy response of a multi-layer planar high pressure ionization chamber using MCNP program," *Hedianzixue Yu Tance Jishu/Nuclear Electron. Detect. Technol.*, vol. 34, no. 7, pp. 883–885, 2014.

[18] J. C. Kim, J. K. Kim, Y. K. Kim, and S. H. Park, "Analysis off design characteristics of cylindrical ion chamber made by KAERI. A comparison between egsnrc, MCNP, and experiment," *J. Nucl. Sci. Technol.*, vol. 41, pp. 299–302, 2004, doi: 10.1080/00223131.2004.10875705.

[19] N. R. Taylor, "Analysis of a High Temperature Fission Chamber Experiment for Next Generation Reactors," The Ohio State University, 2017.

[20] Matthew Gift, "INVESTIGATION OF EXPOSURE RATE DISCREPANCIES BETWEEN ENERGY COMPENSATED GEIGER MUELLER TUBES AND PRESSURIZED IONIZATION CHAMBERS DUE TO MUON AND ANTI-MUON COSMIC PARTICLES," 2017.

[21] J. Coburn, S. M. Luker, E. J. Parma, and K. R. DePriest, "Modeling, Calibration, and Verification of a Fission Chamber for ACRR Experimenters," 2016, doi: 10.1051/epjconf/201610605001.

[22] Z. W. Bell, *Materials Selection for a High- Temperature Fission Chamber*, no. August. 2012.

[23] J. D. Wallace, "Monte carlo modeling of ion chamber performance using MCNP," *Health*

Phys., vol. 103, no. 6, pp. 780–786, 2012, doi: 10.1097/HP.0b013e31826021e7.

[24] J. Turso *et al.*, "Toward the implementation of self-powered, wireless, real-time reactor power sensing," *Ann. Nucl. Energy*, vol. 139, p. 107252, May 2020, doi: 10.1016/j.anucene.2019.107252.

[25] J. Kohpazi, S. Czifrus, S. Feher, and G. Por, "Measuring Delayed Part of the Current of a Self Powered Neutron Detector and Comparison With Calculations," *Proc. Int. Conf. Nucl. Energy Cent. Eur. 2001*, pp. 1–8, 2001, [Online]. Available: http://www.djs.si/proc/port2001/pdf/603.pdf.

[26] M. H. B. Rabir *et al.*, "Measurement and simulation of thermal neutron flux distribution in the RTP core," *IOP Conf. Ser. Mater. Sci. Eng.*, vol. 298, no. 1, 2018, doi: 10.1088/1757-899X/298/1/012029.

[27] L. Vermeeren, "Neutron and gamma sensitivities of self-powered detectors: Monte Carlo modelling," *2015 4th Int. Conf. Adv. Nucl. Instrum. Meas. Methods their Appl. ANIMMA 2015*, pp. 1–5, 2015, doi: 10.1109/ANIMMA.2015.7465531.

[28] A. Rau, "FISSION MATRIX METHODS FOR TEMPERATURE AND CONTROL FEEDBACK OF SMALL NUCLEAR SYSTEMS," 2020.

[29] C. J. Werner, "MCNP Users Manual - Code Version 6.2," *Rep. La-Ur-17-29981*, p. 746, 2017.

[30] M. J. Cenko, "Comparison of PSBR operation's history with the TRIGA core management model," The Pennsylvania State University, 1972.

[31] N. Kriangchaiporn, "Advanced fuel management system (AFMS) for PSBR," The Pennsylvania State University, 2001.

[32] Y. Kim, "Pennsylvania State University Breazeale Reactor (PSBR) core Monte Carlo modeling and analyses," The Pennsylvania State University, 1995.

[33] C. Tippayakul, "Development of a practical fuel management system for PSBR based on advanced three-dimensional Monte Carlo coupled depletion methodology," The Pennsylvania State University, 1978.

[34] C. Tippayakul, "Automated three-dimensional Monte Carlo depletion calculation of PSBR / by Chanatip Tippayakul," The Pennsylvania State University, 2003.

[35] "Reactor Dynamics and Fuel Management Group, TRIGSIMS User Manual Version 1.0," 2006.

[36] N. Connor, "What is Rhodium-104 as Emitter – Rhodium-103 as Material – Definition." https://www.radiation-dosimetry.org/what-is-rhodium-104-as-emitter-rhodium-103-as-

material-definition/.

[37] A. M. Bevill, S. R. Johnson, A. M. Ibrahim, and C. R. Daily, *ADVANTG — An Automated Variance Reduction Parameter Generator November 2013*, no. November. 2013.

[38] T. Evans, A. Stafford, and K. Clarno, "Denovo--A New Three-Dimensional Parallel Discrete Ordinates Code in SCALE."

[39] J. C. WAGNER, D. E. PEPLOW, S. W. MOSHER, and T. M. EVANS, "Review of Hybrid (Deterministic/Monte Carlo) Radiation Transport Methods, Codes, and Applications at Oak Ridge National Laboratory," *Prog. Nucl. Sci. Technol.*, vol. 2, no. 0, pp. 808–814, 2011, doi: 10.15669/pnst.2.808.

[40] A. Sood, "Workshop on Radiation Detection and Simulation with MCNP," *14th Bienn. Top. Meet. Radiat. Prot. Shield. Div. Am. Nucl. Soc.*, vol. 836, 2006.

[41] J. K. Shultis and R. E. Faw, "An MCNP Primer," *Structure*, vol. 66506, no. c, pp. 0–45, 2006, [Online]. Available: http://www.mne.ksu.edu/~jks/MCNPprmr.pdf.

[42] M.-J. Wang and A. Haghighat, "A Novel Detector Response Formulation for RAPID," 2018, [Online]. Available: https://www.researchgate.net/publication/326250674_A_Novel_Detector_Response_Formulation_for_RAPID/citation/download.

[43] D. Şahin and K. Ünlü, "Determination of self shielding factors and gamma attenuation effects for tree ring samples," *J. Radioanal. Nucl. Chem.*, vol. 291, no. 2, pp. 549–553, 2012, doi: 10.1007/s10967-011-1281-x.

[44] D. A. Ross, "The Pennsylvania State University TRIGA Reactor Description, Initial Testing, and First Three Years of Operation," The Pennsylvania State University, 1969.

[45] J. Hanania, K. Stenhouse, and J. Donev, "Moderation." https://energyeducation.ca/encyclopedia/Moderation.

[46] J. J. Duderstadt and L. J. Hamilton, "Nuclear Reactor Analysis." 1976.

[47] *Westinghouse in-core detectors brochure*. .

[48] Dagistan Sahin, "Activity, Exposure Rate and Gamma Spectrum Prediction for Neutron Irradiation Materials at Radiation Science and Engineering Center," no. September, p. 154, 2008.

[49] L. Unger and D. Trubey, "Specific Gamma-Ray Dose Constants for Nuclides Important to Dosimetry and Radiological Assessment." doi: 10.1126/science.109.2828.245.

[50] Glenn G. Knoll, *Radiation Detection and Measurement (4th Edition)*. 2010.

[51] "Gaseous Ionization detectors regions." https://nuclear-power.com/wp-

content/uploads/2019/01/Gaseous-Ionization-Detectors-Regions-min.png.

[52] A. Pungerčič, D. Čalič, and L. Snoj, "Computational burnup analysis of the TRIGA Mark II research reactor fuel," *Prog. Nucl. Energy*, vol. 130, 2020, doi: 10.1016/j.pnucene.2020.103536.

APPENDIX: An Example ADVANTG Input File

```
method                  fwcadis
outputs                 mcnp silo response

mcnp_input              core59r1.in
mcnp_tallies            4 14 24 34 184
mcnp_material_names     1 water
                        3 SS
                        4 graphite
                        5 B4C
                        8 D2O
mcnp_sb_type            none

anisn_library           27n19g

mesh_x                  -60 60
mesh_x_ints             40
mesh_y                  -220 -40
mesh_y_ints             60
mesh_z                  -80 98
mesh_z_ints             40

mcnp_mxspln             50
mcnp_ww_collapse_factor 1
```

VITA

Gokhan Corak was born in Turkey on May 29, 1991. He received his Bachelor of Science degree in nuclear engineering from The Hacettepe University in May 2014 in Turkey. He continued his graduate studies at the Pennsylvania State University. Gokhan received his Master of Science degree in nuclear engineering in May 2018. He completed his Ph.D. titled "Improvements on power calibration and core monitoring at the Penn State Breazeale Reactor" in August 2022.